

Faculty of Aerospace Engineering  
DESIGN SYNTHESIS EXERCISE

---

## Eco-Runner

### Final Report

---



Project No. 14  
Faculty of Aerospace Engineering  
July 2, 2013



# DELFT UNIVERSITY OF TECHNOLOGY

## DESIGN OF THE NEXT ECO-RUNNER

GROUP 14  
FINAL REPORT  
JULY 2, 2013

*Author:*

J.C.A. DE BAERDEMAEKER	4107837
L.J. VAN DEN BERG	4090357
E.T. DIMITROVA	4111249
J.H.D FINOULST	4109813
R. GEUTJENS	1519611
N. VAN HAMEREN	1306146
A. VAN DER HEIDE	1523341
B. HU	4087720
M.M. REIJNE	1303341
A.M.M. SPOELSTRA	4116038

*Tutor:*

Ir. J. SINKE

*Coaches:*

R.K.M. BOUWER  
C.G.F. BOUSSION



# Preface

In completing the Bachelors degree of the Faculty of Aerospace Engineering of Delft University of Technology all students participate in the Design Synthesis Exercise (DSE), which is the final project of the Bachelor. The TU Delft Eco-Runner Team and Ir. J. Sinke initiated a DSE project on the design of a new Eco-Runner vehicle. This report is the final report of the Eco-Runner DSE by group 14 of 2013.

The final report is intended to communicate the final results of the Eco-Runner DSE group and describe the detailed design phase of the project. This report works out the output of the mid-term report, which defined the conceptual design, into further detail. Feedback is given by the tutor of the Eco-Runner DSE group, Assistant Prof. J. Sinke, and the two coaches: R.K.M. Bouwer and C.G.F. Boussion. We, as the Eco-Runner DSE group, would like to thank our tutor and coaches for the given support throughout the project in terms of constructive advice and helpful answers to any questions that arose.

The final report discusses the detailed design phase of a new Eco-Runner vehicle. The designing was done with a group of ten people and the report shows the work done within a ten week time frame. The focus of this report is on working out the conceptual design (discussed in the mid-term report) to a higher level of detail. Actual sizing of the subsystems is done within this report. In order to effectively read this report, it is assumed that the reader has some engineering background and a basic understanding of electrical vehicles.

*Delft, June 2013*



# Table of contents

<b>1</b>	<b>Introduction</b>	<b>1</b>
<b>2</b>	<b>Pre-Design Considerations</b>	<b>3</b>
2.1	Market Analysis . . . . .	3
2.1.1	Micro-, Macro- and Internal Analysis . . . . .	3
2.1.2	SWOT Analysis . . . . .	5
2.2	Sustainable Development Strategy . . . . .	6
2.2.1	Analysis of the Eco-Runner . . . . .	6
2.2.2	The “RRR” Strategy: . . . . .	6
2.3	Functional Breakdown . . . . .	6
2.4	Functional Flow . . . . .	7
2.5	Technical Risk Map . . . . .	8
<b>3</b>	<b>Body Aerodynamics</b>	<b>11</b>
3.1	Introduction . . . . .	11
3.1.1	Fundamental Principles of Aerodynamics . . . . .	11
3.1.2	Design Requirements and Targets . . . . .	14
3.2	Method . . . . .	16
3.2.1	Iteration Process . . . . .	16
3.2.2	Design Process . . . . .	17
3.3	Results . . . . .	18
3.3.1	Body . . . . .	18
3.3.2	Body With Front Fairings . . . . .	21
3.3.3	Total Body . . . . .	24
3.4	Recommendations . . . . .	26
<b>4</b>	<b>Body Structure</b>	<b>29</b>
4.1	Functions and Requirements . . . . .	29
4.2	Sensitivity Analysis . . . . .	29
4.3	Material Specification . . . . .	30
4.3.1	Laminate and Sandwich Skin Layer Material . . . . .	30
4.3.2	Sandwich Core Material . . . . .	31
4.4	Design for Load Cases . . . . .	32
4.4.1	Design Method . . . . .	33
4.4.2	Load Cases . . . . .	33
4.5	Final Body Lay-up and Mass Estimation . . . . .	36
4.6	Inserts . . . . .	36
4.6.1	Loads on Inserts . . . . .	37
4.6.2	Insert Type . . . . .	37
4.6.3	Installation of Inserts in Sandwich Structures . . . . .	38
4.7	Production of the Body . . . . .	38
4.7.1	Production Method . . . . .	38
4.7.2	Mold Selection . . . . .	39
4.7.3	Alignment and Joining of the Body Halves . . . . .	40
4.7.4	Monocoque Production . . . . .	40
4.8	Verification and Validation . . . . .	41
4.9	Cost Budget for the Monocoque Body . . . . .	42
4.10	Compliance Matrix . . . . .	42
4.11	Conclusion and Recommendations . . . . .	44

<b>5</b>	<b>Suspension</b>	<b>45</b>
5.1	Introduction	45
5.1.1	Previous Work	45
5.1.2	Functions and Requirements	45
5.2	Sensitivity Analysis	46
5.3	Contingency Management	46
5.4	Detailed Design Front Suspension	47
5.5	Detailed Design Rear Suspension	49
5.6	Verification and Compliance Matrix	50
5.7	Production Plan	52
5.8	Validation Plan	52
5.9	Mass and Cost	53
5.10	Risk Analysis	55
5.11	Recommendations	55
<b>6</b>	<b>Wheels</b>	<b>57</b>
6.1	Functions and Requirements	57
6.2	Load Cases	58
6.2.1	Assumptions	59
6.3	Tires	59
6.3.1	Tire Selection	59
6.4	Spokes	60
6.4.1	Front Wheel Spoke Pattern	61
6.4.2	Spoke Count and Cross-Section of the Front Wheel	61
6.4.3	Rear Wheel Spoke Pattern	64
6.5	Rims	67
6.5.1	Inflation Pressure	67
6.5.2	Bending Stiffness	68
6.5.3	Cornering	69
6.5.4	Motor Torque and Static Braking Torque	69
6.5.5	Lay-up	69
6.6	Hub	70
6.6.1	Hub Design	70
6.6.2	Rear Wheel Hub	70
6.7	Bearings	71
6.8	Production Plan	71
6.8.1	Lay-up of Rim	71
6.8.2	Lay-up of Spokes	72
6.8.3	Spoke Attachment	72
6.8.4	Lay-up of Front Wheel Hubs	72
6.8.5	Lay-up of Rear Wheel Hub	72
6.8.6	Pre-tensioning the Spokes	72
6.9	Mass and Cost Budget	73
6.10	Verification and Validation Procedures	74
6.11	Conclusion and Recommendations	74
6.11.1	Compliance Matrix	74
6.11.2	Final Wheel Design	75
<b>7</b>	<b>Electronic Systems</b>	<b>77</b>
7.1	Electrical System	77
7.1.1	Hardware Diagram	78
7.1.2	Software Diagram	78
7.1.3	Data Handling Diagram	78
7.2	Communication Flow Analysis	79
7.3	Propulsion Battery	80
7.3.1	Risk Analysis	81

7.4	Solar Cells . . . . .	82
7.5	Motor . . . . .	83
7.6	Other Systems . . . . .	83
7.6.1	System Controller . . . . .	83
7.6.2	Data Logger . . . . .	84
7.6.3	Accessory Battery . . . . .	84
7.7	Cost and Mass Breakdown . . . . .	84
7.8	Recommendations . . . . .	85
7.9	Compliance Matrix . . . . .	85
<b>8</b>	<b>Driving Strategy</b>	<b>87</b>
8.1	Analytical Model . . . . .	87
8.2	Numerical Model . . . . .	88
8.3	Strategies and Results . . . . .	90
8.4	Verification . . . . .	91
8.4.1	Drag Forces . . . . .	92
8.4.2	Propulsive Force . . . . .	93
8.4.3	Lost Energy . . . . .	93
8.4.4	System Test . . . . .	93
8.5	Validation Plan . . . . .	94
8.6	Sensitivity Analysis . . . . .	94
8.7	Operation and Logistic Concept Description . . . . .	95
8.8	Conclusion and Recommendations . . . . .	97
<b>9</b>	<b>Vehicle Characteristics</b>	<b>99</b>
9.1	Body Configuration Parameters . . . . .	99
9.1.1	Ground Clearance . . . . .	99
9.1.2	Camber . . . . .	99
9.1.3	Wheelbase . . . . .	100
9.1.4	Track Width . . . . .	100
9.1.5	Position of the Wheels . . . . .	100
9.1.6	Position Fairings . . . . .	100
9.1.7	Size Wheel Fairings . . . . .	101
9.1.8	Ground Clearance Fairings . . . . .	101
9.2	Rollover Stability . . . . .	101
9.3	Braking Stability . . . . .	102
9.4	RAMS Characteristics . . . . .	103
9.4.1	Reliability . . . . .	103
9.4.2	Availability . . . . .	104
9.4.3	Maintainability . . . . .	104
9.4.4	Safety . . . . .	104
9.5	Cost and Mass Breakdown . . . . .	104
9.5.1	Cost Breakdown . . . . .	104
9.5.2	Mass Breakdown . . . . .	105
9.6	Vehicle System Characteristics . . . . .	107
9.7	Internal and External Lay-out . . . . .	107
<b>10</b>	<b>Future Prospects of the Design</b>	<b>111</b>
10.1	Project Development . . . . .	111
10.2	Manufacturing, Assembly and Integration Plan . . . . .	112
10.3	Project Gantt Chart . . . . .	113
<b>11</b>	<b>Conclusion and Recommendations</b>	<b>117</b>
	<b>Bibliography</b>	<b>119</b>
<b>A</b>	<b>Visualization of the Aerodynamic Design Process</b>	<b>121</b>

<b>B Mass Spring System</b>	<b>125</b>
<b>C Bearings</b>	<b>127</b>
<b>D Motordata</b>	<b>129</b>
<b>E Track Rotterdam Specifications</b>	<b>131</b>
<b>F Logbook</b>	<b>133</b>

# Nomenclature

<i>Abbreviation</i>	<i>Description</i>
ASTM	American Society for Testing and Materials
BMS	Battery Management System
CAD	Computer-Aided Design
CFD	Computational Fluid Dynamics
CFRP	Carbon Fiber Reinforced Polymer
cg	Center of Gravity
cnc	Computer Numerical Controlled
CTE	Thermal Expansion Coefficient
DC	Direct Current
D:Dream	Delft: Dream Realisation of Extremely Advanced Machines
DEMO	Dienst Electronische en Mechanische Ontwikkeling
DSE	Design Synthesis Exercise
FBD	Free Body Diagram
FEM	Finite Element Analysis
FEV	Fuel Efficient Vehicle
GPS	Global Positioning System
HW	Hardware
It	Loading time
MPPT	Maximum Power Point Tracking
NACA	National Advisory Committee for Aeronautics
RAMS	Reliability, Availability, Maintainability and Safety
RRR	Reduce, Re-use and Recycle
SW	Software
SWOT	Strengths, Weaknesses, Opportunities and Threats
UD	Unidirectional

# List of Symbols

<i>Symbols</i>	<i>Description</i>	<i>Unit</i>	<i>Symbols</i>	<i>Description</i>	<i>Unit</i>
$a$	Acceleration	$m/s^2$	$\alpha$	Slope	$rad$
$A$	Area	$m^2$	$\delta$	Deformation	$m$
$A$	Aspect Ratio	-	$\eta$	Efficiency	-
$A \cdot C_D$	Drag index	$m^2$	$\theta$	Spoke Angle	$deg$
$b$	Width	$m$	$\lambda$	Failure rate	-
$C_d$	2D Drag Coefficient	-	$\mu$	Dynamic Viscosity	$Pa \cdot s$
$C_D$	3D Drag Coefficient	-	$\mu$	Poisson's Ratio	-
$C_l$	2D Lift Coefficient	-	$\rho$	Density	$kg/m^3$
$C_p$	Pressure Coefficient	-	$\sigma$	Stress	$Pa$
$C_r$	Rolling friction coefficient	-	$\tau$	Shear stress	$Pa$
$C_\alpha$	Cornering stiffness	$N/rad$			
$d$	Diameter	$m$			
$D$	Drag	$N$			
$e$	Oswald Factor	-			
$E$	Energy	$J$			
$E$	Young's modulus	$Pa$			
$F$	Force	$N$			
$g$	Gravitational acceleration	$m/s^2$			
$G$	Shear modulus	$Pa$			
$h$	height	$m$			
$I$	Current	$A$			
$I$	Moment of Inertia	$m^4$			
$l$	Length	$m$			
$L$	Lift	$N$			
$m$	Mass	$kg$			
$M$	Moment	$N \cdot m$			
$p$	Pressure	$Pa$			
$P$	Power	$W$			
$q$	Shear Flow	$N/m$			
$r$	Radius	$m$			
$R$	Reliability	-			
$Re$	Reynolds Number	-			
$s$	Distance	$m$			
$t$	Time	$s$			
$t$	Thickness	$m$			
$T$	Torque	$N \cdot m$			
$U$	Voltage	$V$			
$v$	Velocity	$m/s$			
$V$	Shear force	$N$			
$V_f$	Fiber to resin volume	-			
$w$	Deflection	$m$			
$W$	Weight	$N$			

# List of Tables

2.1	Technical risk map	9
3.1	Aerodynamic characteristics of the side view airfoils of the body	19
3.2	Aerodynamic characteristics of the testing bodies, results from VSAERO	19
3.3	Aerodynamic characteristics of the body with front fairings	21
3.4	Aerodynamic characteristics of the model, changing fillet radius of the front fairings	22
3.5	Aerodynamic characteristics of the models with different shapes of front fairings	24
4.1	Table of requirements for the body	30
4.2	Fiber properties of Torayca T3000 and Torayca M46J	31
4.3	Composite properties of Torayca M46J, using epoxy resin, 60% fiber volume [1]	31
4.4	(Specific) structural properties of foam, aluminum honeycomb and balsa wood	32
4.5	Mechanical properties for Nomex honeycomb	32
4.6	Thicknesses and mass of each monocoque section	37
4.7	A trade-off between wet lay-up and prepreg technique	39
4.8	Considered materials with their thermal properties [2]	39
4.9	Cost budget for monocoque body	42
4.10	Compliance matrix for the body	43
5.1	Requirements for the suspension system	46
5.2	Material properties [3]	48
5.3	Trade-off table material choice	48
5.4	Suspension compliance matrix	52
5.5	Material costs for aluminum 7075 and stainless steel alloy 17-7PH	53
5.6	Material cost for the off-the-shelf carbon fiber rod	53
5.7	Mass breakdown for the total front suspension	53
5.8	Cost breakdown for the front suspension	54
5.9	Mass breakdown rear suspension	54
5.10	Cost breakdown for the rear suspension for aluminum and steel	54
5.11	Cost breakdown for the rear suspension for the carbon fiber rods	54
6.1	Table of requirements for the wheels	58
6.2	Load cases for the wheels	58
6.3	The specified characters of the Michelin 44-406 and 45-75R16 tires.	59
6.4	The effect of the rolling friction coefficient and the mass of the 44-406 and 45-75R16 tire.	60
6.5	The pattern of the spokes per wheel	61
6.6	The assumptions and corresponding implications	62
6.7	Force equilibrium equations for case I and case II	63
6.8	Inputs and outputs of case I and case II for the front wheel	63
6.9	Inputs and outputs of case I and case II for the rear wheel.	63
6.10	Front wheel spoke characteristics	64
6.13	The characteristics of the three rear spoke patterns.	64
6.11	Thee rear wheel concepts.	65
6.12	The trade-off summary of three rear wheel spoke patterns.	66
6.14	Inputs and outputs of equation 6.3	68
6.15	Inputs and outputs of equation 6.4	68
6.16	Assumptions and implications on the structural analysis of the rim	69
6.17	The lay-up of carbon fiber fabrics and its required thickness, $t$ , for the rims.	70
6.18	Dimensions and material specifications of the front and rear wheel hub.	71
6.19	Mass of the wheels	73

6.20	Cost of the wheels . . . . .	73
6.21	Compliance matrix of the wheels . . . . .	75
7.1	Specifications of a single Panasonic NCR-18650A cell [4] . . . . .	80
7.2	Resulting battery . . . . .	81
7.3	Specifications of a single cell [5] . . . . .	82
7.4	Motor specifications obtained from Mitsuba . . . . .	83
7.5	System controller specifications [6] . . . . .	83
7.6	Specifications of the data logger [7] . . . . .	84
7.7	Cost and mass breakdown of the electrical system . . . . .	85
7.8	Compliance matrix electronic systems . . . . .	86
8.1	Constants used in the simulation . . . . .	90
8.2	Results from the simulation . . . . .	91
8.3	Analytical and numerical results for drag forces . . . . .	92
8.4	Analytical and numerical results for the propulsive force . . . . .	93
8.5	Analytical and numerical results for the lost energy . . . . .	93
8.6	Analytical and numerical results for the energy efficiency . . . . .	93
8.7	Constants used in the simulation . . . . .	94
9.1	Cost breakdown for monoque body, wheels, suspension and electronic subsystems. . . . .	105
9.2	Total mass breakdown for the Eco-Runner vehicle . . . . .	106
9.3	Total vehicle configuration . . . . .	107
9.4	Vehicle performance characteristics . . . . .	107
9.5	Body dimensions . . . . .	108
C.1	Bearing specifications [8] . . . . .	127
E.1	Simplified model of the track . . . . .	131
F.1	Authors and editors per written section . . . . .	133

# Summary

The Shell Eco-marathon challenges young engineers to push the boundaries of fuel efficiency through designing, building and testing ultra-light fuel efficient vehicles (FEV). The purpose of this final DSE report is to present the preliminary design of such a FEV vehicle that is to compete in the prototype battery electric class of the Shell Eco-marathon. The mission need statement of the DSE project is to “drive the largest distance with the least amount of energy”. The two most important requirements that drive the design are a maximum vehicle curb mass of 30 kg and a minimum efficiency equivalent to 790 km/kWh.

In order to come up with a feasible design that satisfies the requirements, a systematic approach has been undertaken by the DSE group, and the project has been divided into three milestones: the baseline report, the mid-term report, and this final report. Here, the output of the mid-term report is further analyzed and a detailed design of the aerodynamic body, the body structure, suspension, wheels, driving strategy and electronic systems is performed. For all these subsystems requirements have been generated, different design possibilities have been analyzed and trade-offs have been made. All topics in this detailed design feature multiple iterations in order to achieve optimal performance and compliance with the stipulated requirements.

In order to design the aerodynamic body, different models have been tested using the dedicated computational fluid dynamics (CFD) software VSAERO. The final output of the CFD analysis is a drag coefficient of 0.085 [–] and a frontal area of 0.285 m<sup>2</sup>. For the body structure, a material selection and finite element analysis have been performed on the aerodynamically tested body in order to reinforce it for the load cases experienced during the competition. Using carbon fiber and Nomex sandwich panels, the entire monocoque has been optimized to a mass of 6.946 kg. An embedded thru axle suspension is used to connect the front wheels to the body and a bracket and rail suspension with four rods is implemented in the rear. The total mass of the front suspension for the left and right wheel is 330 g and the total mass of the rear suspension is 1621 g. The front wheels and rear wheel are made entirely of carbon fiber and weigh a total of 1898 g. Michelin tubeless tires with minimal rolling friction coefficient are used. The developed driving strategy is based on using the motor at its most efficient condition while maintaining a velocity around 7.5 m/s with a feedback mechanism.

This particular strategy results in an energy efficiency of 2110 km/kWh. Since the vehicle is to compete in the battery electric class of the Eco-marathon, a proposal for an electric system has been made. Most of the electronic components used are off-the-shelf products. The distinctive features are the lithium-ion battery and the solar cells. The solar cells have an efficiency of 30% and provide an average power of 37.5 W.

By assessing all vehicle subsystems together, it can be concluded that the detailed design is feasible and compliant with the weight and efficiency requirement. All subsystems have been integrated in the body and no issues in terms of pilot visibility and insufficient space have been encountered. The overall design shows a great improvement in terms of weight and energy savings when compared to the Eco-Runner 3, the current TU Delft FEV competing in the Shell Eco-marathon. The Eco-Runner 4 will have a curb mass of 23.6 kg, which is 45% less than the Eco-Runner 3, and will have an efficiency better than the required 790 km/kWh.

In the process of the detailed design various issues have been encountered such as erroneous results from CFD tests, insufficient computing power for MATLAB calculations and limited knowledge in finite element analysis. Due to these problems as well as the limited amount of time available, it is recommended to perform some further tests and develop more elaborate analytical models in order to validate the current results. A suggestion for the next step in the design is building a scaled prototype based on the present CAD model and performing a wind tunnel test.



# 1 Introduction

In recent times, environmental aspects of vehicles have become more and more important. This report discusses the detailed design of the next Eco-Runner, which is an answer to this environmental craving. The Eco-Runner is designed according to the Shell Eco-marathon rules of 2013 [9], aiming to be as fuel efficient as possible. More specifically, the mission of the project can be stated as follows:

*Drive at least 790 km on 1 kWh*

The design process was subdivided into four distinct phases. The first phase, the project outline, merely dealt with the organization of the team and planning the other phases. The second phase, closed with the baseline report, identified requirements of the design, as well as the design options. The third phase, closed with the mid-term report, made a choice between these options and finished with a conceptual design of vehicle subsystems. The vehicle was divided into subsystems as follows.

- body;
- vehicle dynamics;
- wheels
- electronic systems.

The final report, closing the fourth and final design phase, covers the detailed design of the Eco-Runner. The subsystems listed above are designed to a higher level of detail. Moreover, it was chosen to develop a simulation tool capable of simulating a driving strategy for the Shell Eco-marathon. Besides, the body was split up into an aerodynamic and a structural section.

The report is structured as follows. First of all, the viability of the design is investigated in Chapter 2. Then, the aerodynamic design of the body is elaborated in Chapter 3. In the fourth chapter, the structural design of the body is described. The report continues with the suspension design in Chapter 5, after which the design of the wheels is described in Chapter 6. Next, a simulation tool for the driving strategy of the Shell Eco-marathon is designed, which is describe in Chapter 7. The design of the electronic systems is presented in Chapter 8. Moreover, general design choices and key figures of the design are treated in Chapter 9. Furthermore, plans for the future of the design are made. This includes an assembly plan and a Gantt chart. Finally, a conclusion is drawn and recommendations are made.



# 2 Pre-Design Considerations

Before the actual design process of the next Eco-Runner vehicle is initiated, viability of the project must be ensured. Therefore, a market analysis is conducted first. Then, a sustainable development strategy is established. This carefully developed strategy makes sure that not only the race is about sustainability, but also the design of the vehicle. Finally, an analysis of the functions of the Eco-Runner is done and a risk analysis is performed.

## 2.1 Market Analysis

The following section presents the performed market analysis of the Eco-Runner project. It is important to understand that the Eco-Runner vehicle is a competition vehicle. In this sense, some parts of the market analysis, such as market dynamics, cannot be discussed. However, it is still important to clearly describe the business environment and identify all the project stakeholders and their requirements. Furthermore, a strengths, weaknesses, opportunities and threats (SWOT) analysis is conducted that outlines the factors that determine the success of the Eco-Runner project, as well as possible problems which might be encountered.

### 2.1.1 Micro-, Macro- and Internal Analysis

In order to identify all the stakeholders involved in the Eco-Runner project, the entire business environment is visualized in figure 2.1. The business environment has three levels: the macro-environment, the micro-environment and the internal environment. The macro-environment comprises general forces and trends rather than specific organizations. On the other hand, the micro-environment includes all individuals and organizations that affect the activities of the Eco-Runner project directly or indirectly. Last but not least, the internal environment shows the processes and structures internal to the organization that influence the activities and choices made. The positive outcome of this business environment analysis is that all involved stakeholders can be clearly identified. In the following list, their relevance to the Eco-Runner project is described. Moreover, their requirements are stated.

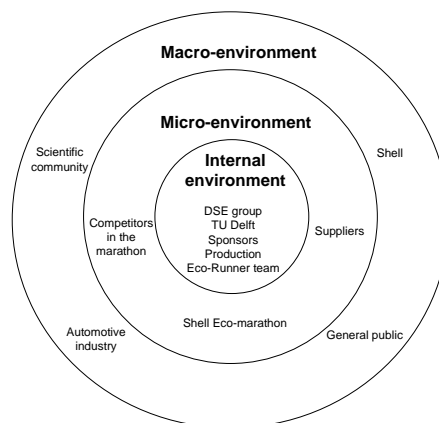


Figure 2.1: Business environment diagram

**Scientific community:** The Eco-Runner could be used as a validation project of scientific and engineering principles. Furthermore, if articles or books from winning teams are published, such as *The World's Most Fuel Efficient Vehicle* [10], this adds to the scientific knowledge and can be used as a reference or starting point for further research. Important for the scientific community is that the project contributes

to current studies, especially in the field of light-weight materials and aerodynamics. Another requirement is that the design process is carefully documented and published according to the scientific standard.

**Automotive industry:** If the Eco-Runner team comes up with an innovative design which proves to be successful in terms of fuel efficiency, the automotive industry may be interested in the ideas of the team and possibly apply some concepts to mass manufacturing of vehicles. Furthermore, expert opinions from the automotive industry can positively influence the outcome of the project and lead to future collaborations. The automotive industry demands that the vehicle contains innovative designs with promising market potential, contributing to the development of existing vehicle technologies.

**General public:** The Eco-Runner team has the chance to send a message to the public, gain popularity and thus, additional funding from independent sponsors, and attract the attention of prospective new members. This can only be achieved when the vehicle attracts attention. Furthermore, it should be safe, friendly to the environment and perform well in the race.

**Shell:** The general public with its ideas about environmentally friendly vehicles is a pressure group for Shell to establish a more sustainable business strategy. Furthermore, Shell is company that has the resources available for funding research. Shell demands that the vehicle is as energy efficient as possible. Besides that, vehicles taking part in the competition have to contribute positively to the image of the company.

**Competitors in the marathon:** The performance of the other competitors throughout the years sets the targets for the competitions to come. The designs of the competitor teams from previous years can be analyzed by the Eco-Runner team and benchmarks regarding vehicle performance can be set.

**Suppliers:** Suppliers have an influence on the design process. Since it often takes time to deliver a certain component, it has to be ordered well in advance. This means that the design process should not be lagging at any point. Furthermore, suppliers may impose restrictions on the ordered component in terms of price.

**Shell Eco-marathon:** The Shell Eco-marathon is the institution that thoroughly checks whether or not the rules are followed by the teams. The design of the Eco-Runner must be compliant with all regulations.

**DSE group:** The DSE group is comprised of ten students and is responsible for designing a battery-powered Eco-Runner vehicle to compete in the prototype class of the 2014 Shell Eco-marathon. Required by the DSE group is to improve designing skills and functioning within a team.

**TU Delft:** TU Delft is the educational institution responsible for providing the required knowledge and expertise to the DSE group. In this sense, TU Delft, as an entity, puts its mark on the Eco-Runner project. It is the guidance of the instructors and the resources available (literature, facilities, etc.) which influence the final design in a positive manner. Vital for TU Delft is that the design is well documented and useful for future participation in the race as well.

**TU Delft Eco-Runner team:** The team participating in the Eco-marathon benefits from a vehicle that is already designed to a certain extent and is more fuel efficient than their previous design. Thus, a well recorded design trade-off process is very beneficial to them. The last important factor for the team is that the design should have a production plan and manufacturing plan that lies within the budget of costs, including sponsors and manufacturers, of the TU Delft Eco-Runner team.

**Sponsors and production:** The sponsors in the project are of utmost importance. Without their financial backup, the Eco-Runner vehicle cannot be produced. Most of the sponsoring is in the form of custom-made parts for the vehicle. In this sense, the Eco-Runner project itself can stimulate some companies to produce new tools and instruments and accept more special orders from their clients. Sponsors do, however, require the vehicle to achieve a high ranking in the competition. Moreover, the vehicle should contribute positively to the image of the sponsor.

## 2.1.2 SWOT Analysis

Now that the business environment and all the stakeholders are identified, a SWOT analysis of the Eco-Runner project as a whole is conducted. The project is a social system which consists of the DSE team and Eco-Runner team collaborating in order to complete their mission. The main goal of this analysis is to determine the key success factors for the project. The outcome of the SWOT analysis is summarized in figure 2.2.

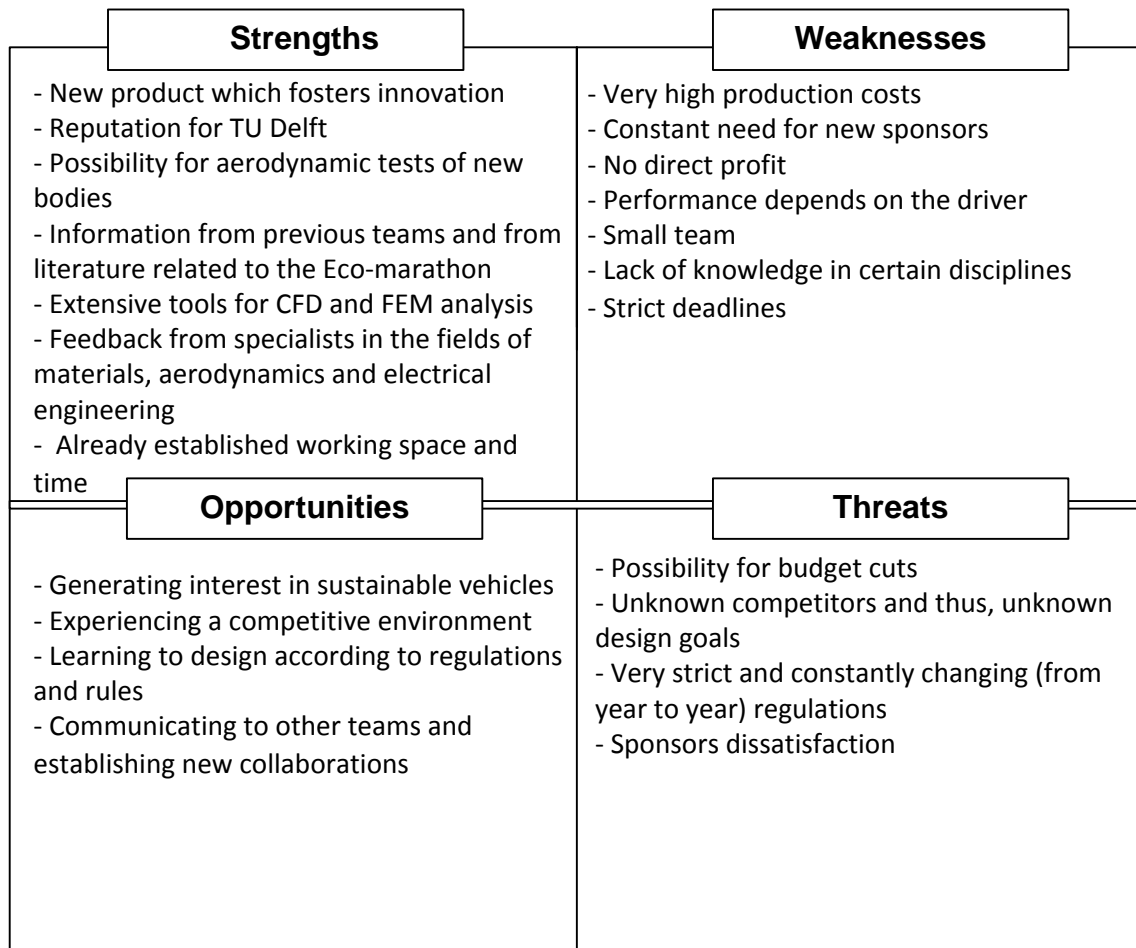


Figure 2.2: SWOT - analysis

**Strengths:** The Eco-Runner project is a project with the goal of designing an innovative vehicle. In this sense, the team has a complete freedom to explore different solutions, as long as the stipulated rules and requirements of the Eco-marathon are followed. Furthermore, the TU Delft offers strong support in terms of specialists and facilities which means that the design team has all of the tools required to come up with a successful design. The information from previous Eco-Runner teams can facilitate a more organized design process in which some of the issues encountered in past years can be solved quickly and easily. Last, but not least, the already established working plan and internal structure within the team ensure that there will be no delays during any of the project stages.

**Weaknesses:** Building an ultra-light, highly efficient vehicle is a task which requires multi-disciplinary knowledge. However, it often happens that there is a lack of understanding of certain concepts. Together with the small size of the design team, this creates a definite problem. On the other side, the strict deadlines do not allow for a complete vehicle design to be made. If the Eco-Runner project is viewed from a more global perspective. Since the vehicle is a part of a competition, it can be concluded that there is no direct profit from the whole design and manufacturing process. Yet, the production costs are

high compared to mass manufactured cars. This is due to the fact that several important components such as the wheels and the body are custom made.

**Opportunities:** The opportunities which the Eco-Runner project offers are mainly related to generating interest in sustainable vehicles. By participating in the Shell Eco-marathon, the team has the chance to compete and show the capabilities of the designed vehicle in terms of efficiency. Furthermore, some important skills such as designing according to regulations and requirements can be developed. Communication with other teams during the competition and establishing contacts may prove useful during future projects.

**Threats:** The production costs for the Eco-Runner are high and sponsorship is limited, thus there is a possibility for budget cuts which might cost the team its participation in the competition. The sponsorship also depends on the performance of the team at the Shell Eco-marathon and so an unsuccessful ranking might lead to loss of support from companies. Furthermore, the constantly changing rules do not allow using the same design as the previous year. As a result, designs are changed every year. Last, but not least, since the Eco-marathon is a competition, the element of surprise is always present: unknown competitors with unknown funding and human resources.

## 2.2 Sustainable Development Strategy

It is important to understand that meeting the needs of the present time shall not compromise the ability of future generations to meet their own needs. In this sense, during every step of the design process, a sustainable way of working must be employed. This section presents a concise sustainable development strategy which will be applied throughout the project.

### 2.2.1 Analysis of the Eco-Runner

The Eco-Runner will be an electric vehicle powered by a lithium-ion battery which means that it will have zero direct emissions. The primary goal for sustainability is to improve the design such that the fuel efficiency is as high as possible. However, emissions may be produced by the generator of electric power as well as the materials used and the manufacturing process. During the design, concepts with a high ecological impact are reduced as much as possible.

### 2.2.2 The “RRR” Strategy:

The main sustainable concept of the Eco-Runner project is to develop a fuel efficient vehicle with a high action radius. However, the sustainable aspect goes further than this. There is also a focus on materials, manufacturing and the final product should be environmentally friendly. In the scope of the project, this is accomplished by means of the Reduce, Re-use and Recycle or “RRR” strategy. The basic idea is that reducing the footprint of the vehicle is possible by means of optimizing the design and the manufacturing process (increased efficiency), re-using materials and components from previous Eco-Runner vehicles and finally employing new materials which can be recycled later. The “RRR” strategy is summarized in Figure 2.3, which can be used as a check during the steps of the design process. It is important to note that when designing a component, one should design with the material and the manufacturing process in mind in order to achieve the best result. Thus, the goal of increasing the fuel efficiency is the top-level priority. After this, one should look at the sustainability of the materials or manufacturing process itself. Since the team tries to use new sustainable design techniques and strategies, some ideas can be applied in the future by automotive manufacturers with the creation of more sustainable vehicles as outcome.

## 2.3 Functional Breakdown

The mission of the design is to successfully compete in the Shell Eco-marathon. In order to do this, the design should perform several functions. Vital functions for the design are shown in Figure 2.4.

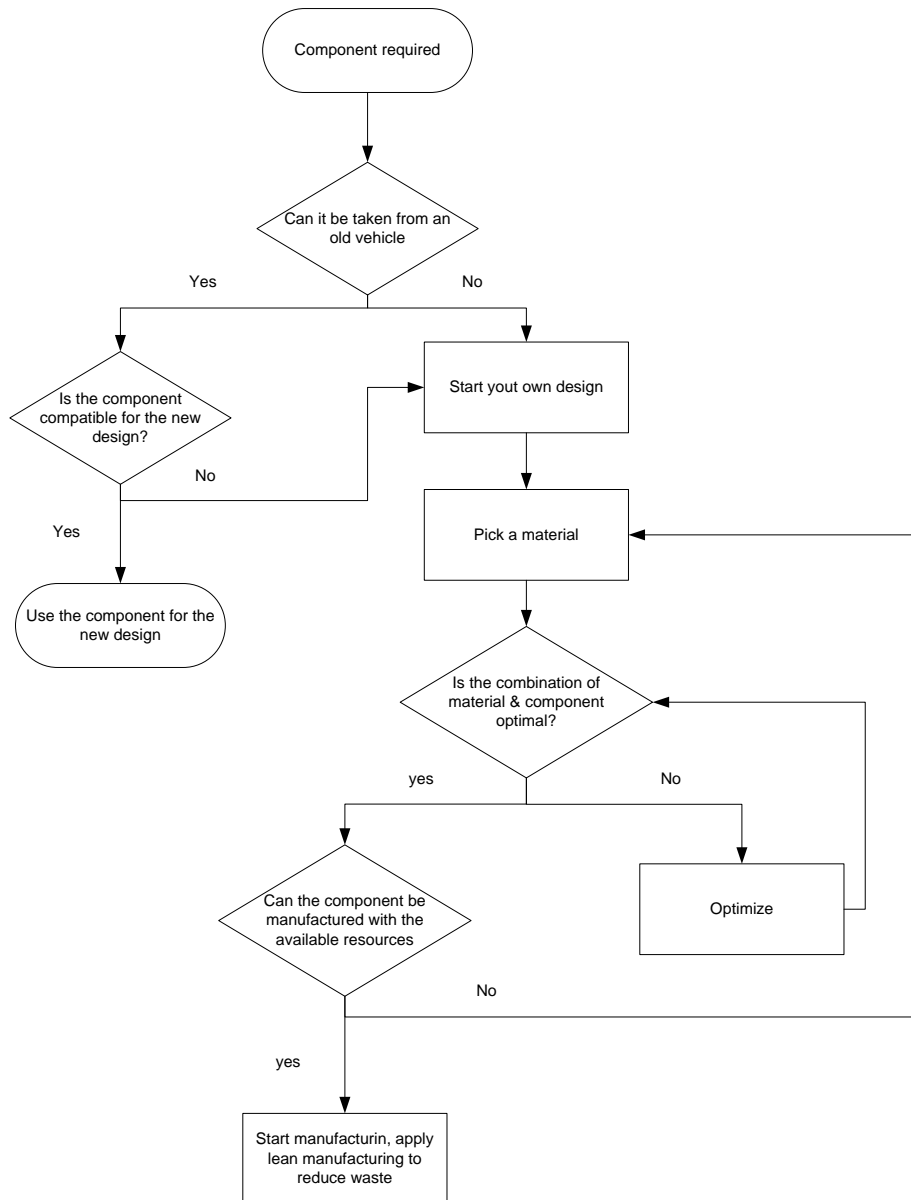


Figure 2.3: Sustainable strategy chart

Vehicle control is only achieved, when the vehicle is stable. Besides that, the pilot has to be able to steer, accelerate and decelerate the vehicle. Of course, vision for the pilot should be provided in such a way that he or she can clearly see the track. Energy is provided to the vehicle in two ways. At the beginning of the race, energy is solely retrieved from the battery and transferred to the motor. Later, energy is generated (e.g. by solar cells) as well, which can then be used by the vehicle.

## 2.4 Functional Flow

The functional flow discusses the same functions mentioned in the functional breakdown structure. The only difference, however, is that the functional flow is structured with time. Functions that the system must perform are displayed in a logical order. The functional flow diagram is shown in Figure 2.5.

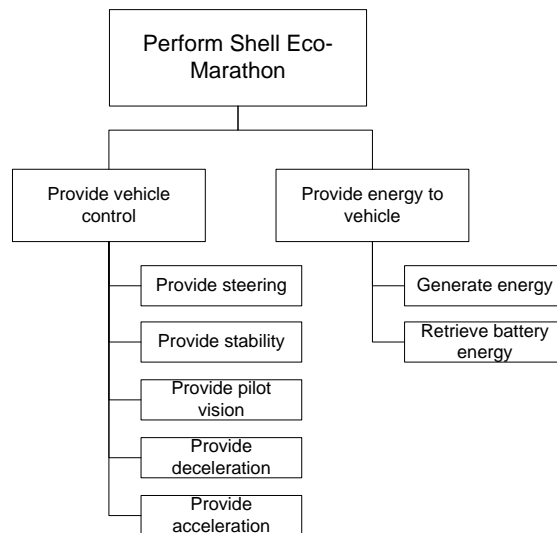


Figure 2.4: Functional breakdown structure for the Eco-Runner vehicle

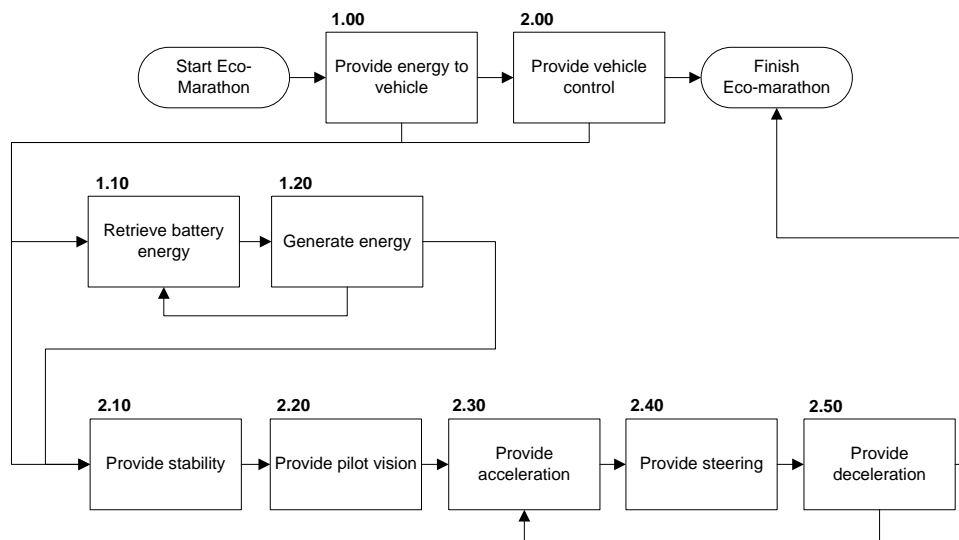


Figure 2.5: Functional flow diagram for the Eco-Runner vehicle

Notable is the feedback loop between the retrieval of energy from the battery and the generation of energy. It states that the battery powers the motor and energy that is generated is stored by capacitors. Another feedback loop is shown within the driving sequence. The idea is here, that the vehicle accelerates, after which steering is required to keep the vehicle under control. At some point in the race, a deceleration may be required. After that, the vehicle may want to accelerate again, repeating the loop.

## 2.5 Technical Risk Map

Every subsystem brings a certain risk for the mission. These risks have to be taken into account during the design process. Risks are not a problem, as long as they are mitigated as much as possible. In this section, risks of the subsystems are identified and mapped.

### **Body Aerodynamics:**

1. Drag coefficient is not accurate

### **Body structure:**

2. Weak spots in the body due to incorrect lay-up and assembly
3. Body weight exceeds the budget
4. Local damage of the body due to an impact
5. Local damage of the body due to heat exposure from the battery

### **Suspension:**

6. Blocking steering system
7. Structural failure of the suspension
8. Dragging of brakes due to deformation of the suspension

### **Wheels:**

9. The rim buckles during its operational life
10. Failure of the axle between the wheel and the suspension
11. Tire gets punctured during the race
12. Failure of one spoke during the operational life
13. Failure of more than one spoke during its operational life
14. Vehicle tipping over, due to major shift of center of gravity

### **Driving strategy:**

15. Not finishing in time using the driving strategy, since no external influences (e.g. wind, other participants, etc) are included in the simulation

### **Electronic systems:**

16. Lowering performance due to charge/discharge cycles
17. Failure due to too many charge/discharge cycles;
18. Failure due to deep discharge of the battery
19. Lowering performance due to a bad battery management controller

Table 2.1: Technical risk map

<b>Consequences</b>	<b>Frequent</b>	<b>Probable</b>	<b>Improbable</b>
<b>Catastrophic</b>		15	6,7,11,13,14,17
<b>Critical</b>		3,5	4,9,10,18,19
<b>Marginal</b>		1,2	8,12
<b>Negligible</b>	16		



# 3 Body Aerodynamics

## 3.1 Introduction

For a vehicle such as the Eco-Runner the aerodynamic drag is responsible for almost 40% of the total drag at a velocity of  $7.5 \text{ m/s}$  [11]. Therefore, it is clear that the aerodynamic design should be of high quality. In this chapter the design process of the aerodynamic body will be discussed. First, there is a small introduction into the basic principles of aerodynamics followed by the design requirements and targets. Second, the methods used to come up with the final design are explained. How these methods lead to results is discussed in the third section of this chapter. Finally, in the last section some recommendations are made for the Eco-Runner team of 2013-2014.

### 3.1.1 Fundamental Principles of Aerodynamics

During the design process some important aerodynamic principles are encountered. Since these principles are the basis for the design, it is important that the reader gets familiar with them.

#### Aerodynamic drag

The aerodynamic drag of a body in a flow can be calculated using Equation 3.1 [11].

$$D = \frac{1}{2} \cdot \rho \cdot A_f \cdot C_D \cdot v^2 \quad (3.1)$$

$D$  is the total aerodynamic drag,  $\rho$  is the air density,  $A_f$  is the frontal area,  $C_D$  is the drag coefficient and  $v$  is the speed. Of all parameters only  $C_D$  and  $A_f$  are dependent on the shape of the body. These two parameters also influence each other, if  $C_D$  decreases often the frontal area increases. That is why the product of both parameters should be as low as possible to keep the aerodynamic drag as low as possible.

#### Drag coefficient

The drag coefficient can be divided into two kinds of drag: friction drag and pressure drag. The friction drag is related to the different boundary layers. A laminar boundary layer has a smaller friction drag coefficient than a turbulent boundary layer. The pressure drag coefficient is related to induced drag and flow separation.

#### Boundary layer

The friction drag mentioned above is created due to a boundary layer on the surface of the body. In this layer the velocity of the airflow decreases towards the surface and becomes zero at the surface. The thickness of this layer determines the amount of friction drag that is created. The thicker the boundary layer, the higher the friction drag. It is possible to distinguish two kinds of boundary layers: a laminar one and a turbulent one. The first one is the preferred boundary layer, because it is a thinner layer than the latter one and the airflow is less disturbed, thus gives less drag.

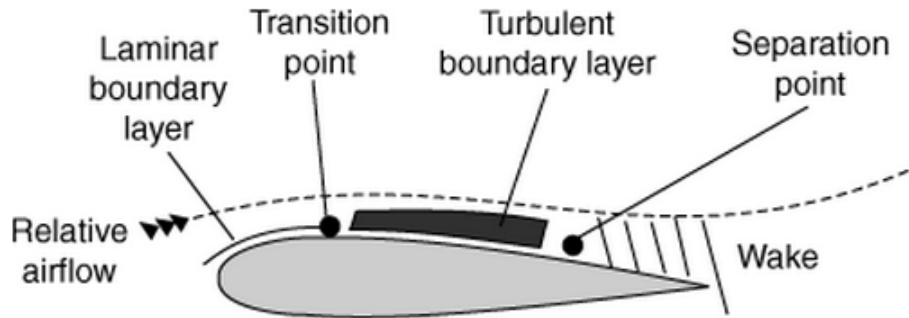


Figure 3.1: Stages of the boundary layer [12]

In Figure 3.1, the stages of a boundary layer can be seen. A boundary layer always starts as a laminar flow and at a certain point, called the transition point, it becomes turbulent. At last also separation can occur, this starts at the separation point. Where both points on the airfoil lay, depends on the shape of the airfoil, the smoothness of the surface and the Reynolds number.

### Reynolds number

The Reynolds number is one of the most important parameters during the design of the aerodynamic shape of the vehicle, since both lift coefficient and drag coefficient are functions of the Reynolds number. To find the Reynolds number, Equation 3.2 can be used.

$$Re = \rho \cdot v \cdot \frac{l}{\mu} \quad (3.2)$$

$Re$  is the Reynolds number,  $v$  is the velocity,  $l$  is the length of the body/fairing,  $\rho$  is the density of air and  $\mu$  is the dynamic viscosity. To compare the aerodynamic properties of different bodies with same scale in the same flows, the Reynolds number should stay constant. When, for example, a scale model is tested in the wind tunnel using a scale of 1:4, the Reynolds number should increase by a factor of four. Since the length of each part (body, front fairings and rear fairing) is different, three different Reynolds numbers are used during the design process: one for the body, one for the front fairings and one for the rear fairing.

### Airfoil

Each 3D-model is build up from 2D airfoils, that is why it is important to choose the right airfoils. Even though there is no one ideal airfoil for every situation, there are a lot of airfoils available. All these airfoils can be sorted in series, one of these series is the NACA 7-series. This is a very laminar airfoil and is chosen to be the basis of the body shape design [13].

### Pressure coefficient curve

The air pressure coefficient  $C_p$  has a direct relation to the shape of the airfoil. The  $C_p$ -curve is a plot of the local pressure coefficient on each point of the airfoil. In other words, it shows the pressure distribution over the airfoil and in combination with the Reynolds number it also shows where the airflow is laminar and where it is turbulent. At low Reynolds numbers, which is the case for the design, the transition point is often located where the  $C_p$ -curve starts descending. By applying small changes to the  $C_p$ -curve, the airfoil shape can be changed and the transition point can be shifted to the rear. In Figure 3.2 an example of a  $C_p$ -curve of a standard airfoil (1) and its transition point (A) can be seen. Also an example of a modified airfoil (2) and its transition point (B) can be seen. The  $C_p$ -curve of the modified airfoil stays horizontal for a longer period and thus the transition point is moved to the rear. In this example the laminar flow is increased from 44 % to 82 %.

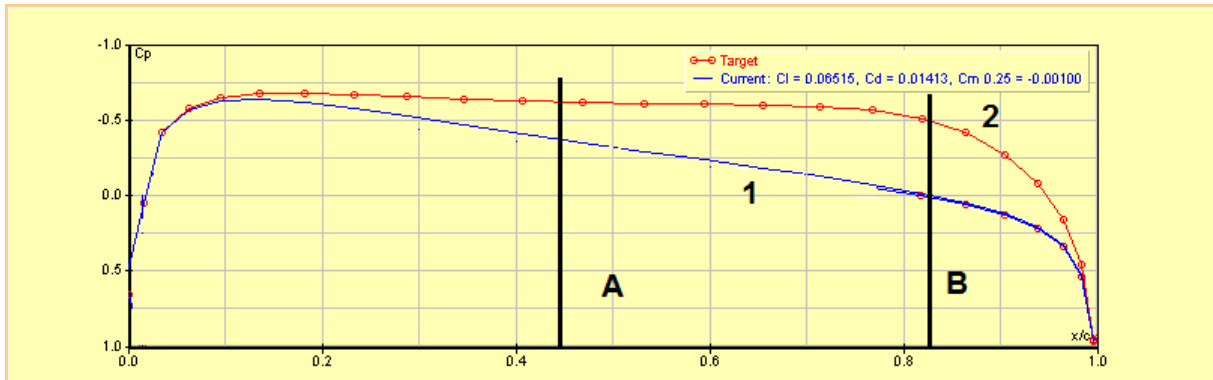


Figure 3.2:  $C_p$ -curves of a standard airfoil (1) and a modified airfoil(2) [11]

### Separation

When an airfoil is modified as described above, the risk that the  $C_p$ -curve becomes too steep at the end arises. This means that at a certain point the airflow can not follow the shape of the airfoil any more and separation of the flow occurs. After separation two things happen: first, the boundary layer separates so there is no friction drag anymore and second, the air does not come together anymore at the end of the airfoil thus the stagnation point at the end (partly) disappears. The latter one can be seen in Figure 3.3. In general, the absence of the stagnation point causes more drag than the absence of the friction drag is beneficial. That is why it is important to avoid separation when possible.

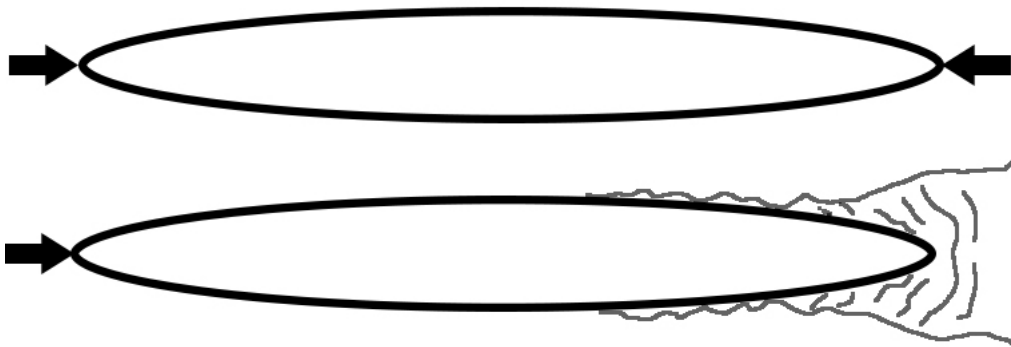


Figure 3.3: Forces due to stagnation points [11]

### Lift, downforce and induced drag

The body consists of a symmetric airfoil, that is used for the top view, and an asymmetric airfoil, that is used for the side view. Asymmetric airfoils can generate lift or downforce at zero angle of attack. Lift arises when the pressure at the top side is lower than the pressure at the bottom. Downforce is created in the same way lift is created, and the higher pressure is located at the top of the body. The pressures at top and bottom of a symmetric airfoil at zero angle of attack are the same and there is no lift or downforce. Both lift and downforce cause induced drag.

Downforce has two disadvantages: first, there will be more rolling drag due to the extra weight and second, there will be induced drag. Lift has one disadvantage and one advantage: there will be induced drag, but the rolling drag decreases. Therefore, downforce is not favorable. However, whether the vehicle should create lift or not is still to be analyzed.

## Ground-effect

As described above, the symmetric airfoil does not create any lift or downforce in the free stream at zero angle of attack. However, when it comes close to the ground, the symmetric airfoil creates downforce. It is because that the area between the ground and the airfoil acts like a Venturi tube. Due to the Venturi-effect a low pressure area arises between the body and ground which creates a downforce.

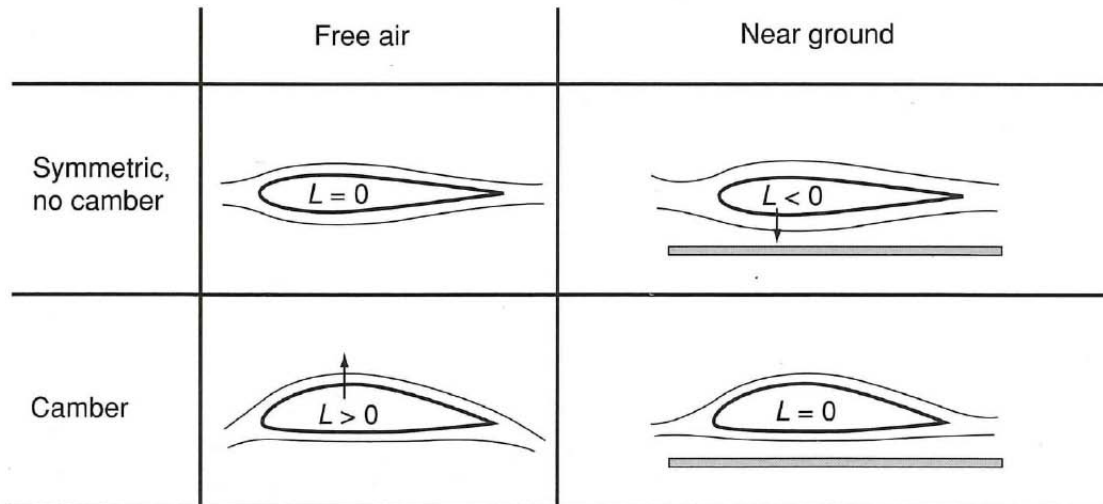


Figure 3.4: Negative and positive lifting effect of an airfoil due to camber and the ground effect[14]

## 3.1.2 Design Requirements and Targets

### Requirement of the drag coefficient

As already mentioned, the aerodynamic drag of the vehicle is given by Equation 3.1. To reduce the aerodynamic drag, the product of the frontal area  $A_f$  and the drag coefficient  $C_D$  should be as small as possible. However, due to the geometric constraints of the vehicle, the frontal area does not differ significantly among all the possible design options. Therefore, the frontal area  $A_f$  is considered to be constant with value of  $0.285 \text{ m}^2$ , measured from the preliminary estimated vehicle model. This makes the drag coefficient  $C_D$  the most important parameter variable to the aerodynamic drag. The aerodynamic drag of the previous Eco-Runner is approximately  $1 \text{ N}$  at the nominal driving speed. Using the standard atmosphere for the air density, the same nominal driving speed ( $7.5 \text{ m/s}$ ) of the vehicle, and the frontal area estimated above, a drag coefficient  $C_D$  of  $0.117 [-]$  is obtained corresponding to  $1 \text{ N}$  of aerodynamic drag. Therefore, to achieve less aerodynamic drag than the previous Eco-Runner, the drag coefficient  $C_D$  of the design should be less than  $0.117 [-]$ .

### Desired lift coefficient

The desired lift coefficient  $C_L$  of the vehicle is determined here. There are two factors to be taken into account. On one hand, the non-zero lift coefficient causes induced aerodynamic drag. On the other hand, the positive lift coefficient will reduce the normal force on the ground and therefore reduce the rolling friction. Based on these two considerations, the negative lift coefficient is obviously excluded from the design option. In the following discussion, the effect of both a positive and zero lift coefficient are analyzed.

Assuming the vehicle has a positive lift coefficient  $C_L$ , the induced aerodynamic drag by this lift coefficient is:

$$D_i = \frac{1}{2} \cdot \rho \cdot v^2 \cdot A_f \cdot \frac{C_L^2}{(\pi \cdot A \cdot e)} \quad (3.3)$$

The reduction in rolling resistance is:

$$\Delta F_r = \Delta L \cdot C_r = 0.5 \cdot \rho \cdot v^2 \cdot A_f \cdot C_L \cdot C_r \quad (3.4)$$

Therefore, the total drag caused by the lift coefficient is:

$$D_i - \Delta F_r = \frac{1}{2} \cdot \rho \cdot v^2 \cdot A_f \cdot \left( \frac{C_L^2}{\pi \cdot A \cdot e} - C_L \cdot C_r \right) \quad (3.5)$$

The minimum  $D_i - \Delta F_r$  occurs when its derivative w.r.t  $C_L$  equal to zero:

$$\frac{2 \cdot C_L}{\pi \cdot A \cdot e} - C_r = 0 \quad (3.6)$$

$$\Rightarrow C_L = \frac{C_r \cdot \pi \cdot A \cdot e}{2} \quad (3.7)$$

Therefore, when  $C_L$  is equal to  $(C_r \cdot \pi \cdot A \cdot e)/2$ , the total drag caused by the lift coefficient is minimal. Substituting Equation 3.7 into Equation 3.5, this minimum value can be found:

$$(D_i - \Delta F_r)_{min} = -\frac{1}{8} \cdot \rho \cdot v^2 \cdot A_f \cdot C_r^2 \cdot \pi \cdot A \cdot e \quad (3.8)$$

The relation of the total resisting force caused by the lift coefficient ( $D_i - \Delta F_r$ ) and the lift coefficient ( $C_L$ ) is shown qualitatively in Figure 3.5.

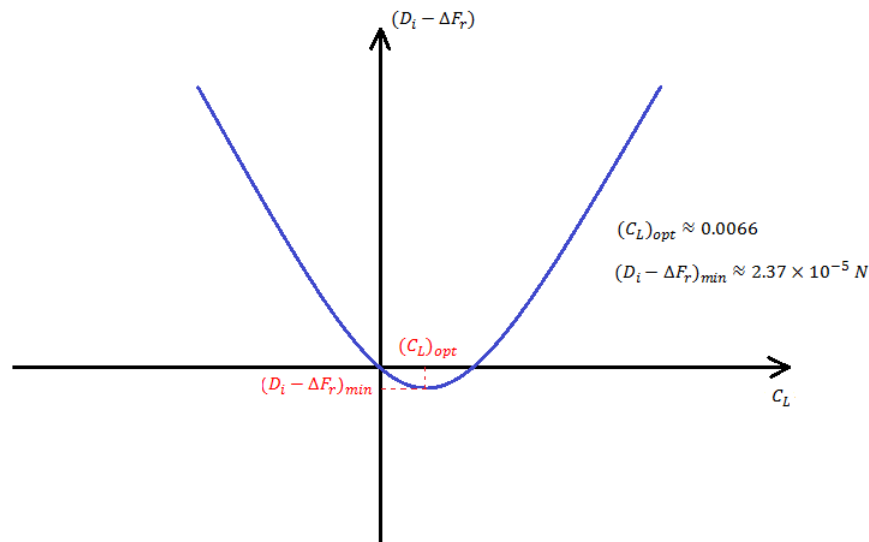


Figure 3.5: A qualitative illustration of optimal lift coefficient

The rolling resistance coefficient  $C_r$  of the tire is  $8.4 \cdot 10^{-4}$ . The Oswald factor  $e$  is always less than one. The aspect ratio  $A$  of the vehicle body is dependent on the airfoil used for the body design, therefore it is not determined yet. However, as an estimation, it is expected to be less than five. Hence, the optimal  $C_L$ , which is the  $C_L$  yielding the minimum  $D_I - \Delta F_r$ , is estimated to be less than 0.0066 [-]. With the frontal area  $A_f$  of  $0.285 \text{ m}^2$ , the  $(D_I - \Delta F_r)_{min}$  is estimated to be  $-2.37 \cdot 10^{-5} \text{ N}$ , meaning that the optimal lift coefficient  $C_L$  can reduce the resisting force of the vehicle by  $2.37 \cdot 10^{-5} \text{ N}$ . Based on the analysis shown above, it is found that the desired  $C_L$  is a positive number which is very close to zero. This optimal  $C_L$  will only reduce the total resisting force by a very small amount. Therefore, for the ease of the design, it is decided to set the desired  $C_L$  equal to zero. With zero lift coefficient, no addition nor reduction of the total resisting force is induced.

Note that the desired lift coefficient of the vehicle is not a requirement, but a target. The lift coefficient of the design output should be as close to this target as possible, but some offset may be accepted, as long as the negative effect is not significant.

## 3.2 Method

For the design of the aerodynamic shape of the vehicle, the same design process as the one for the Eco-Runner 3 is used [11], only shortened due to time limitations. The design process of the Eco-Runner 3 consists of five steps, whereas this process only has three steps, as there is no time to perform a wind tunnel test. These three steps can be seen in Figure 3.6.

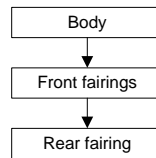


Figure 3.6: Design process

The first step is to find the ideal body. As a next step, the front fairings are added and optimized. Finally, the rear fairing is added and a overall optimization is done. This design can be tested in the wind tunnel. It should be kept in mind that each step consist of several iterations.

### 3.2.1 Iteration Process

The iteration process that is mentioned above is shown in Figure 3.7. Another visualization of this iteration process van be found in Appendix A. This process is performed many times during the design of the aerodynamic shape. It is important that this process is started from the beginning, otherwise the basis of the design will not be good.

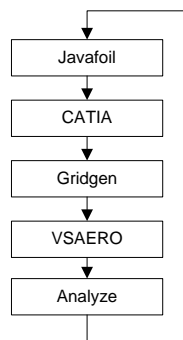


Figure 3.7: Iteration process

#### Javafoil

For the 2D analysis Javafoil is used. This program is chosen to analyze and modify the 2D airfoils, because in contrast to other programs, in Javafoil it is possible to take the ground-effect into account.

#### CATIA

CATIA v5 is used to create 3D models based on the chosen airfoils determined by Javafoil.

#### Gridgen

Gridgen is the linkage between CATIA and the CFD program VSAERO. VSAERO uses finite elements to calculate the results, that is why the 3D-model has to be meshed into a finite amount of squares and this is done by Gridgen.

## VSAERO

VSAERO calculates the different aerodynamic values such as the pressure coefficient  $C_p$ , drag coefficient  $C_D$  and boundary layer properties per square on the mesh.

### Analysis

The results that are generated by VSAERO can now be analyzed in a 3D-environment. After this analysis it is possible to make changes to the model and run through the whole process again.

### 3.2.2 Design Process

As mentioned before the aerodynamic shape of the vehicle is designed in three main steps (see Figure 3.6): the body, the body with front fairings and the full body. This sequence is chosen because the body has the largest influence on the drag, followed by the two front fairings. The rear fairing is added at the end because it encounters the airflow that is already perturbed by the front fairings. This means that it is not possible to optimize the rear fairing without the front fairings in place.

#### Step 1: body

The body is designed using two different airfoils that are based on the NACA 7-series [13], one for the top view and one for the side view. The 2D-airfoils are first optimized using Javafoil and then imported into CATIA to make a 3D-model. For the top view a symmetric airfoil is chosen, since the lift in lateral direction is not favorable. For the side view an asymmetric airfoil is chosen to neutralize the ground-effect. Both airfoils have to meet several requirements: everything has to fit into the body, the frontal area of the body should be as small as possible, the airflow on the body should be laminar as long as possible and separation of the airflow should be avoided. To get everything fitted into the body, a thickness ratio for both airfoils was set: 21% for the top view airfoil and 17% for the other one. Now that all this is known, the basic NACA 7-series airfoils can be modified, shifting the  $C_p$ -curve as was explained in section 3.1.1. Once the body is optimized the next step is adding the front fairings.

#### Step 2: body with front fairings

Designing the front fairings was done in three steps: airfoil optimization, fillet optimization and side shape optimization. Since the airfoil used for the fairings is not influenced by the ground-effect, a symmetric airfoil with the NACA 7-series as basis can be used. Furthermore, it has to meet the same requirements as the airfoils of the body: the wheels have to fit into the fairing, the frontal area of the fairing should be as small as possible, the airflow on the fairing should be laminar as long as possible and separation of the airflow should be avoided. To get the wheels fitted into the front fairings the thickness ratio for the airfoil was set to be 23%. Taking all this into account, the airfoil was modified in Javafoil the same way as the airfoils of the body were, adapting the  $C_p$ -curve.

After the 2D-airfoil is optimized a fillet was added into the 3D-model to connect the fairing smoothly to the body. Several radii for the fillet have been investigated and the one with the most laminar flow is chosen. Finally, the effect of the side view shape on the drag and laminar flow over the fairings has been investigated.

#### Step 3: complete model

The final step in the design process is adding the rear fairing, using the same three steps as in step 2: airfoil optimization, fillet optimization and side shape optimization.

The airfoil of the rear fairing is subjected to almost the same requirements as the airfoil of the front fairings, the only difference is that it has to be large enough to let the rear wheel turn. The thickness ratio of the airfoils is therefore set to 30%. The design process is identical to that of the front fairings.

### 3.3 Results

In this section the results of the design process are shown and discussed. The method used to get these results is described in Section 3.2. First, the results of only the body will be described, followed by the results of adding the front fairings. Finally, the results of the complete vehicle with rear fairing is discussed.

#### 3.3.1 Body

As mentioned in Section 3.2, the main body consists of two airfoils, a top view one and a side view one. In this section first the choice of the top view airfoil is discussed followed by the side view airfoil. For the side view four different options are considered. Finally, the body configuration based on the best combination of top and side view airfoils is chosen.

##### Top view airfoil of the body

The top view airfoil of the body is relatively simple to design, since it is required to be symmetric and no ground effect needs to be considered. By trial and error described in section 3.1.1, the airfoil RU-21T-00632D, which has a  $C_d$  equal to 0.00632 [-] and laminar boundary layer which is up to 97% of the body, is found in Javafoil. It stands out distinctively due to its low drag coefficient and high percentage of laminar flow. Therefore, the airfoil RU-21T-00632D is chosen as the top view airfoil for the body. The airfoil RU-21T-00632D is designed by the team. The first two letters stand for its designer (Rubben). The number before letter "T" is the thickness to chord ratio (21%). The number before letter "D" represents the drag coefficient at zero angle of attack (0.00632). All the airfoils designed by the team are named in the similar way. If the airfoil is asymmetric, its lift coefficient at zero angle of attack is included in the name as well. For example, the airfoil BO-17T-00757D-057L has lift coefficient of 0.057 at angle of attack of zero. The shape, boundary layer and pressure distribution of the RU-21T-00632D airfoil are shown in Figures 3.8, 3.9 and 3.10.

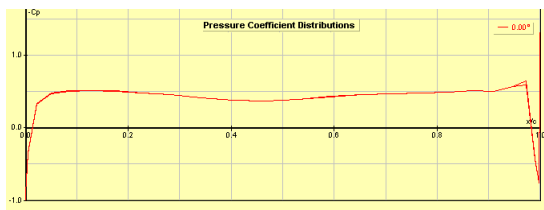


Figure 3.8: The pressure distribution analysis of airfoil RU-21T-00632D by Javafoil

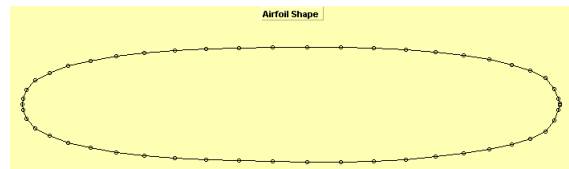


Figure 3.9: Shape of airfoil RU-21T-00632D



Figure 3.10: The boundary layer analysis of airfoil RU-21T-00632D by Javafoil

##### Side view airfoil of the body

The designed angle of attack of the Eco-Runner is  $0^\circ$ . Due to the ground effect, the symmetric airfoil for the side view of the body causes a negative lift coefficient, which is not favorable as discussed in

Section 3.1.2. Hence, cambered airfoil is used for the side view of the body.

In addition to the requirement for the thickness ratio, the design goal in Javafoil is to achieve an airfoil which has zero (as close to zero as possible) lift coefficient with the ground effect and smallest drag coefficient. Four airfoils for the side view of the body are finally selected as the candidates from Javafoil. These candidates are used to build the testing bodies together with the top view airfoil determined above, then the testing bodies are tested in VSAERO. The final airfoil for the side view of the body was selected based on the results from VSAERO.

There are two reasons why the airfoil for the side view of the body cannot be chosen directly from Javafoil. First, the aerodynamic characteristics of the candidate airfoils are similar in Javafoil. Second, examining the 3D body in VSAERO is naturally more reliable than looking at solely the side view airfoil in Javafoil, since the interaction between the top view airfoil and side view airfoil is taken into account in the former method.

The four candidate airfoils for the side view of the body and their main aerodynamic characteristics in Javafoil are listed in Table 3.1.

Table 3.1: Aerodynamic characteristics of the side view airfoils of the body

Name	Thickness ratio	$C_L$ with ground effect [-]	$C_D$ [-]
BO-17T-00757D-057L	17.00%	0.057	0.00757
BO-173T-00735D-047L	17.30%	0.047	0.00735
BO-18T-00767D-073L	18%	0.073	0.00767
BO-175T-00977D-065L	17.50%	0.065	0.00977

## Vehicle body

As mentioned above, four testing bodies are tested in VSAERO. Their profiles and testing results are shown in Table 3.2. In Table 3.2, the total drag coefficient  $C_D$  is the most important design parameter. The friction drag coefficient  $C_{Df}$  is just checked as an auxiliary tool to understand the aerodynamic behavior and check whether the result is doubtful. It is noticed that the  $C_D$  of Body-1 is negative, which is considered as a faulty result. Therefore Body-1 is discarded from the design option. Comparing the rest of the testing bodies, it is found that Body-2 is the best, because it has the smallest  $C_D$  and the  $C_L$  closest to zero.

Table 3.2: Aerodynamic characteristics of the testing bodies, results from VSAERO

Name	Top View Airfoil	Side View Airfoil	$C_D$ [-]	$C_{Df}$ [-]	$C_L$ [-]
Body-1	RU-21T-00632D	BO-17T-00757D-057L	-0.026	0.029	-0.269
Body-2	RU-21T-00632D	BO-173T-00735D-047L	0.064	0.026	-0.11
Body-3	RU-21T-00632D	BO-18T-00767D-073L	0.077	0.03	-0.279
Body-4	RU-21T-00632D	BO-175T-00977D-065L	0.158	0.033	-0.318

The boundary layer analysis and pressure distribution of Body-2 (results from VSAERO) are shown in Figure 3.11 and Figure 3.12 respectively. The red streamlines represent the laminar flow and the blue streamlines represent the turbulent flow.

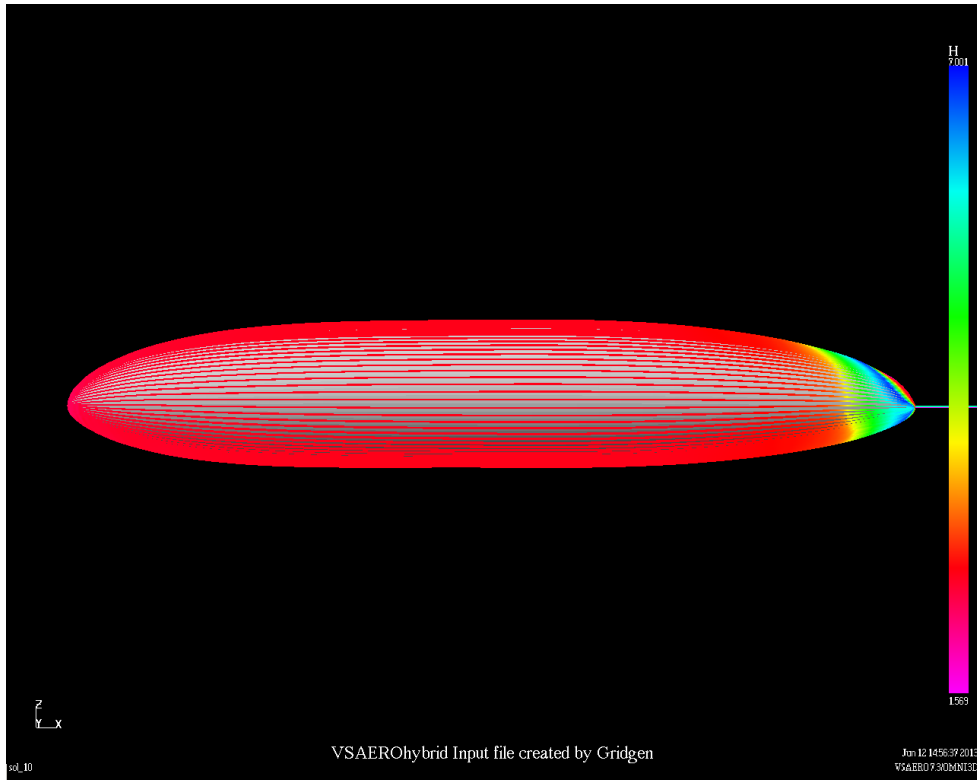


Figure 3.11: Boundary layer analysis of Body-2, side view

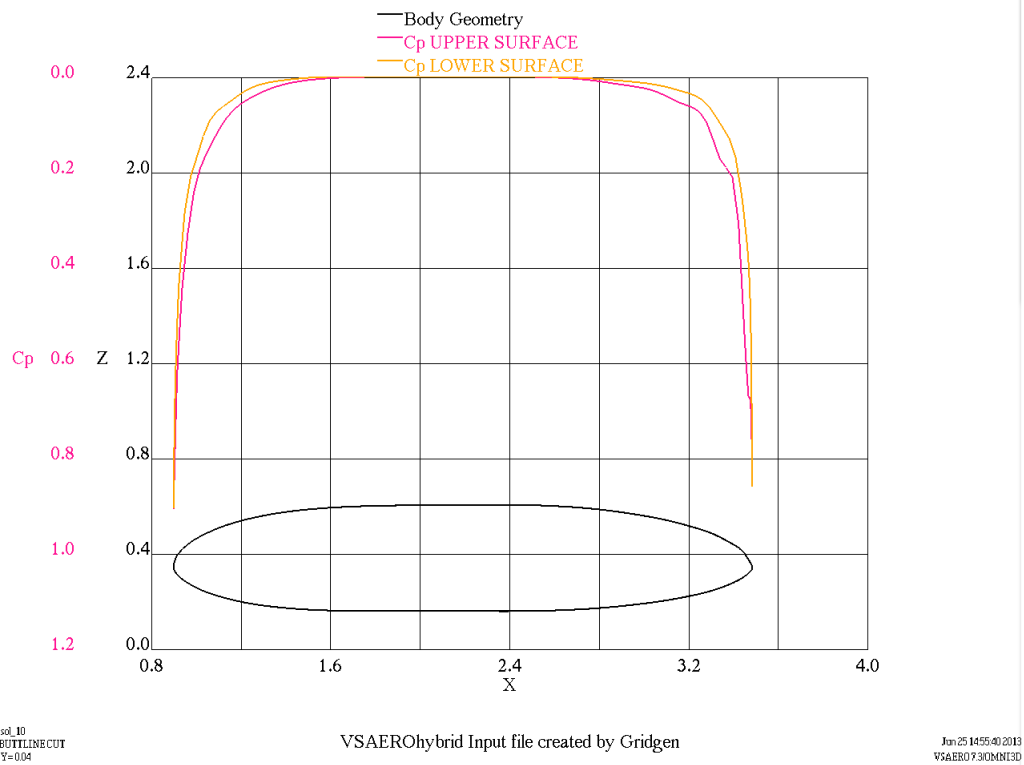


Figure 3.12: Pressure distribution of Body-2

From Figure 3.12, it can be seen that the  $C_p$  curves of the body are quite smooth and flat, which is expected to yield a very large portion of laminar flow over the body. This is proven by Figure 3.11, where about 90% of the body is found to have the laminar flow (red lines). Knowing that the vehicle body of the current Eco-Runner has achieved the laminar flow about 80% of the body, Body-2 shows an improvement. The design goal was to get a drag coefficient of the whole vehicle lower than 0.117 [-]. The  $C_D$  of Body-2 is 0.064 [-]. Since the body is the main cause of the aerodynamic drag, this result is promising to meet the goal.

Even though the lift coefficient of the 2D side view airfoil is positive ( $\approx 0$ ), the lift coefficient of the 3D body is slightly negative. This result infers that the 2D side view airfoil should have more positive  $C_l$  to guarantee a desired 3D lift coefficient (positive and close to zero). Due to the time limitation, the adjustment and redesign of the side view airfoil cannot be performed. With this negative  $C_L$  of  $-0.110$  [-],  $0.94\text{ N}$  downward lift is exerted on the vehicle, resulting  $7.9 \cdot 10^{-4}\text{ N}$  extra rolling friction. Since the extra rolling resistance caused by the negative lift coefficient is very small, this drawback is neglected. Therefore, the Body-2 with side view airfoil BO-173T-00735D-047L is chosen as the vehicle body for the further design. The shape of the airfoil BO-173T-00735D-047L can be seen from Figure 3.11.

### 3.3.2 Body With Front Fairings

The top view of the front fairing is a symmetric airfoil. This airfoil is designed based on the RU-21T-00632D, the one used for the top view of the vehicle body. With three candidates airfoils designed from Javafoil, three different front fairings are made and connected to the body (Body-2) with fillet radius of  $20\text{ mm}$ . These three models (body + front fairings) are then tested in the VSAERO. The results are shown in the Table 3.3 below.

Table 3.3: Aerodynamic characteristics of the body with front fairings

Name	Airfoil for the front fairings	$C_D$ [-]	$C_{Df}$ [-]	$C_L$ [-]
Model 1	BO1939	0.103	0.039	-0.098
Model 2	RU1199	0.085	0.038	-0.112
Model 3	BO2226	0.119	0.04	-0.101

As can be seen from Table 3.3, the Model 2 has the smallest drag coefficient among all the candidates models. This drag coefficient is also lower than the maximum allowable drag coefficient, which is equal to 0.117 [-], specified in Section 3.1.2. Therefore airfoil RU1199 was chosen for the front fairings. Its shape is shown in Figure 3.13.

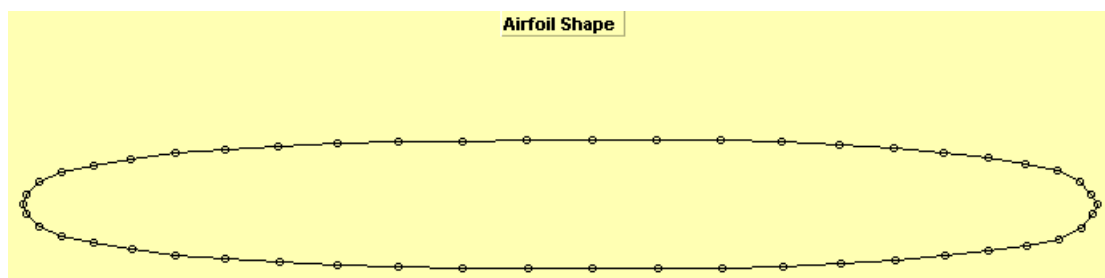


Figure 3.13: Shape of airfoil RU1199

The test from the VSAERO shows that the flow is disturbed by the junction of the wheel fairings to the body (seen from Figure 3.14). This disturbance causes extra drag. Therefore, different fillet radii are applied to the junction and tested in the VSAERO to see how the fillet of the junction affects the flow disturbance. The results are summarized in Table 3.4, which shows that a larger fillet radius induces more disturbance of the flow, thus more drag. This conclusion is also proven by Figure 3.15, where darker stream lines (more turbulence) can be seen near the junction, compared to Figure 3.14.

Table 3.4: Aerodynamic characteristics of the model, changing fillet radius of the front fairings

Radius of Fillet [mm]	$C_D$ [-]	$C_{Df}$ [-]
20(tested before)	0.085	0.038
30	0.094	0.041
40	0.096	0.043
50	0.1	0.044

To reduce the disturbance of the flow at the junction, the fillet radius should be as small as possible. However, it should be kept in mind that a very small fillet radius corresponds to sharp edges which are not favorable to the structure (causes stress concentration) and manufacturing (increases difficulty). Therefore, a radius of  $15\text{ mm}$  is finally chosen for the fillet connecting the fairings to the body. Actually, this number is quite subjective. If more time is available, it is recommended to look into more options ( $10\text{ mm}$ ,  $5\text{ mm}$ ,  $0\text{ mm}$ , etc.) and make a trade-off between the aerodynamic, structural and manufacturing performance with a sensitivity analysis.

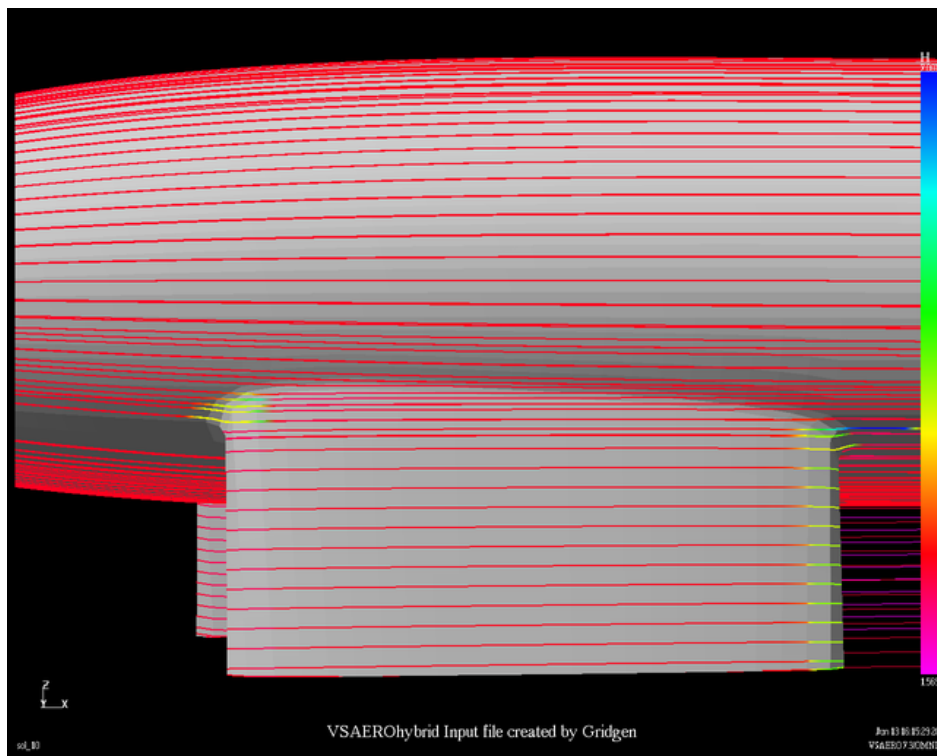


Figure 3.14: Flow disturbance by the junction of  $20\text{ mm}$  radius of fillet

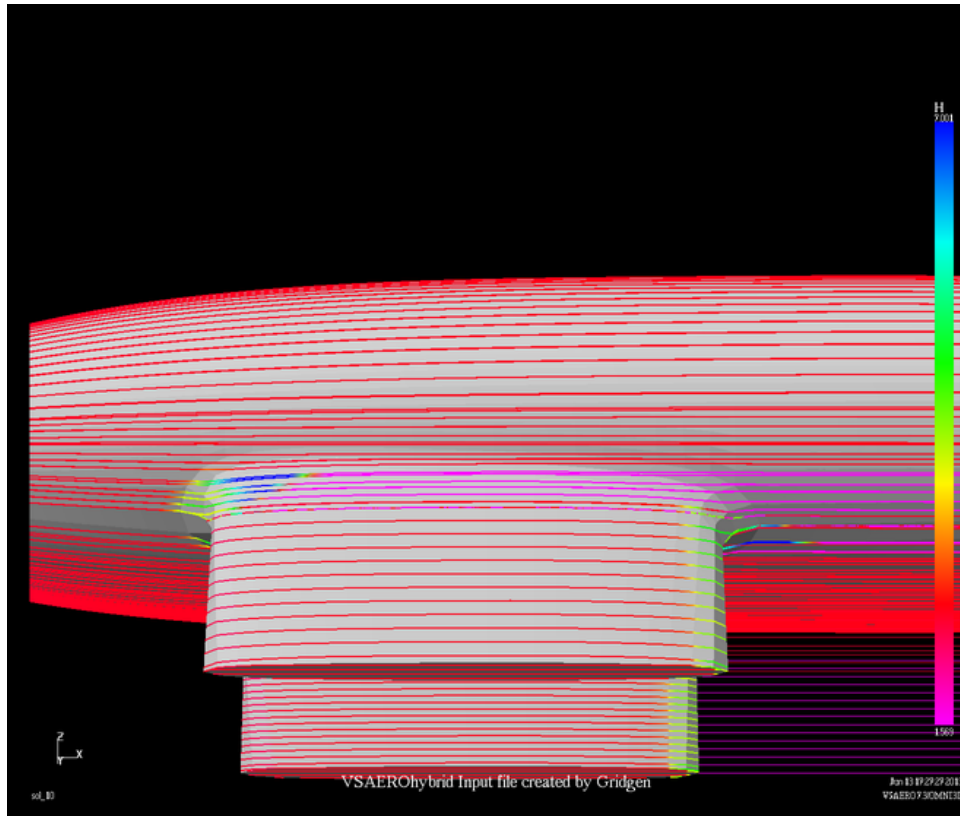


Figure 3.15: Flow disturbance by the junction of 50 mm radius of fillet

At last, different shapes of the front fairings are tested in VSAERO. Apart from the original shape shown above, five more shapes are applied to the front fairings. These are shown in Figures 3.17 to 3.21.

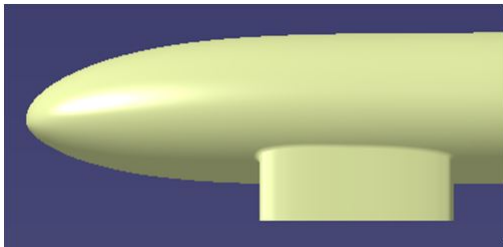


Figure 3.16: Shape 1 (original)

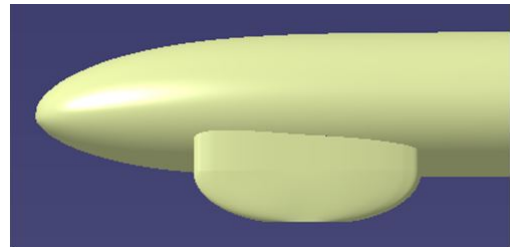


Figure 3.17: Shape 2

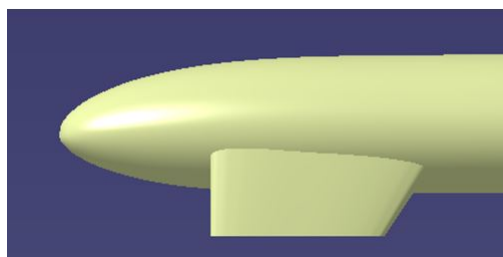


Figure 3.18: Shape 3

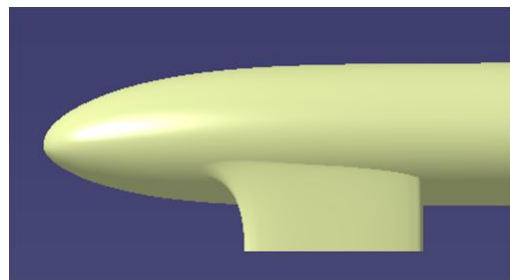


Figure 3.19: Shape 4

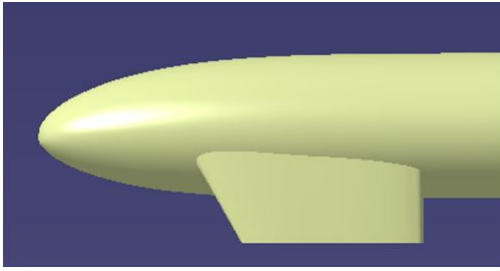


Figure 3.20: Shape 5

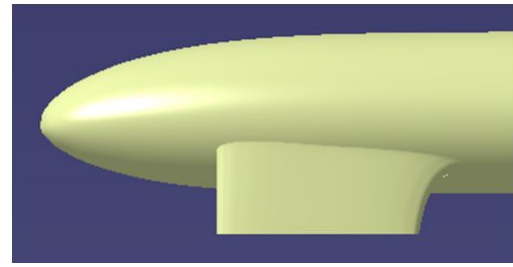


Figure 3.21: Shape 6

The testing results are listed in Table 3.5. It can be seen that the drag coefficient of shape 4 and shape 5 is much lower compared to the other shapes. When looking at shape 4 and shape 5, the difference in drag coefficient is 0.003 [-], which causes only 0.0256 N difference in drag (estimated by Equation 3.1). Therefore, other properties are compared between these two options. It is found that the laminar boundary layer on the lower surface of the model with front fairings shape 5 is longer than the one with shape 4. This may be very beneficial to the rear fairing if the rear fairing is added later on. It is because that the flow entering the rear fairing can be less disturbed if the laminar flow on the lower surface of the body is longer, which results in a lower overall drag coefficient. Therefore, shape 5 is selected.

Table 3.5: Aerodynamic characteristics of the models with different shapes of front fairings

Shape	$C_d$ [-]	$C_{df}$ [-]	$C_L$ [-]
1(original)	0.085	0.038	-0.112
2	0.094	0.037	-0.074
3	0.106	0.038	-0.083
4	0.074	0.04	-0.101
5	0.077	0.04	-0.083
6	0.101	0.037	-0.101

Before moving on to the design of the rear fairing, an experiment is done to the vehicle body. The sharp tip of the rear end of the vehicle body is tentatively cut off as shown in Figure 3.22 as compared to Figure 3.23. The test from VSAERO shows that the new model without the sharp tip reduces the drag coefficient from 0.077 [-] to 0.059 [-]. Hence, this experimental changes in vehicle body is accepted.

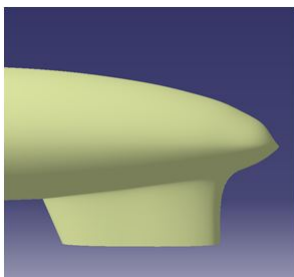


Figure 3.22: Rear end without a cut-off

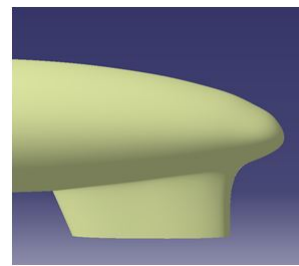


Figure 3.23: Rear end with a cut-off

### 3.3.3 Total Body

Based on the design experience, the airfoil used for the rear fairing has the same “shape” as the one used for the front fairings, but different thickness. The thickness is constrained by the steering angle of the rear wheel.

Two shapes of the rear fairings are tested in VSAERO, as shown in Figures 3.24 and 3.25. However, the testing results of both shapes show negative  $C_D$ , which is physically impossible. Examining the

boundary layer analysis done by VSAERO, it is found that the streamlines do not cover the whole surface of the rear fairing, as shown in Figure 3.26. This is suspected as the cause of the error. A lot of time has been spent on trying to fix this error, however, no credible results have been obtained .

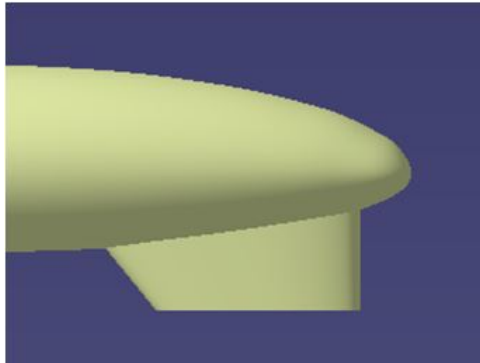


Figure 3.24: Rear fairing shape 1

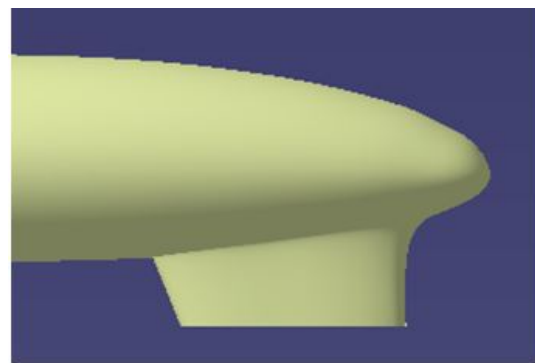


Figure 3.25: Rear fairing shape 2

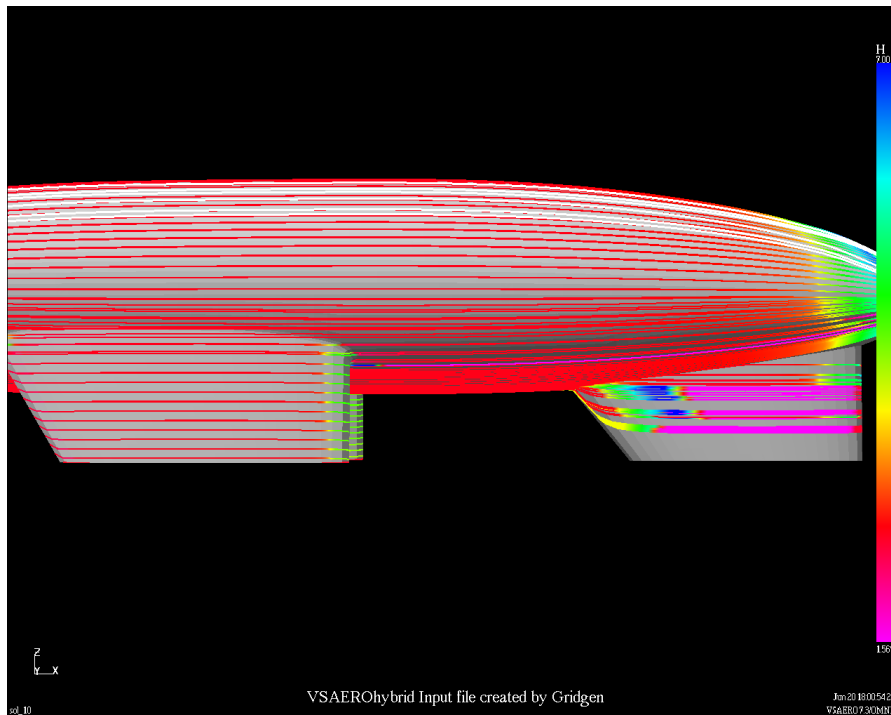


Figure 3.26: Boundary layer analysis of the whole vehicle

Comparing the pressure distribution along the waterline cut at the bottom of the vehicle body, it can be seen that the difference between the two models is very small, as shown in Figure 3.27. Therefore, it is very difficult to make a choice between the two shapes of the rear fairing. Also, due to the errors of VSAERO in the drag coefficient and boundary layer analysis, the accuracy of pressure distribution shown in Figure 3.27 is doubtful, which makes the decision making even more difficult. Finally, Shape 2 of the rear fairing is chosen. The decision is not based on the testing results from VSAERO, but on the experience that sharp corners are easier to cause flow separation than smooth corners. This decision is quite subjective, therefore high design risk is expected.

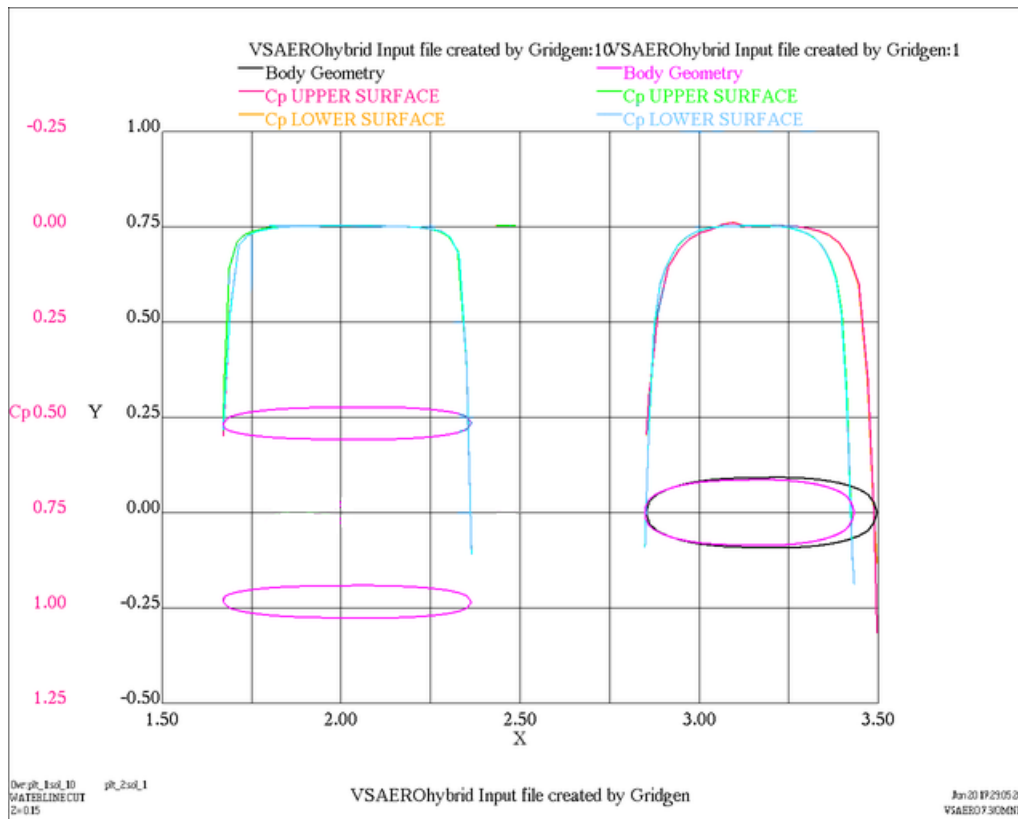


Figure 3.27: Comparison of pressure distribution between two models with different rear fairing Shapes

Due to the error encountered in VSAERO after adding the rear fairing, the drag coefficient of the complete vehicle can only be estimated based on tests performed on the body itself and the body with front fairings. As stated above, the vehicle body alone has a drag coefficient of 0.064 [–]. Adding the front fairings to the body and keeping the body shape unchanged, the new model has a drag coefficient of 0.077 [–]. Therefore, adding front fairings to the body only increases the drag coefficient by only 0.013 [–]. After cutting off the sharp tip at the end of the body, the drag coefficient of the vehicle without rear fairing has been reduced to 0.059 [–]. Assuming adding the rear fairing to the body increases drag coefficient by the same amount as adding the front fairings, the drag coefficient of the complete vehicle is 0.072 [–]. In order to account for the uncertainty of this assumption, a safety factor of two is applied to the drag coefficient contribution of the rear fairing. In this sense, the new drag coefficient of the complete vehicle is estimated to be 0.085 [–]. Therefore the requirement of designing a vehicle with a drag coefficient less than 0.117 [–] is met.

### 3.4 Recommendations

The aerodynamic design of the body of the Eco-Runner 3 took three months, working 40 hours/week with two people. In contrast the DSE project only allows for two 40 hours weeks with two people. Due to this time limitation, the design process is simplified a lot. Therefore, recommendations are made for the future continuation of the design.

The current design process is illustrated in Figure 3.6. If more time is available, it is recommended to follow the process shown in Figure 3.28. In the recommended process, more iterations are included. With these iterations, more design options can be made and tested. Besides, mistakes in one of the design phases can be corrected immediately based on the feedback.

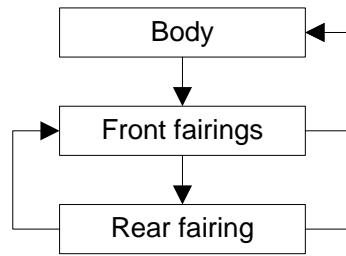


Figure 3.28: Design process

While determining the fillet radius between the fairings and the body, it is found that the fillet with larger radius causes more flow disturbance (based on the results from VSAERO). This is contradictory to the predictions made before the tests, since sharp edges normally tend to cause flow separation. It is suspected that VSAERO may have given erroneous results due to incorrect user operations. Therefore, it is recommended to investigate this problem further and clarify the reasons for the contradiction.

The error encountered in VSAERO after adding the rear fairing suggests that more knowledge about the CFD software should be acquired before the design process. With more reliable results from the CFD software, a more definite design choice can be made. It is recommended that this design choice is further tested in a low speed wind tunnel. Using the feedback from the wind tunnel test, the CFD results can be validated and the vehicle model can be adjusted accordingly.



# 4 Body Structure

In this chapter, the final configuration for the body structure is determined. First, the functions and requirements that should be met after the detailed design are stated. Second, a sensitivity analysis is given. Next, the materials are chosen for the composite body structure. Afterwards, several load cases are discussed and are used to determine the lay-up for the laminate and sandwich structure of the body. Next to the lay-up, thicknesses and masses could be determined. Special attention is paid to the use and installation of inserts which connect subsystems onto the body. The production of the monocoque structure is discussed and a cost estimation is provided. At the end, conclusions and recommendations are given.

## 4.1 Functions and Requirements

Before designing the structure of the body all functions that have to be provided are listed. These functions are shown below:

- provide structural stiffness;
- provide protection for driver (impact resistance);
- provide ergonomics for driver;
- provide driver's vision;
- allow entrance of driver;
- allow fast exit of driver;
- provide space for subsystems: battery, electronics, wheels, suspension, steering, etc.;
- enable access to the subsystems.

These functions are transformed into requirements. These requirements should be met at the end of the detailed design. The requirements are coming from different sources; the Shell Eco-marathon rules, DSE assignment, and calculations from the midterm report. The requirements for the structural design of the body are stated in Table 4.1

## 4.2 Sensitivity Analysis

The structural design is sensitive to other subsystems and design choices. First of all, the structure depends on the shape of the body. This shape is mainly determined by the aerodynamic design. Also the molding technique is dependent on the shape. The suspensions also have a large influence on the body. The structure should be designed for the connection and load transfer of the suspensions. Inserts determine where the body should be reinforced and where sandwich structure should be used. Cut-outs for the pilot's vision and the top cover make reinforcements necessary in the monocoque structure. The cut-out for the top cover are determined by sub-systems and the pilot that should be taken out or placed into the body.

Table 4.1: Table of requirements for the body

Category	ID#:	Requirement:
Dimensions	B.D.1	The body mass shall be equal/lower than 11.5 <i>kg</i> .
	B.D.2	The vehicle body shall be wide and long enough to protect the driver's body in case of a frontal collision into a wall or lateral collision with a different vehicle at an impact speed of 35 <i>km/h</i> equivalent to 20 <i>kN</i> .
	B.D.3	The vehicle shall be designed for any driver position, except for head first.
	B.D.4	A minimum distance of 10 <i>cm</i> shall be present between the driver and the most frontal part of the nose of the vehicle.
Structural	B.Str.1	The body shall resist a point load of 500 <i>N</i> on the bottom plate in the middle of the wheels in the driver compartment.
Safety	B.S.1	Windows shall be made of material which shall not shatter into sharp shards.
	B.S.2	A permanent bulkhead shall completely separate the vehicle's propulsion, power train and energy storage systems from the driver's compartment.
	B.S.3	The bulkhead shall be made of fire retardant materials and construction.
	B.S.4	The bulkhead shall effectively seal the driver's compartment from the power train.
	B.S.5	The bulkhead shall extend at least 5 <i>cm</i> above the highest point of the power train or the driver's shoulders, whichever is the highest.
	B.S.6	The bulkhead shall prevent manual access to the engine/energy compartment of the driver.
	B.S.7	The driver's seat shall be fitted with a safety harness having at least five mounting points to maintain the driver in his/her seat.
	B.S.8	The five independent belts shall be attached to the vehicle's main structure and be fitted into a single buckle. It shall withstand a force of at least 1.5 times the driver's weight (736 <i>N</i> ).
	B.S.9	The driver, fully harnessed shall be able to vacate the vehicle at any time without assistance in less than 10 <i>s</i> .
Monocoque solidity	B.M.1	Any bulkhead shall be capable of withstanding a static load of 700 <i>N</i> applied in a vertical, horizontal or perpendicular direction, without exceeding a 0.3 strain(i.e. in any direction).
	B.M.2	The bulkhead shall extend in width beyond the driver's shoulders when seated in normal driving position with the safety belts fastened.
	B.M.3	The vehicle monocoque shall be wide and long enough to protect the driver's body in case of a frontal or lateral collision.

### 4.3 Material Specification

In the conceptual design phase, the material type for the body has been determined. The body will consist of a combination of a sandwich structure and a carbon fiber laminate. The sandwich structure is still a broad description for a composite which contains an upper and lower skin and a lightweight core. Therefore, a choice must be made for both the skin layer and the core material. First, the choice for the skin layer material is discussed. Afterwards, the choice for the core material is discussed.

#### 4.3.1 Laminate and Sandwich Skin Layer Material

For the skin layer, carbon fiber will be used. This was already determined in the conceptual design phase. Since Ten Cate is one of the main sponsors of the Eco-Runner, the choice of carbon fiber will be limited to their supply. High modulus carbon fiber will be the best choice of carbon fiber. At the moment Ten Cate, a company specialized in materials technology, sponsors Toray Torayca T3000 carbon fiber in 0°/45° 100 *gr/m<sup>2</sup>* weave. This is an intermediate modulus carbon fiber. A possible alternative and improvement would be using high modulus carbon fiber such as Toray Torayca M46J delivered by Ten Cate. The most important properties for both the intermediate and high modulus fibers are shown in

Table 4.2 and its composite properties are shown in Table 4.3. Although high modulus carbon fiber has more favorable properties than the intermediate carbon fiber, the price is more than twice as high. In order to obtain a better structural performance and in order to save weight on the composite structure, the M46J fiber should be used for a same fabric. Still, with the T3000 fiber good performances can be obtained. In both cases a 0°/90°-weave should be used with a 93 gr/m<sup>2</sup> density. A twill weave prepreg fabric with this fiber would have a ply thickness around 0.25 mm.

In combination with these fibers, epoxy TC350, from Ten Cate, resin designed to use for low temperature vacuum bag cure processing must be used.

Table 4.2: Fiber properties of Torayca T3000 and Torayca M46J

Fiber properties	Torayca T3000	Torayca M46J
Tensile strength 0° [MPa]	4210	4210
Tensile Modulus 0° [GPa]	230	436
Maximum Strain %	1.8	1.0
Density [kg/m]	1.78	1.82
Filament diameter [μm]	7	5

Table 4.3: Composite properties of Torayca M46J, using epoxy resin, 60% fiber volume [1]

Composite properties	Torayca T3000 UD composite	Torayca M46J UD composite
Tensile strength 0° [MPa]	2050	2210
Tensile modulus 0° [GPa]	130	265
Strain %	1.4	0.8
Compressive strength 0° [MPa]	1570	1080
Compressive modulus 0° [GPa]	125	225
In plane shear strength [MPa]	98	59
Tensile modulus 90° [MPa]	80	49

### 4.3.2 Sandwich Core Material

For the core material, three main types of materials can be chosen. Balsa wood, foam and honeycomb structure. Balsa wood has a high compression and shear strength, excellent fatigue performance, is lightweight and easy to shape. Nevertheless the structural properties decrease in moist conditions. Advantages of foam are that it is lightweight, moisture resistance, easy to handle, flexible and durable. The specific structural properties are less than those of honeycomb. On the contrary, this is the major advantage of honeycomb: the specific structural properties are very high, especially the compressive strength. Though, it is expensive and more difficult to shape and cut in a mold.

In Table 4.4 the structural properties and specific structural properties are shown of the three possible core materials. Honeycomb has in general the best specific structural properties. For this reason honeycomb will be used as core material in the sandwich structure.

A wide range of products are available for the honeycomb core. Aluminum is a commonly used material for honeycomb core, since it has a low cost and high structural properties. It is however difficult to shape and not corrosion resistant. Another commonly used material is Nomex. This aramid fiber honeycomb structure is fire retardant which is a requirement for the bulkhead of the body. It is also corrosion resistant, easy to shape, easy to process and has good strength-to-weight ratios. It is slightly more expensive compared to aluminum honeycombs. The good strength-to-weight ratio and the fire retardant property were decisive to chose Nomex as core material.

Nomex, commercial grade, honeycomb is available in different cell sizes and thicknesses. Three of them are compared. In Table 4.5 their properties are stated. For these three types the first figure

Table 4.4: (Specific) structural properties of foam, aluminum honeycomb and balsa wood

	Foam (DIAB HP200)	spec.	HexWeb® CR III 1/4-5052-.0025	spec.	DIAB ProBalsa PB Standard	spec.
Density [ $kg/m^3$ ]	200		83		155	
Compr. strength [ $MPa$ ]	5.4	0.027	5.45	0.066	12	0.077
Compr. modulus [ $MPa$ ]	310	1.55	1600	19.277	4000	25.806
Tensile strength [ $MPa$ ]	7.1	0.035	10	0.120	13.5	0.087
Shear strength [ $MPa$ ]	3.5	0.017	1.83	0.022	3	0.019
Shear modulus [ $MPa$ ]	74	0.37	244	2.939	166	1.071

stands for the cell size ( $mm$ ), the second figure stands for the density ( $kg/m^3$ ). The ANA-4.8-48 Nomex honeycomb is chosen, since it has the highest specific strength properties. For Table 4.5 the L-direction is defined as the direction of the driving and W-direction is perpendicular to the L-direction as shown in Figure 4.1.

Table 4.5: Mechanical properties for Nomex honeycomb

	ANA-3,2-48	ANA-4,8-32	ANA-4,8-48
Compressive strength [ $MPa$ ]	2.4	1.2	2.4
specific	0.05	0.0375	0.05
compressive modulus [ $MPa$ ]	138	75	140
specific	2.875	2.344	2.917
shear strength (L-direction) [ $MPa$ ]	1.25	0.7	1.2
specific	0.0260	0.0218	0.025
shear modulus (L-direction) [ $MPa$ ]	40	29	40
specific	0.833	0.906	0.833
shear strength (W-direction) [ $MPa$ ]	0.73	0.4	0.7
specific	0.0152	0.0125	0.0145
shear modulus (W-direction) [ $MPa$ ]	25	19	25
specific	0.5208	0.594	0.5208

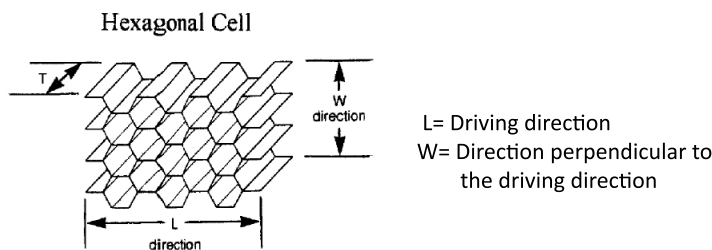


Figure 4.1: Explanation of L-, T- and W-direction for Nomex honeycomb

## 4.4 Design for Load Cases

Before, during and after the race, loads will act on the Eco-Runner body. Several load cases are important to consider for the design of the body structure. In this section, the most crucial ones will be analyzed for the structural design of the body. First, a brief description of the design method is given. Then, each crucial load case will be discussed. The outcome for the body laminate and sandwich structure is given afterwards.

#### 4.4.1 Design Method

Crucial load cases are used as input to determine the sandwich and laminate lay-up for the body. First, with the use of common knowledge (e.g. applying similar loads on a paper fold structure and look at the deformations) and basic physical equations, an estimation for composite lay-up and thicknesses is made. Secondly, these configurations will be optimized and verified with Finite Element Method (FEM) software. A CAD-model of the Eco-Runner is meshed with the program Abaqus and loads are applied on this model. This program operates dimensionless, but since every input is given in SI-units, the outcome will also be in SI-units. First, a body with the current lay-up of Eco-Runner is used. Afterwards, reinforcements are located on critical areas and a second simulation is done. This method gives an understanding in the determination of the structural design of the body. The side windows are discarded in the structural design since their size and position were not determined yet.

#### 4.4.2 Load Cases

##### Load case I: lift off vehicle

During the life time of the vehicle, it will be taken off the ground for transportation or for better accessibility for the subsystems. In most of the cases the body will not include the pilot. If the vehicle, including the pilot, has to be cleared from the race track (i.e. due to a crash or failure) it will be lifted up by two marshals. This will cause serious bending moments and torsion loads on the vehicle. The vehicle must be designed such that this situation will not cause body failure. This load case is defined with the next loads:

- A downward pressure acts on the  $0.5 \text{ m}^2$  seat, corresponding to the pilot weight. [500  $N$  resulting in 1000  $Pa$ ]
- A distributed load corresponding to the vehicle weight acts downwards over the complete vehicle. [300  $N$  resulting in 200  $Pa$ ]
- Two concentrated reaction loads at the front and rear vehicle representing the lifting of the vehicle. [800  $N$  resulting in 4000  $Pa$ ]

This load will cause some bending moments and stresses into the body. As can be seen from Figure 4.2, the highest stresses and displacements would occur around the section cut for the front window. Therefore, an extra layer of the carbon fabric in  $0^\circ/90^\circ$  direction will be placed around it. With this reinforcement, the simulation for the body results only in small stresses around this area.

##### Load case II: braking on a slope

Braking on a slope of 20% will result in a load transfer of the wheels to the suspension into the body. A total braking force of 384  $N$  can occur, taken a 2.5 $g$  load factor into account. Therefore, the attachment of the rear suspension must be able to handle 384  $N$  and each attachment of the front suspension must be

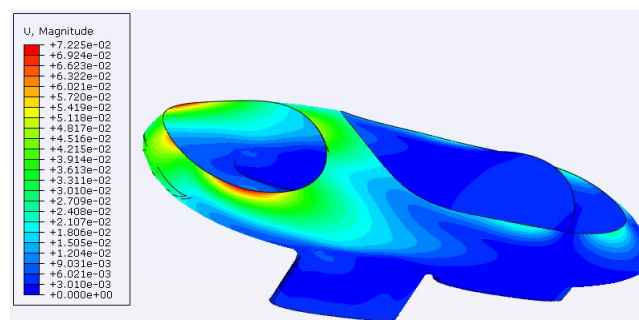


Figure 4.2: Displacement on the body, perpendicular to the skin, in the lift off load case using current Eco-Runner lay-up

able to handle 192  $N$ . This single load case is not critical for the monocoque structure. Therefore, this load will be discussed within the maximum load cases of the suspension.

### Load case III: insert of the pilot

When the pilot enters the vehicle, a small area of the bottom of the body must be able to handle the weight of the pilot. The seat is considered to have a length of 0.160  $m$  and a width of 0.350  $m$ . This results in a surface area of 0.056  $m^2$ . Including a safety factor of 1.5, a total weight of 750  $N$  acting on this surface an pressure of 13000  $Pa$  acting on this surface can be considered. For simplicity an equally distributed pressure is assumed.

The determination of the thickness of the sandwich panel is based on the deflection of a sandwich plate as in Equation 4.1 [15], which represents the deflection for a simply supported sandwich plate. In Equation 4.1,  $\delta$  is the deflection which is set on 0.001  $m$  constant,  $K$  is 0.0107[-],  $q$  is the pressure,  $b$  is the plate width,  $\mu$  the Poisson's ratio,  $E_f$  the tensile modulus,  $t_f$  the skin thickness and  $h$  the overall thickness of the sandwich panel. Using the mechanical properties of the high modulus cross-ply carbon fiber fabric and the honeycomb sandwich core, the required panel thickness is approximately 11.5  $mm$ , thus the core thickness should be 10  $mm$ .

$$\delta = \frac{2 \cdot K \cdot q \cdot b^4 \cdot (1 - \mu^2)}{E_f \cdot t_f \cdot h^2} \quad (4.1)$$

A simulation with Abaqus is made for such a simply supported honeycomb sandwich panel in order to verify the previous calculation. According to the simulation, the total panel and the core thickness could be respectively decreased to 7  $mm$  and 5  $mm$  to obtain a 1  $mm$  deflection.

### Load case IV: maximum loads from suspension

The suspension will transfer loads from the wheels into the body. The maximum loads are defined as the maximum loads the suspension will have to handle. The maximum vertical load for each wheel is 1400  $N$  and occurs when riding on a bump. The maximum longitudinal load for each wheel is 320  $N$  and occurs when braking. Lastly, the maximum lateral load for each wheel is 250  $N$  and occurs during turning. This implies that the body will have to withstand these loads in a worst case scenario situation, where they all act together on one wheel. With these loads, especially the area around the attachment of the suspension shall be investigated for stresses and displacements.

First, the loads coming from the front suspension are examined. As can be seen in Figure 4.3 major displacements and stresses occur on the location where the suspension is attached to the body, especially on the bottom center region of the body. Displacements of almost 10  $mm$  can occur. This area will be stiffened using sandwich panels on the bottom of the Eco-Runner. Since there will be a sandwich panel at the seat already, this panel can be extended towards the front upto the front of the fairings.

For the loads acting on the rear suspension, major stresses build up on the rear bottom of the body and around the cut for the top cap. This is noticeable in Figure 4.3. Therefore, around the cut for the top cap an extra layer of the carbon fabric in  $0^\circ/90^\circ$  direction will be placed around it. Although the bulkhead helps to carry loads around this cutout, the complete region around the top cap cut will be reinforced since some displacements occur at the front of this region. On the rear bottom, a sandwich panel will be used to increase the stiffness around the rear suspension.

### Load case V: bulkhead

Three load cases will occur on the bulkhead. One is determined from a safety requirement, which states that the top of the bulkhead should be able to withstand a vertical load of 700  $N$ . Another load case is due to the fact the pilot leans against the bulkhead. Since the bulkhead will have an area of 0.240  $m^2$  and assuming the full driver weight can act on the bulkhead, a pressure of 1850  $Pa$  is applied on it. For simplicity an equally distributed pressure over the whole bulkhead is assumed. The third load case

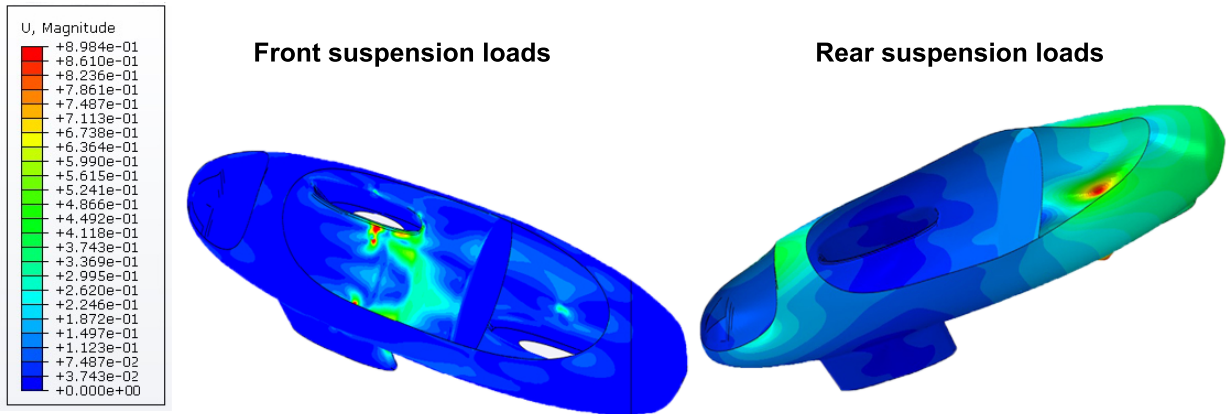


Figure 4.3: Displacement on the body, perpendicular to the surface direction, from the front and rear suspension loads using current Eco-Runner lay-up

comes from the installed seat belt inserts. This last one is described later within the section about inserts.

As can be seen from Figure 4.4 the displacements due to the load cases are too large if only a four layer laminate structure is used for the bulkhead. Therefore, a sandwich panel structure will be designed. Buckling could occur if the sandwich panel is made too thin.

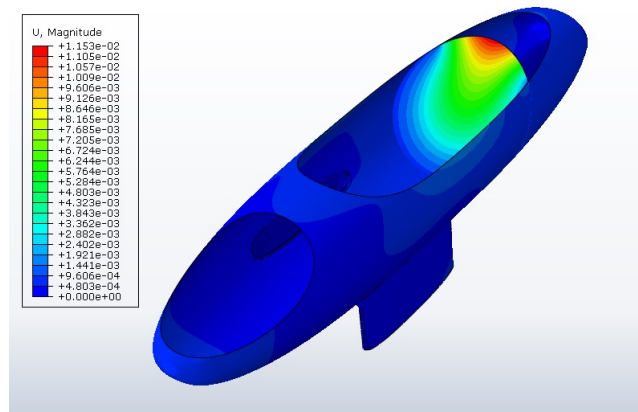


Figure 4.4: Displacement on the bulkhead using a  $0^\circ/90^\circ / + 45^\circ / - 45^\circ$  lay-up

Using Equation 4.2 [15], the maximum sandwich panel buckling load, with force  $F$  equal to  $700\text{ N}$ , length  $l$  and width  $b$  both  $0.45\text{ m}$ , carbon fabric tensile modulus  $E_f$  of  $70\text{ GPa}$ , total skin thickness  $t_f$  of  $0.001\text{ m}$  and core shear modulus  $G_c$  of  $220\text{ MPa}$  the thickness of the sandwich panel could be estimated. This results in a core thickness of  $0.015\text{ m}$ .

$$F_b = \frac{\pi^2 D}{l^2 + \frac{\pi^2 D}{G_c h b}} \quad \text{with} \quad D = \frac{E_f t_f h^2}{2} \quad (4.2)$$

To check if this panel could withstand the load of the driver leaning to the bulkhead, Equation 4.1 is used. The thickness for an allowable deflection of  $0.005\text{ m}$  is estimated. This would result in a core thickness of  $0.015\text{ m}$ . Buckling is therefore the crucial load on the bulkhead. Figure 4.4 shows that the largest deflection on the bulkhead occurs at the top. Instead of increasing the total core thickness of the bulkhead, adding an extra layer of carbon fiber fabric around the top decreases also the deflection.

The previous result is optimized and verified using Abaqus and the final outcome will be a  $0.010\text{ m}$  core thickness and a total sandwich thickness of  $0.011\text{ m}$  with an extra reinforcement at the top.

## 4.5 Final Body Lay-up and Mass Estimation

The body is divided into several sections where different lay-up configurations are used. Most of the body will consist of a two layer laminate. This section is indicated in Figure 4.5 as 'Body skin laminate'. Two prepegs with T300 carbon fiber, twill weave,  $0^\circ/90^\circ$  and a thickness of  $0.2\text{ mm}$  are placed above each other. One layer is placed in  $0^\circ/90^\circ$  and one is placed in approximately  $45^\circ$  direction. This direction is orientated with respect to the symmetry plane.

A large section of the floor will consist of a sandwich structure to increase the stiffness and to improve the load transfer from the suspension. This sandwich structure will have a total thickness of  $11\text{ mm}$  with a core thickness of  $10\text{ mm}$  and each skin face consist of the same two layer laminate as the body skin. This sandwich configuration will also be used for a section on the side fairings of the front wheels since the suspension will also be attached on this side. This makes it possible to install inserts into this region of the monocoque. The core thickness for the seat will be thicker, namely  $12\text{ mm}$ , since it has to cope with the load from the pilot entering the vehicle. The face layers are the same as the bottom sandwich structure. The bulkhead will have a total thickness of  $16\text{ mm}$  with a core thickness of  $15\text{ mm}$  and the same skin layers as the the other sandwich structures in the body.

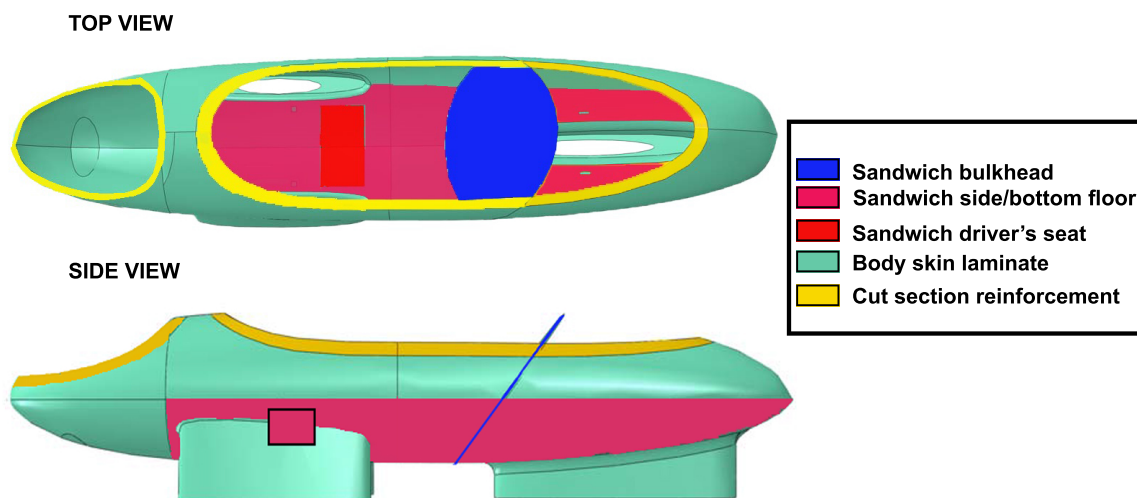


Figure 4.5: Top and side view of the body with indicated section laminate and sandwich structures

Several sections are cut out of the body, namely for the top cap, front and side windows. These cuts will consist of the normal two layer fabrics such as the rest of the body skin reinforced with an extra layer of the  $0^\circ/90^\circ$  twill weave fabric in  $0^\circ$  direction with respect to the symmetry plane.

An overview of thicknesses and mass estimations can be found in table 4.6. The top cover, which will be placed on top of the monocoque will be non structural. It has a surface area of  $0.760\text{ m}^2$ , it will consist of two carbon fabric layers and have a total mass of  $0.456\text{ kg}$  without solar cells. The total monocoque mass, including the top cover, will be  $6.946\text{ kg}$ . This is a mass reduction of around 10% compared to the current Eco-Runner body.

## 4.6 Inserts

Special attention must be given to the loads and installation of inserts on the laminates and sandwich structure in the body. Inside the body some inserts will be placed for the attachment of components.

Table 4.6: Thicknesses and mass of each monocoque section

	Skin[mm]	Core[mm]	Total thickness [mm]	Mass [kg]
Body skin laminate	0.5	n/a	0.50	2.300
Section reinforcement	0.75	n/a	0.8	0.147
Sandwich panel driver's seat	2 x 0.5	12	13	0.135
Sandwich panel bottom floor	2 x 0.5	10	11	3.108
Sandwich panel bulkhead	2 x 0.5	10	11	0.650
Top cover (non structural)	0.5	n/a	0.5	0.456
Total	n/a	n/a	n/a	6.796

#### 4.6.1 Loads on Inserts

Attachment by inserts and bolts will be used if tension loads occur and bonding (glue) is not effective. One example of a component that will be attached to the body is the five point harness. This will be mounted by three inserts onto the body and by two inserts onto the bulkhead. In worst case scenario two bolts will handle a load of 1.5 g times the pilot's weight. Therefore, one bolt must handle around 550N. Besides, inserts will be used to attach the front and rear suspension. A load, of at most 700N, could be transferred through one bolt. According to Bunyawanichakul [16], most potted sandwich panel inserts can handle easily loads up to 3kN without failure of the insert or sandwich panel. These inserts also have a small stress concentration around the insert, especially when a [0°/+45°/90°] carbon fiber lay-up is used around these insert. This is also recommended in the Eco-Runner body.

#### 4.6.2 Insert Type

Two types of inserts are considered to use, namely blind and through threaded as shown in Figure 4.6. The through threaded fasteners are mounted into the top and bottom skin layer, while the blind threaded only is mounted into the top layer and 'floats' around in a filled up section of the core material. The through threaded fasteners will be used since they are stronger and better resistant against shear. However, a disadvantage using this type is the fact that the fastener must be mounted through both skin layers of the sandwich structure. Two different head styles for the fastener can be used. These are shown in Figure 4.7[17]. The flushed style is preferred for its smoothness in the body's finishing.

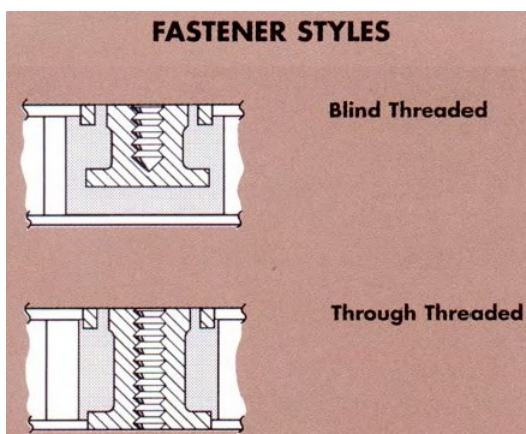


Figure 4.6: Fastener styles for sandwich panels

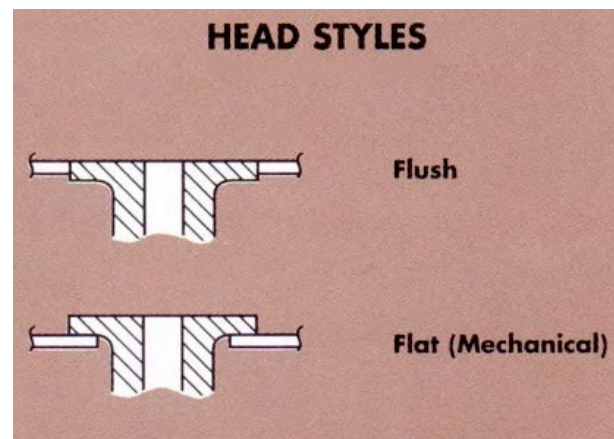


Figure 4.7: Flat and flush head styles for fasteners

#### 4.6.3 Installation of Inserts in Sandwich Structures

For structural reasons the best way to install the inserts is to place them into the right place during the molding of the monocoque structure. Since through threaded, flushed inserts will be used, the length of the insert will be equal to the thickness of the sandwich panel. To increase the strength around a

fastener, they will be reinforced by an extra  $[+45^\circ]$  carbon fiber lay-up. To fill the empty space between the honeycomb core and the insert, epoxy is injected through one of the potting holes with a sealant gun. This permits venting through the other hole which ensures a completely uniform fill, as shown in Figure 4.8.

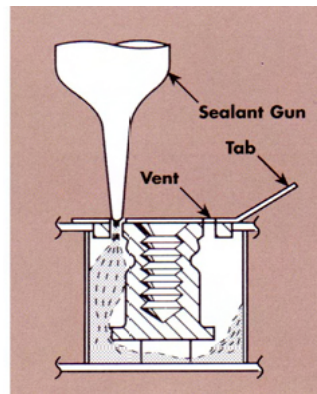


Figure 4.8: Sealing empty space around insert in a honeycomb core

## 4.7 Production of the Body

In this section, the production method of the monocoque structure is first presented. Then, the production of the mold is discussed and special attention is paid to the alignment and joining of the molded body parts. Finally, the molding process is discussed.

### 4.7.1 Production Method

#### Prepreg vs wet lay-up

A Nomex honeycomb sandwich structure is chosen for the body, leaving only the possibility of prepreg and wet lay-up as production method to ensure full and uniform impregnation of the fibers. To obtain the optimal method a trade-off is made. For the trade-off criteria mechanical properties, production complexity and overall cost are used. Higher mechanical properties will result in a lower mass, one of the design objectives. The production complexity and costs criteria are added to weigh the feasibility of the options. Wet lay-up is cheaper than prepreg as the molding, tooling, and material costs are lower. However, this could be compensated by lower labor cost. The mechanical and thermal properties of wet lay-up might be compromised in order to keep the resin low in viscosity to be workable. The quality of production depends on the skill of the producers. The resin level for prepreg is set by the manufacturer, for ensuring the quality. The thickness of the laminate can be controlled better using prepreps. They will result in a lower void content and a higher fiber content can be obtained compared to wet lay-up, which decreases the weight of the structure for comparable mechanical properties. The prepreps are easy and clean to work with, increasing the quality of production for inexperienced producers. At this point, exact values are unknown for cost, difference in mechanical properties and importance of trade off criteria. Therefore, the trade-off criteria are treated equally and plus or minus signs are assigned for the score. After the trade-off, the prepreg production method is chosen. The better mechanical properties and lower production complexity outweigh the cost increase. The trade-off is shown in Table 4.7.

### 4.7.2 Mold Selection

The mold has three main requirements. It should be releasable, have a maximum thermal expansion difference of  $5 \text{ mm}$  with the body and shall withstand an oven temperature of  $150^\circ\text{C}$ . The release of the mold is determined by the parting line, while the mold material determines the thermal expansion coefficient and the maximum servicing temperature. A negative mold was chosen, because the outside

Table 4.7: A trade-off between wet lay-up and prepreg technique

	Mechanical properties	Production complexity	Cost
Weight factor	33.3	33.3	33.3
Wet lay-up	-	-	+
Prepreg	+	+	-

facing should be as smooth as possible for aerodynamic reasons. A mold with a horizontal parting line is considered, since a horizontal parting line offers much more advantages compared to the vertical parting line. For a horizontal parting line, no sandwich panel is split. For a laminate, no core needs to be glued together resulting in a lighter and simpler joint. The location of pick-up points for the suspension, left and right, will have a higher symmetry accuracy. Since the fairings of the body will have camber, they cannot be laminated together in one mold with the bottom part of the body. The mold for the under-body should be divided into three molds. This allows the fairings to be laminated together with the under-body. If one mold is used for the under-body the fairings need to be laminated separately for the monocoque to be releasable and joined afterwards. For the three part molds there is no seam, nor is the extra reinforcement required for the joint. Complexity of the overall production is similar. The molds will become more complex as these need to be joined airtight, but the fairings do not need to be joined to the under-body afterwards. The lower mass and the smooth transition from fairing to body are the reasons to choose a three part bottom mold. The mold division is shown in Figure 4.9. The selected carbon fiber has a thermal expansion coefficient (CTE) of  $-0.43 \cdot 10^{-6} \text{ m/mK}$ . The mold has a length of  $3 \text{ m}$  and the temperature difference is  $132 \text{ }^\circ\text{C}$ . Five materials were considered for the mold and their properties are presented in Table 4.8. The length increment is computed by the multiplication of the mold length, CTE and temperature difference. Making a mold of carbon fiber is the only possibility to have a mold with an acceptable equal CTE. To create this carbon fiber mold, polyurethane foam or wooden positive mold is used, from which a carbon fiber mold is made with vacuum infusion. The resulting mold shall have the thermal properties as set in the requirements.

Table 4.8: Considered materials with their thermal properties [2]

	CTE	Length increment [mm]	Max servicing temperature [ $^\circ\text{C}$ ]
ABS-glass fiber reinforced	$39.4 \cdot 10^{-6}$	15.60	80 – 200
Aluminum	$22.2 \cdot 10^{-6}$	8.79	150 – 250
Polyurethane foam	$55 \cdot 10^{-6}$	2.18	50 – 80
Wood	$3 \cdot 10^{-6}$	0.12	80 – 150
Carbon fiber	$-0.43 \cdot 10^{-6}$	-0.017	80 – 215

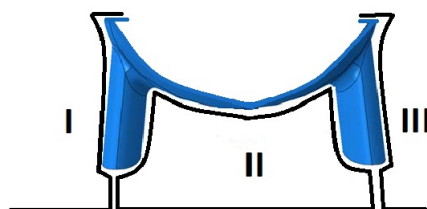


Figure 4.9: Mold for bottom part of body, consisting of 3 parts: I , II, III

### 4.7.3 Alignment and Joining of the Body Halves

The main requirement for the alignment of the two halves is high accuracy. The best option is to provide the alignment already on the positive mold. This is the only part that is machined and in this way

maximum benefit can be taken from the low tolerances of milling by CNC .

Holes can be milled in the flanges of the two positive molds at the same locations. Rods can be placed in these holes, after which the negative mold can be laminated around these rods. The same process can be applied for laminating the monocoque halves. When the two halves are laminated, they can be aligned with the aid of the rods. The cut-out for the top panel can already be cut out providing access for the bonding of the two halves.

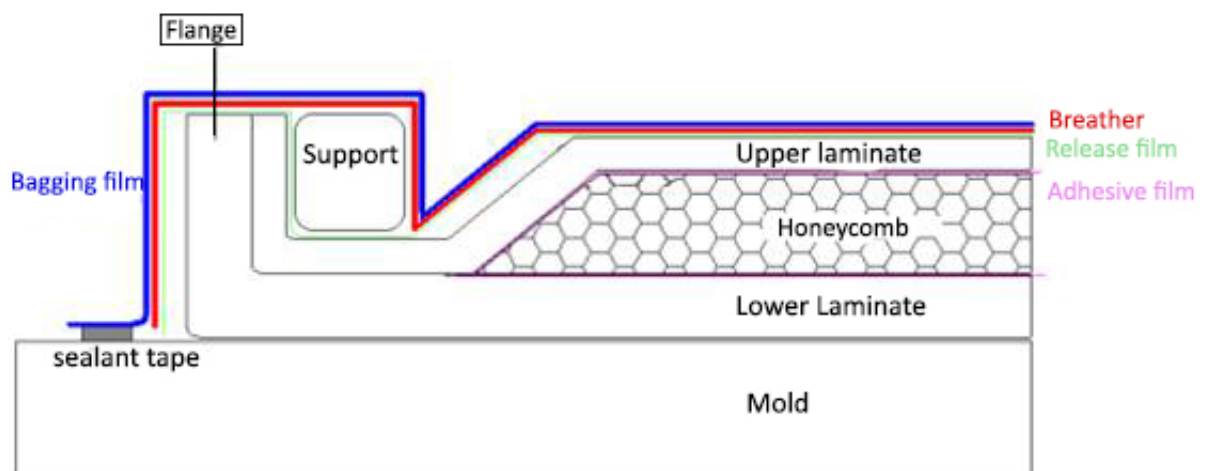


Figure 4.10: lay-up and vacuum bagging process for a combined laminate and sandwich structure at the end of sandwich structure

The bonding can also be performed on the flanges as shown in Figure 4.10. Bolts or epoxy were considered for bonding. Bolts will lead to stress concentrations, extra reinforcements, but makes the parts dismantling. Epoxy will provide a uniform distributed bonding. For epoxy, the surface should be a bit rough in order for the adhesive to bond. This can easily be achieved by using a peel-ply during the production process on the flange. Epoxy makes the attachment of the two parts irreversible. Due to stress concentration of bolts and the fact that the two body parts shouldn't be dismantlable, epoxy is chosen.

#### 4.7.4 Monocoque Production

Since the mold type and material are defined, the production of the monocoque body can be done. Vacuum bagging will be applied to fabricate the body. The top side and the bottom side of the monocoque will be made separately.

First a release agent is applied on the mold. Next, the carbon fiber layers forming the outer skin are placed into the mold. The fibers will be cut with CAD software to increase accuracy. The layers used are preregs. Each layer will be placed in a predefined direction and at some places more carbon fiber layers will be used for better structural performance. Using preregs will cause a gloss, smooth outer skin. Inserts should already be positioned during the lay-up. This skin layer will form the first skin face for the sandwich structures in the body and the total skin for the laminate structure. This first layer will be vacuum bagged such that this skin layer for the sandwich structure cannot buckle into the honeycomb core.

To create this vacuum environment, the air-tight mold is sealed with a vacuum bag. A vacuum pump is connected to this air-tight system with a plastic tube and the complete system is bleed under vacuum.

This curing can be done at ambient temperature.

After this first vacuum bagging, an adhesive film is applied on the surface. This film will connect the face skin to the honeycomb core. On the adhesive film, a flexible Nomex honeycomb will be placed. The adhesive film and the core will only be placed at the positions where a sandwich structure has to be. Attention has to be paid to the lay-up of the honeycomb where the region is curved. On these places, the core should stay in contact with the face skin. On top of this core, another adhesive film is applied and the carbon fiber prepregs for the bottom skin are positioned.

Then, the composite is vacuum bagged for a second time and cured at ambient temperature. When the parts are completely cured, they are inspected for voids or other manufacturing flaws. When the top and bottom parts pass the inspection, they are placed on top of each other, aligned and bonded together using the technique of wet lay-up. At the same time, the bulkhead is bonded into the body.

### Top cover fabrication

The removable top cover of the body also will be manufactured through vacuum molding. The only difference with the other body parts is that this part will be a full laminate and not a sandwich structure. In the design it is chosen that the top cover will not participate in the load carrying of the body.

### Windows

The windows will be made out of poly-methyl methacrylate or poly-carbonate. These are transparent polymers which easily can be shaped by vacuum forming. The windows will be bonded into the body from the inside. They should be shaped such that the window borders are trimmed. This will result in a smooth transition from the outer body skin to the window as shown in Figure 4.11



Figure 4.11: Installation of a window on the monocoque body

### Wheel cover fabrication

The wheels will be concealed on the inside of the body with a removable cover which will protect the pilot from the rotating wheels. These covers will be non-structural. Therefore, they will be made out of one or two carbon fiber fabrics. This laminate will be processed in the same way as the body will be manufactured. A mold will be made, the layers will be inserted into a mold, treated with release agent and cured using vacuum bagging.

## 4.8 Verification and Validation

The number of layers, thicknesses and directions of layers for the composite body are based on structural and mechanical equations and formulas. These configurations were verified with FEM software. A CAD-model of the Eco-Runner is meshed with the program Abaqus and loads are applied on this model. Using this software, it is assured that structural failure shall be avoided in all possible load cases.

The production method of the monocoque body should be validated. This should be done by testing the proposed production method. The way the sandwich panel will be molded should be applied first on a separate piece. If the outcome has the desired quality, the fabrication technique could be applied for the full monocoque structure.

## 4.9 Cost Budget for the Monocoque Body

Several elements will contribute to the cost budget of production of the monocoque body. Material, mold, labor and processing costs will form the total costs for the body. It is advisable for the Eco-Runner team to try to discard most of these costs from the total costs by sponsoring. Ten Cate is the main sponsor for the carbon fibers. To laminate the body including the bulkhead and the top cover, a total area of  $15 \text{ m}^2$  of prepreg Toray T300 twill weave,  $0^\circ/90^\circ$  carbon fiber is needed. This has a market price of about €1500 [18]. To create the sandwich structures, also  $1.5 \text{ m}^2$ , Nomex honeycomb is needed. This has a market price around €80 [18]. It is very difficult to estimate the production cost of the composite mold itself. These costs can vary from €500 for a cheap mold up to several thousand of euros. Now, a composite mold is proposed. Using an aluminum mold for the monocoque body would increase the mold cost for at least 5000€. However, the Eco-Runner team had the mold sponsored by NedCam. It is therefore hoped that this cost can be discarded from the total cost budget. The production, including lay-up, laminating, vacuum bagging and curing, could be done by Eco-Runner team members in collaboration with specialized employees from a sponsored company, such as VaboComposites. The process of hand lay-up and vacuum bagging has a cost around €450 [19]. A total cost estimation for the production of the monocoque body is given in table 4.9.

Table 4.9: Cost budget for monocoque body

	Material	Mold	Production	Total
Price [€]	1580	2000	450	4030

## 4.10 Compliance Matrix

The table below shows the compliance matrix for the body structure. Almost every requirement was met. The only requirement that has not been met is B.S.9, since it has to be tested if the driver can get out of the vehicle fast enough.

Table 4.10: Compliance matrix for the body

Category	ID#:	Requirement:	Check
Dimensions	B.D.1	The body mass shall be equal/lower than 11.5 <i>kg</i> .	✓
	B.D.2	The vehicle body shall be wide and long enough to protect the driver's body in case of a frontal collision into a wall or lateral collision of a different vehicle at an impact speed of 35 <i>km/h</i> equivalent to 20 <i>kN</i> .	✓
	B.D.3	The vehicle shall be designed for any driver position, except for head first.	✓
	B.D.4	A minimum distance of 10 <i>cm</i> shall be present between the driver and the nosecone of the vehicle.	✓
Structural	B.Str.1	The body shall resist a point load of 500 <i>N</i> on the bottom plate in the middle of the wheels in the driver compartment.	✓
Safety	B.S.1	Windows shall be made of material which may not shatter into sharp shards.	✓
	B.S.2	A permanent bulkhead shall completely separate the vehicle's propulsion, power train and energy storage systems from the driver's compartment.	✓
	B.S.3	The bulkhead shall be made of fire retardant materials and construction.	✓
	B.S.4	The bulkhead shall effectively seal the driver's compartment from the power train.	✓
	B.S.5	The bulkhead shall extend at least 5 <i>cm</i> above the highest point of the power train or the driver's shoulders, whichever is the highest.	✓
	B.S.6	The bulkhead shall prevent manual access to the engine/energy compartment of the driver.	✓
	B.S.7	The driver's seat shall be fitted with a safety harness having at least five mounting points to maintain the driver in his/her seat.	✓
	B.S.8	The five independent belts shall be attached to the vehicle's main structure and be fitted into a single buckle. It shall withstand a force of at least 1.5 times the driver's weight (736 <i>N</i> ).	✓
	B.S.9	The driver, fully harnessed shall be able to vacate his/her vehicle at any time without assistance in less than 10 <i>s</i> .	?
Monocoque solidity	B.M.1	Any bulkhead shall be capable of withstanding a static load of 700 <i>N</i> applied in a vertical, horizontal or perpendicular direction, without exceeding its strain by 0.3 (i.e. in any direction).	✓
	B.M.2	The bulkhead shall extend in width beyond the driver's shoulders when seated in normal driving position with the safety belts fastened.	✓
	B.M.3	The vehicle monocoque shall be wide and long enough to protect the driver's body in case of a frontal or lateral collision.	✓

## 4.11 Conclusion and Recommendations

The monocoque body will consist of a combined sandwich and laminate structure. Toray T300 carbon fiber,  $0^\circ/90^\circ$  plain weave fabric, is chosen for the laminate and skin layers of the sandwich structure. The core material for the sandwich structure will be Nomex honeycomb. The thicknesses, number of fabric layers and fiber directions are based on different load cases acting on the body. A body lay-up configuration providing sufficient strength and stiffness could be created within the mass budget. Including a top cover of  $0.456\text{ kg}$ , the total body structure mass shall be  $6.946\text{ kg}$ .

Inserts shall be placed in regions on the body where sandwich panels are situated. For the production of the body, first, a top and bottom part of the body will be molded using vacuum bagging. For the bottom part, the mold will consist of three parts, such that the body and wheel fairings are integrated and a smooth transition is created. The top and bottom part of the body are laminated together using wet lay-up. At the same time, the bulk head will be laminated into the body using wet lay-up.

The total cost for the production of the body is difficult to estimate since most of the cost can be discarded due to sponsorship of several companies. If no sponsors could be obtained, the largest cost would be the carbon fiber fabrics (€1500), the production of the mold (€500 up to €2000), and labor costs if some processes have to be outsourced.

One point of possible improvement is the view from inside the body. Especially the shape and position of the side windows should be investigated. It is also recommended to investigate which parts of the production could be outsourced to sponsored companies in order to reduce costs. Furthermore, special effort should be spent for the sponsorship of carbon fiber with a higher modulus, now intermediate modulus is delivered. The use of high modulus carbon fiber could lead to less fabric layers and therefore weight saving. The lay-up of the monocoque could still be optimized. This can be done by investigating and observing how the new monocoque body will react on real life loads. Lastly, the integration of the solar cells on the top cover should be specified further.

# 5 Suspension

## 5.1 Introduction

This chapter describes the detailed design process of the front and rear suspension. For the detailed design, the rear suspension and the steering system are combined. The brakes are not designed in detail, but are considered during the design in terms of space and loads. The sections correspond to phases in the design process. First, the previous work is analyzed. Then, the functions and requirements are reconsidered. A sensitivity analysis and contingency management are also discussed for these requirements. The detailed design process of the front and rear suspension is described and then verified. Then, a manufacturing plan is set-up and proposals are made for validation tests. Finally, a cost and mass budget is constructed and recommendations are made for further work. The design process is also shown in Figure 5.1.

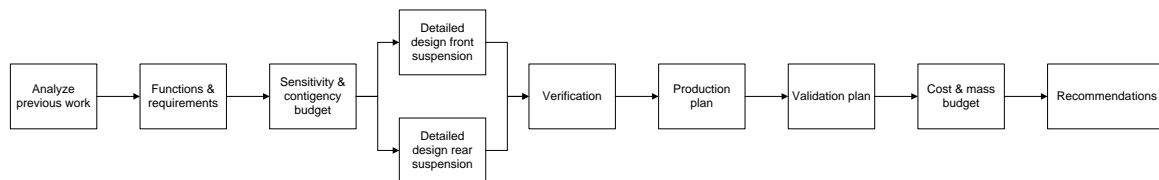


Figure 5.1: Design process of the suspension

### 5.1.1 Previous Work

In the conceptual design phase, the rear wheel steering and rear wheel driven option were chosen. Rear wheel steering was based on the reduction in frontal area and aerodynamic drag. A Mitsuba M00512-IV in-wheel motor was chosen for efficiency and weight reduction, resulting in rear wheel steering for a symmetric traction force with the lowest drag. For the front suspension an embedded system was proposed, yielding the lowest mass and highest stiffness compared to size. The detailed design continues with this concept.

The only option considered in the mid-term report [13], that could be integrated with a steering system, was a fork. However, there are more solutions that integrate suspension and steering. The fork concept was not analyzed further in the detailed design. This decision was made after a meeting with the current Eco-Runner team. The fork constrains all degrees of freedom on only one attaching point in the body. This is not beneficial for reliability. The load introduction in only one point can lead to heavy reinforcements to meet the strength and stiffness requirements. The contact point and turning point are at a large distance from each other, resulting in a large turning area required for the wheel. New concepts were considered for the rear suspension and a different one was selected in the detailed design.

### 5.1.2 Functions and Requirements

The goal of the design process is to minimize weight and drag. The suspension system contributes to this goal by optimizing the design for minimum weight, high lateral and high normal stiffness. Though the total suspension mass is only 7% of the total vehicle weight, every kilogram that can be saved matters for the energy efficiency. A high lateral and normal stiffness will prevent the disc brakes from dragging in the brake claw where the clearance is limited.

The two main functions of the suspension are listed below:

- introduce loads to body: bump, braking, weight and steering;

- steer vehicle with stability and feedback to the driver.

To succeed in performing these functions, requirements are set. The main requirements for the suspension are presented in Table 5.1. The dynamic normal force is computed for a spring-mass system when the vehicle hits a 1.5 cm bump with a velocity of 25 km/h. These calculations are described in Appendix B. The braking force is equal to the force needed to keep the vehicle immobile on a 20% inclined slope. The lateral force is computed with a steady-state tricycle vehicle cornering model described in the mid-term report [13].

Table 5.1: Requirements for the suspension system

Category:	ID#:	Requirement:
Dimensional	Su.D.1.F.	The total front suspension system shall fit within the body and allow room for the drivers legs.
	Su.D.1.R.	The total rear suspension system shall fit within the body and behind the bulkhead.
Structural	Su.S.1.F	The front suspension shall be able to withstand a dynamic normal force of 2132 N.
	Su.S.1.R	The rear suspension shall be able to withstand a dynamic normal force of 1209 N.
	Su.S.2.	The suspension shall be able to withstand a braking force of at least 279 N.
	Su.S.3.	The suspension shall be able to withstand a lateral force of 250 N.
	Su.S.4.	The suspension shall have a maximum deformation of 0.1 mm in all directions.
Su.S.5.	The suspension shall allow the wheel to be removed from the body for servicing.	

## 5.2 Sensitivity Analysis

Now that the values of the forces are known, the loads are ranked in order of magnitude. This is useful to determine the importance of the loads.

1. dynamic normal force;
2. braking force;
3. lateral force.

The dynamic normal load is about five times larger than the braking force and lateral force, hence the normal load introduction into the monocoque is by far the most critical parameter for the suspension design. In designing the stiffness, the same ranking is used.

## 5.3 Contingency Management

A contingency budget of 3 kg is added to the vehicle mass to compute the forces acting on the vehicle. Extra mass due to the driver, last minute repairs at the event or trapped dirt and water during the race are estimated to be 3 kg. Though the vehicle may have a weight of 30 kg as designed, these factors might cause the vehicle to exceed this weight.

The suspension is designed for absolute worst case scenario: the vehicle hits a bump during a corner while braking. This corresponds to a load case where the maximum normal force, braking and cornering force all happen together at the same time. The suspension will not encounter a higher load during its lifetime, so no extra safety factor is included.

## 5.4 Detailed Design Front Suspension

From the sensitivity analysis the critical load is defined as the normal force exerted from the body on the axle. This load can either be introduced on one side or on both sides of the axle. Though introducing the loads on both sides requires two inserts and two holes in the composite body which need to be reinforced, the deflection and bending moment will be greatly reduced. The mass difference is therefore small and difficult to predict. If the axle is supported on two sides, its deflection is reduced with a factor 64. This is shown in the free body diagrams of a cantilever beam in Figure 5.2 and 5.3, where the maximum deflection is also indicated in the figure. As the mass difference is small and difficult to predict, the only trade-off criterion is the stiffness. This resulted in the choice to support the axle on both sides.

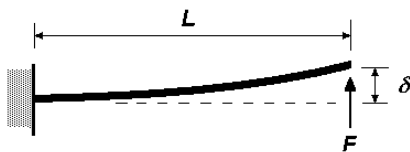


Figure 5.2: One-side cantilever beam [20]

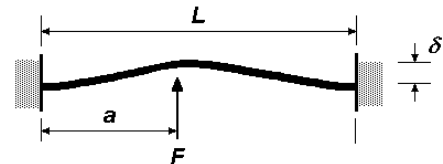


Figure 5.3: Two-sides cantilever beam [20]

For the body a carbon fiber monocoque concept is chosen, offering a high degree of design freedom for the load introduction points, as the entire body is load-carrying. Carbon fiber is an anisotropic material. A carbon fiber epoxy matrix has a tensile strength of  $760 \text{ MPa}$  in longitudinal direction and only  $28 \text{ MPa}$  in transverse direction. It is 27 times stronger in the in-plane direction than out-of-plane. Therefore, to reduce the weight of the monocoque, the vertical load was chosen to be introduced in-plane such that less material is needed. The only location available to introduce loads in-plane is the fairing. The fairing needs to be reinforced around the insert location, but this mass increase is small compared to the reinforcements required for out-of plane load introduction.

The body is optimized for a low frontal area, resulting in little space available at the outside of the wheel. A hand would not fit behind the wheel to release the wheel and an attachment at the outside of the body is not allowed for aerodynamic reasons. The only solution available is to use a thru axle that can be screwed into an insert on the outside of the fairing. This allows the wheel to be removed for servicing.

Several options are still available for the inside bracket. It can simply support the axle or clamp the axle. It can be made out of one piece or two. The brake claw mount can be integrated or a separate bracket can be designed. Integrating the brake claw mount reduces the mass and size as an extra bracket is not required. The brake force can even be used to alleviate the normal load if it is introduced in the upward direction. So the first choice was to integrate the brake claw mount. Tolerances of the disc in the brake claw are very small. To prevent the disc from dragging in the brake claw, alignment accuracy of  $0.05 \text{ mm}$  and a lateral movement of less than  $0.1 \text{ mm}$  are required. For the same reason as the vertical load introduction, it was chosen to clamp the axle on both sides as this will improve the lateral stiffness. This decision implied that a two-piece bracket should be used. A one piece bracket clamping the axle will bend, decreasing the alignment accuracy of the brake claw below the requirement.

Now that the structural concept is chosen, the appropriate material should be selected. The materials considered for each component are steel, aluminum, carbon fiber, titanium and magnesium. The trade-off criteria are specific strength, cost and production complexity. With these criteria, performance is weighed against feasibility. Specific strength is performance, while the feasibility is ensured by cost and production complexity.

All trade-off criteria are treated equally, as the importance of criteria are unknown at this point. The trade-off table is presented in Table 5.3. The scores are based on the material properties as shown in Table 5.2 [3]. The specific strength is the yield strength divided by the density. The relative cost is the cost of the material relative to plain carbon A36 steel. Complexity refers to design, production and

machining complexity. The production and machining of steel and aluminum is well known, machines and tools are available at TU Delft. Titanium is difficult to machine because of its hardness. Carbon fiber has a high complexity because it is more difficult to design, extra tools are required for production and drilled holes need to be reinforced. Magnesium is the fastest machining metal, however magnesium dust is highly flammable.

The score is the value of the material property divided by the maximum value of the five materials, multiplied by five to get a score of 1 to 5. When a minimum value is better, the inverse score is taken. In this way the materials are scored based on their relative ranking to each other.

Table 5.2: Material properties [3]

	Specific strength [ $\frac{kNm}{kg}$ ]	Relative cost	Complexity
Aluminum 2024 (heat treated)	125	12.3	5
Aluminum 7075 (heat treated)	180	13.4	5
High modulus carbon fibers	447	340	1
Epoxy matrix ( $V_f = 0.6$ )			
Magnesium alloy AZ31B	124	15.7	3
Stainless steel alloy 17-7PH	171	12	5
Titanium alloy Ti-6Al-4V	249	132	2

Table 5.3: Trade-off table material choice

Option \ Criterion	Specific Strength	Cost	Complexity	Total
Weight Factor (%)	33,3	33,3	33,3	100
Aluminum 2024 (heat treated)	1	5	5	72
Aluminum 7075 (heat treated)	2	4	5	76
High Modulus Carbon Fibers Epoxy Matrix ( $V_f=0.6$ )	5	1	1	46
Magnesium Alloy AZ31B	1	4	3	58
Stainless Steel Alloy 17-7PH	2	5	5	76
Titanium Alloy Ti-6Al-4V	3	2	2	45

Stainless steel and the aluminum alloys score best and are close together. Assuming the opportunity of supply of the aluminum or steel is the same, it is chosen to optimize for mass and the aluminum 7075 alloy is chosen because it has the highest specific strength. A disadvantage of this alloy is a lower fatigue resistance, but as the lifetime of the Eco-Runner is very short fatigue is not an issue. The axle should be made of steel to meet the stiffness requirement. The diameter cannot be increased as the diameter of the bearings is fixed. If retaining steel bolts are more easily available or much cheaper, it is proposed to use these. The bolts should be retained to prevent themselves from loosening due to vibrations.

The detailed design was drawn, dimensioned and assembled in CATIA. The result is shown in Figures 5.4 and 5.5. Note that the outer insert is integrated in the fairing sandwich structure. The fairing is not shown. In the upper bracket, the brake claw mount is integrated and can be seen at the edges. Parallel to the detailed design phase, the design was verified with the requirements. The verification process is described in Section 5.6.

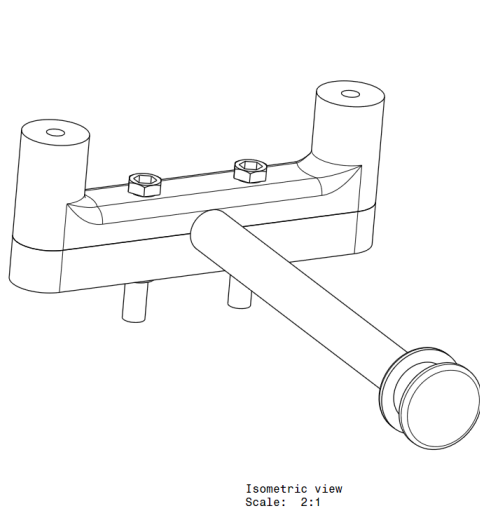


Figure 5.4: Assembly front suspension

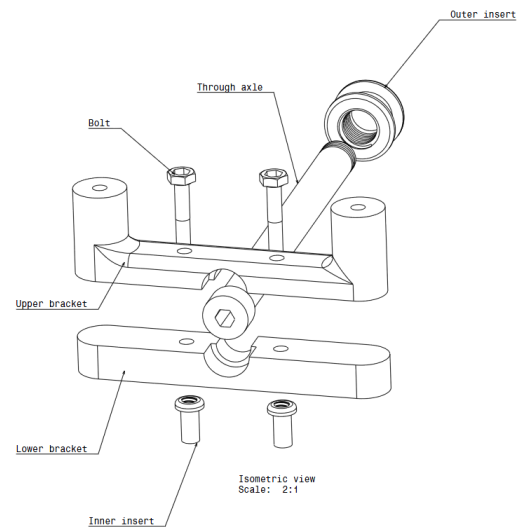


Figure 5.5: Exploded view of the front suspension

## 5.5 Detailed Design Rear Suspension

The difficulty of integrating the steering with the suspension is that all degrees of freedom need to be constrained, except for the yawing motion (rotating about the vertical axis). All the degrees of freedom can either be constrained by one or multiple components. Constraining all degrees of freedom with a single component might lead to obstruction of the yawing motion due to deformations of the component. In a meeting with the current Eco-Runner team, they mentioned this happened before. Using separate components for each degree of freedom will get rid of this problem. The mass difference is expected to be negligible between one or several components. Several components require more parts, but each part can be optimized for constraining its degree of freedom. This efficiency cannot be reached using one component. The higher reliability of the steering systems is the main criterion to choose to constrain the degrees of freedom with multiple components.

As for the front suspension, the loads can be either introduced into the body through one side or through two sides of the axle. For the same reason as for the front, it was also chosen to introduce the loads of the rear suspension on both sides. This choice eliminates the commonly used fork and kingpin concepts.

The vertical translation of the axle is constrained by two horizontal plates. Translations in the horizontal plane are constrained by a bracket on the axle and a rod placed under an angle attached to this bracket. Again, the wheel is supported on both sides by rods to increase lateral stiffness. The moments in the vertical plane are constrained by placing a second rod above the first one. The yawing moment is allowed by letting the axle roll on the two horizontal plates by means of a bearing. The normal load is introduced in two points below the rails on each side of the wheel. The lateral and longitudinal forces are introduced by two points to the body.

The wheel alignment is secured by spacers on the axles. For the wheel to make the smallest yaw rotation, the turning point needs to be above the contact point. This means that the center line of the rods needs to intersect above the contact point of the wheel. This is a requirement for the angle of the rods. The rods are placed higher in the body, as there is more space to make a larger angle. This was a trade-off of a higher bracket, but a more efficient load introduction in the body. The rod end can be screwed on the rod insert, making it adjustable for a perfect alignment.

For the materials, the same trade-off is done as for the front suspension. The bracket, inserts and rails are made out of aluminum. The axle is made out steel to meet the stiffness requirement. There is

one exception and those are the rods. Off-the-shelf carbon fiber rods can be bought that are lighter than aluminum rods. Moreover, the rods are not weakened by any holes if inserts are glued to each end. This reduces the design and production complexity of the rods.

As for the front suspension, the concept design was drawn, dimensioned and assembled in CATIA. The CAD drawings are shown in Figures 5.6 and 5.7. The bearings on the ends of the axle roll in the rails and are constrained on the ends to make sure the wheel will never touch the fairing during turning. The bearings are kept in place using a bolt. Next to the bearings, two brackets attach the four rods to the axle. On the right bracket, also the steering rod is attached. This steering rod goes to the bulkhead, where it is attached to the push-pull cable. The end of the steering rod is also attached to two springs, which bring the steering rod back to the equilibrium position after releasing the control handle. The axle itself is made hollow, so that the wires can go through it and come out in the middle of the axle, straight into the in-wheel motor.

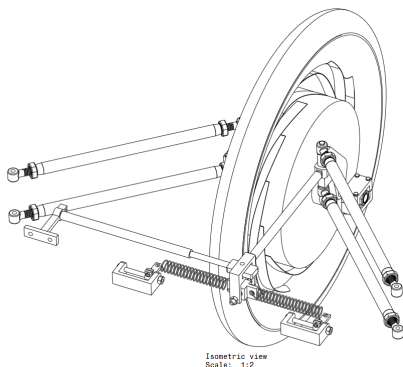


Figure 5.6: Assembly rear suspension including wheel

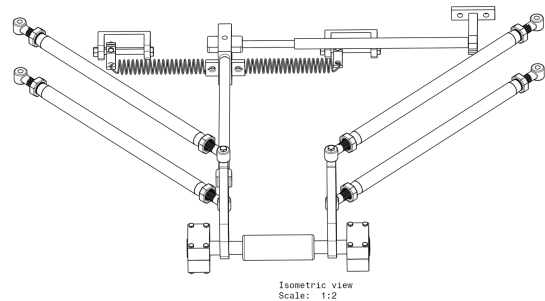


Figure 5.7: Assembly rear suspension

## 5.6 Verification and Compliance Matrix

The dimensional requirements are verified with an assembly in CATIA. All CAD models of the components are assembled together, including the driver. The axle fits through the hub of the wheel and the inserts are aligned with the monocoque. For the front suspension, the distance between the left and right inner bracket is not large enough to accommodate the driver. The removal of the wheel via the top is also checked in this assembly. The bracket height, rod length and angle of the rear suspension were modified in the assembly in order to fit the rear suspension in the body. A picture of the assembly is shown in Figure 5.8.

The design verification of the structural requirements is done by fundamental principles of mechanics of the materials. The verification process starts by isolating and simplifying the components in a free body diagram. For the calculations, the smallest cross-section is taken for the maximum point loads. The maximum load is described in the contingency section above. Though all the weight is on one wheel, it is assumed that the forces are distributed equally to the left and right side of the axle. The weight increase by over-designing the component is very small and outweighed by the simplicity of the verification calculations. The calculations are performed either to optimize the components dimension or to check whether the dimensions comply with the requirements.

The critical dynamic normal load introduces bending in the axle, shear stress in the bracket and tension stress from the insert to the composite body. To check whether the design can withstand this load, the bending of the axle should be within the deformation requirement, the bracket should not fail or deform under the shear stress and the composite should be able to carry the tensile load. The verification calculations for these three cases are shown below. These are both performed for the front and rear

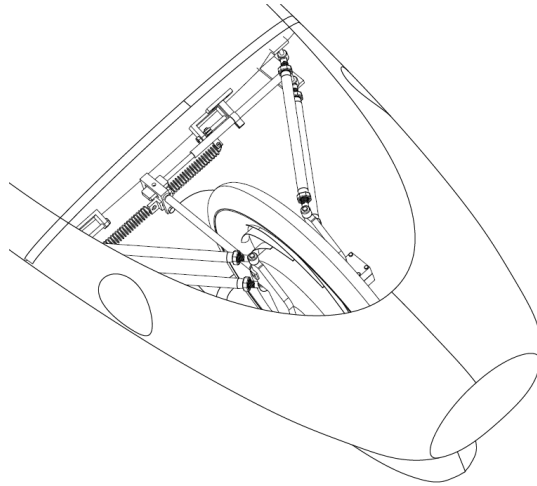


Figure 5.8: Isometric view of the assembly of the suspension

suspension.

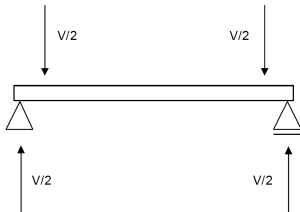


Figure 5.9: Free body diagram of the axle

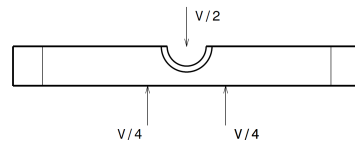


Figure 5.10: Free body diagram of the front lower bracket

The axle is assumed to be a simply supported beam with a couple of forces on each side as shown in Figure 5.9. In reality, the axle is clamped, reducing the maximum deformation even more; thus this calculation is on the safe side and reduces the complexity of the calculations. The axle diameter is determined by the bearings of the wheel. The shear force  $V$  is equal to the maximum dynamic load in the requirements. The maximum deflection  $w$  is in the middle of the beam and given by Equation 5.1 [21]. The deflection should be within  $0.1 \text{ mm}$  set by the requirements.

$$w = \frac{1}{8} \frac{Ml^2}{EI} \quad (5.1)$$

The force body diagram of the front suspension lower bracket is shown in Figure 5.10. The thickness  $t$  of the bracket is optimized for the maximum shear force  $V$ , shear stress  $\tau_{max}$  and width  $b$ . The maximum shear stress is determined by the shear modulus  $G$  of the material, the maximum allowed deformation  $\Delta x$  by the requirements and the initial length  $l$  of the bracket. The outcome is the minimum thickness the bracket needs to have everywhere. The maximum shear force is equal to the maximal dynamic load. Note that a rectangular cross-section of the bracket is assumed. The maximum shear stress is shown in Equation 5.1 [21] and the minimum thickness is presented in equation 5.3 [21].

$$\tau_{max} = \frac{G\Delta x}{l} \quad (5.2)$$

$$t = 1.5 \frac{V}{\tau_{max} b} \quad (5.3)$$

For the inserts the maximum out of plane force is calculated, as this is the critical load for composites. The maximum forces the inserts have to be able to withstand are calculated by multiplying the outer area with the shear strength of the core. It is assumed that the core is the weakest part. The glue is assumed to be stronger. The maximum force for a round insert can then be computed with Equation 5.4 and should be lower than 250 N.

$$F = 2\pi \cdot r \cdot h \cdot \tau_{max} \quad (5.4)$$

Similar verification calculations are performed for the lateral forces, braking forces and deformations. Several iterations took place to optimize the design for the loads with aid of these verification calculations. In the compliance matrix presented in Table 5.4, the results of the verification process are shown. All but one requirement are met.

Table 5.4: Suspension compliance matrix

Requirement	Compliance	Verification method
Su.D.1.F.	x	CATIA assembly
Su.D.1.R.	✓	CATIA assembly
Su.S.1.F.	✓	Mechanics of materials
Su.S.1.R.	✓	Mechanics of materials
Su.S.2.	✓	Mechanics of materials
Su.S.3.	✓	Mechanics of materials
Su.S.4.	✓	Mechanics of materials
Su.S.5.	✓	CATIA assembly

Su.D.1.F. was not met as the driver modeled in CATIA did not fit between the front suspension. The dimensions of the driver were based on the dimensions of an average person using online database DINED. However, the driver selected is usually smaller than an average person. The distance between the front suspension was compared to that of the Eco-Runner 3 and was found out to be 1 cm larger. So it means that the current driver would fit between the front suspension. This confusion could have been prevented by adding a width value to the dimensional requirement.

## 5.7 Production Plan

The brackets, axles and inserts are produced by the team itself. The team has free access to milling, turning and CNC machines. The tolerances of the machines range from 0.1 to 0.01 mm. The bearings, carbon fiber rods and bolts are off-the-shelf products. The inserts are glued onto the body and the carbon fiber rods. To compensate for production errors or tolerances, the rods are made adjustable.

## 5.8 Validation Plan

The dimensions can be validated by putting a mock-up of the suspension inside the body. The mock-up can be of a different material that is cheap and easy to form as long as the dimensions are correct. For example foam or printed material can be used. The mock-up does not need to withstand the loads, it is just to check if the design fits in the body.

The structural requirements can be validated by performing tests on the bracket, axle, rods and inserts. This means that extra components need to be produced for the tests.

For the inserts, an ASTM pull through test and an in-plane shear test can be performed to check whether the inserts and composite body can withstand the required loads. A three point bending test can be performed to validate the stiffness of the axle. A compression and pull test can be done for the rods of the rear suspension. And an ASTM B769 test can be performed to validate the shear strength of the

brackets.

When the car is finished, track tests can be performed to validate the values of the load requirements. Strain gauges or accelerometers can be attached to the wheel, axle, bracket or rods to measure the displacement or acceleration. From these parameters, the loads can be computed. The loads can be compared to the loads in the requirements and validated whether the vehicle is over- or under-designed.

## 5.9 Mass and Cost

For the suspension, CATIA drawings were made. In CATIA, it is possible to assign a material to the parts and receive the mass. Costs for the materials are used as a function of mass. These prices are found in Tables 5.5 and 5.6 [3] [22]. From the material trade-off, it was decided to use Aluminum 7075 heat treated and stainless steel alloy 17-7PH. In the cost breakdown, the material mass is multiplied by two to include the waste created by milling and turning the part from a solid block. This factor two was based on a simple approximation using Figure 5.11. In Figure 5.11, it is observed that the area that will be milled away is approximately 50% of the block. Afterwards, the mass and costs are summed in Table 5.7, 5.8 and 5.9, 5.10, 5.11 for the front and rear suspension respectively.

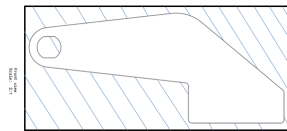


Figure 5.11: Waste factor of manufactured parts

Table 5.5: Material costs for aluminum 7075 and stainless steel alloy 17-7PH

Material	Price [\$/kg]	Price [€/kg]
Steel	8.43	6.28
Aluminum	9.35	6.97

Table 5.6: Material cost for the off-the-shelf carbon fiber rod

Material	Cost [€]
Carbon fiber rod - hollow: 15mm d, l = 1.5m	70

Table 5.7: Mass breakdown for the total front suspension

Part	Material	Count	Mass [g]	Total mass [g]
Axle	steel	2	75	150
Upper bracket	aluminum	2	42	84
Lower bracket	aluminum	2	34	68
Insert fairing	aluminum	2	4	8
Insert inside	aluminum	4	2	8
M3 bolts	steel	4	3	12
Total				330

Table 5.8: Cost breakdown for the front suspension

Material	Total mass [g]	Waste included [g]	Cost [€]
Aluminum	180	360	3.37
Steel	162	324	2.73
Total			6.10

Table 5.9: Mass breakdown rear suspension

Part	Subpart	Material	Subpart count	Subpart mass [g]	Subpart total mass [g]	Part count	Part mass [g]	Part total mass [g]
Rod						4	67	268
	Carbon rod	Carbon	1	17	17			
	Rod end	Aluminum	2	10	20			
	Nut	Steel	2	11	22			
	Insert	Aluminum	2	4	8			
Axle		Steel				1	384	384
Bearing		Aluminum				2	8	16
Rail		Aluminum				2	154	308
Bolt		Steel				16	2	32
Nut		Steel				10	1	10
Bracket		Aluminum				2	156	312
Ring		Aluminum				4	1	4
Steering rod						1	197	197
	Carbon rod	Carbon	1	21	21			
	Rod end	Aluminum	2	88	176			
Pushpull attachment		Aluminum				1	62	62
Spring attachment		Aluminum				1	22	22
Spring		Aluminum				2	3	6
Total								1621

Table 5.10: Cost breakdown for the rear suspension for aluminum and steel

Material	total mass [g]	Waste included [g]	Cost [€]
Aluminum	934	1868	13.03
Steel	64	128	0.80
Total			118.84

Table 5.11: Cost breakdown for the rear suspension for the carbon fiber rods

Material	Cost	Waste included	Cost [€]
Carbon	70	105	105

It is assumed that the only costs for the team are material costs. The manufacturing will be done by team members since the parts are not really complex. The machines are available in the D:Dreamhall for free and are accurate enough for these parts. A mass reduction of 70% is achieved for the front suspension and 5% for the rear suspension based on the documentation provided by the current Eco-Runner team.

## 5.10 Risk Analysis

When considering all risks, the failure of the two functions are the main ones. This includes blocking of the steering system and failing of the suspension under the loads introduced. These risks are mapped into a technical risk map, found in Section 2.5.

For the blocking of the steering system, already all degrees of freedom are constrained with different structural elements. This is done to prevent the failure of the entire steering system due to failure or blocking of only one degree of freedom.

For the introduction of the loads, the suspension is designed for the worst case scenario. To be able to introduce the loads as calculated, the production and alignment are important. The attachment to the body is also really important to be able to transfer the loads. If this is not done correctly, delamination of the body at the insert could occur.

Finally dragging of brakes is a major risk. This year, this was the main issue during the race. The body and suspension were not stiff enough, so in corners the alignment of the brakes changed and led to dragging. Obviously this is fatal for the efficiency. To prevent the dragging, the body and the suspension are made stiffer.

## 5.11 Recommendations

In Appendix B, a model is described to analyze the dynamic loads on the wheels and suspension. In this model no damping is included, since it was already decided that no damping would be used in the design. If next year the damping is included in the model, the effect of damping on the loads introduced to the body can be analyzed. Damping might reduce the peak forces introduced to the body and level out the loads. A choice of damping or not damping the vehicle could then be based on this model.

In this detailed design, the braking system is not further worked out. It was already decided that both front as rear disc brakes would be used. In the design of the suspension, it is defined where the claw will be attached since here the loads will be introduced. It would be useful to work out the integrated disc claw mount, disc and claw also in detail. The attachment and dimensions itself can be adapted.

The brackets are verified for the separate loads. This was done as the dynamic normal load is by far the largest force and there was no time in the end to perform a Von Mises stress calculation. In a further stage, the Von Mises [21] yielding criterion can be used for a higher accuracy.



# 6 Wheels

A disc wheel has been designed and used in the Eco-Runner for the last two years. There is a lot of data and experience for designing and producing the disc wheel, therefore it can be considered as a proven concept with little risk. Although spoke wheels have not been used in the Eco-Runner vehicle, it is widely used in other vehicles participating in the Shell Eco-marathon and many other vehicles. Data needed for the design can be found in literature. Hence, spoke wheels have slightly more design risk than the disc wheel, but is still a mature concept. The hubless wheel is a new concept for the Eco-Runner. No vehicle has used this concept so far in the Shell Eco-marathon. Even in the field of automobile, it is an immature innovation and rarely used. Little data can be found for the design of a hubless wheel. Hence, it has a high design risk.

According to the trade-off done in the conceptual design phase [13], the spoke wheel concept has the best performance. The lower mass, material cost and production complexity give it a slight advantage over the disc wheel. The uncertainty, risk and complexity of the design are the downside of the hubless wheel, though in theory it has high potential for a light and aerodynamic design.

The chosen design concept for the wheel is a Michelin 44-406 tubeless tire fitted on a spoke wheel. The wheel has an out diameter of 500 mm, with an inflation pressure of 6 bar. The rolling friction coefficient on dry asphalt is equal to 0.0024 [-] and a first mass estimation for the spoke and rim is equal to 601 gr. For the detailed design it is recommended that the spoke wheel concept is further optimized regarding the number of spokes, the spoke pattern, the spoke and rim material and integration with the in-wheel motor. The design process that is used in the detailed design phase to optimize the wheels is shown in the work flow chart shown in Figure 6.1.

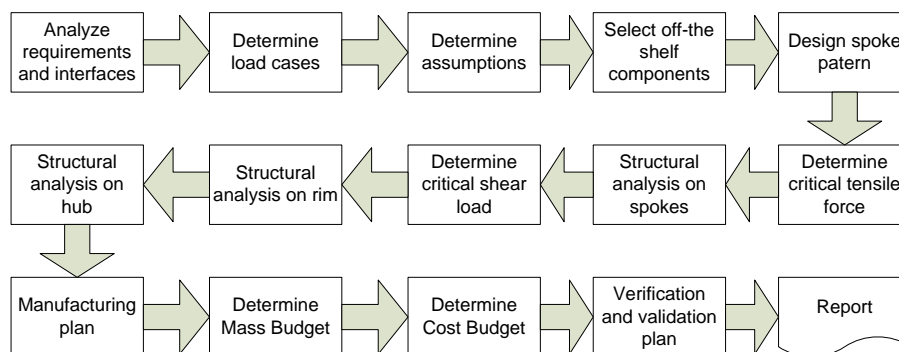


Figure 6.1: The design process of the wheels

## 6.1 Functions and Requirements

The function of the wheels is to provide an efficient movement of the vehicle across the track. In order to do this, the wheels have to transfer and withstand loads. The functions of the wheels are specified as:

- Support vertical load, while cushioning against road shocks;
- Withstand longitudinal forces for acceleration and braking;
- Withstand lateral forces for cornering.

These functions yield certain requirements for the wheels. As reported in the mid-term report [13], these requirements are given in the Table 6.1.

Table 6.1: Table of requirements for the wheels

Category	ID#:	Requirement:
Drag	W.D.1	Have a maximum rolling friction coefficient of 0.0027 [-] on an asphalt surface in dry conditions.
Strength	W.D.2	Have a maximum bearing friction coefficient of 0.001 [-].
	W.STG.1	Support a maximum vertical load of 916 N.
	W.STG.2	Withstand a lateral cornering force of 258N .
	W.STG.3	Withstand a longitudinal acceleration force of 27.8 N.
Stiffness	W.STG.4	Withstand the longitudinal braking force required to hold the vehicle immobile when placed on a 20° incline.
	W.STF.1	Have a maximum radial deflection of 0.04% of its original length.
	W.STF.2	Have a maximum lateral deflection of 0.04% of its original length.

## 6.2 Load Cases

Before starting with the preliminary design of the wheel, it is important to look at the load cases for which the wheel should be sized. These load cases are derived from the requirements stated in the mid-term report [13] as well as from calculations done in Chapter 5. The values are such that they represent the worst case scenarios for braking and cornering per wheel as well as the pressure on the rim from the tire inflation. All forces and their corresponding magnitudes are summarized in Table 6.2. The directions in which the forces act are indicated in Figure 6.2 and Figure 6.3.

Table 6.2: Load cases for the wheels

Type of Force	Load	Explanation of Value
Cornering torque	65 Nm	This value is derived from the steady-state cornering model described in the mid-term report [13]. The cornering torque is caused by the lateral cornering force.
Braking torque	96 Nm	The braking torque is caused by the longitudinal braking force. The braking force is derived from the competition requirements for braking on a slope of 20%.
Radial (front wheel)	2132 N	These forces are calculated using a mass-spring system to represent the vehicle. A worst case scenario is considered when the car hits a bump of 15 mm height with velocity of 7.5 m/s.
Radial (rear wheel)	1209 N	
Inflation pressure	1.75 MPa	The maximum pressure force which the rim should be able to withstand is 0.7 MPa. It acts as a distributed load along the inner profile of the rim. A safety factor of 2.5 is used for the value of the pressure force.

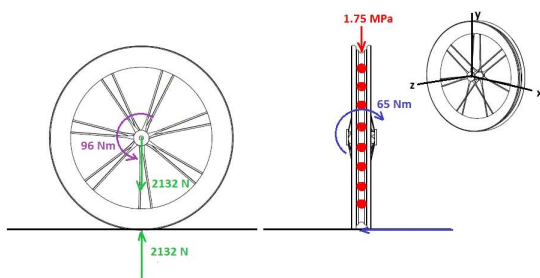


Figure 6.2: Front wheel load case

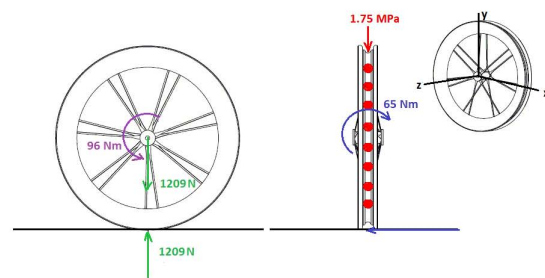


Figure 6.3: Rear wheel load case

## 6.2.1 Assumptions

Before performing a structural analysis on the wheels two important assumptions are made to simplify the situation:

1. The spokes of the wheels take only tension loads;
2. The rim only take shear stresses and bending loads;
3. The rim profile is a semicircular shape, and the loads from the tire are perfectly transferred into the rim. This assumption is valid since the rim profile is actually stiffer than a semicircular shape, due to the stiffening effect of the corners in the profile [23].

## 6.3 Tires

The main criterion in selecting a tire is that it should be an off-the-shelf product with a rim diameter between 0.33 m and 0.43 m [9]. Due to limited resources the design and production of the tires is outside the scope of this project. Another criterion for the tire is that it should be compatible with the tubeless use of the tire. Tubeless tires have the advantage over tubed tires that no energy is lost by the friction between the tire and the tube. There are two such tires especially designed for the Shell Eco-marathon prototype class by Michelin. These two types of tires will be discussed in this section and a selection will be made.

### 6.3.1 Tire Selection

The Michelin 44-406 tire and the Michelin 45-75R16 tire are especially designed for the fuel efficient vehicles competing in the Shell Eco-marathon. The specified characters, according to Michelin [10], of the tires are displayed in Table 6.3. Both these tires are compatible for tubeless use and an inflation pressure of 5 bar to 7 bar can be applied. Thus these are both suitable candidates. Trade-off criteria between the 44-406 and the 45-75R16 tires will be based on the main differences between the two tires: the weight of the tires, the rolling friction coefficient,  $C_r$  and the shape of the rims. The cost difference of the two tires will not be taken into account in the trade-off since the cost both these tires are within the budget of the Eco-Runner 3.

Table 6.3: The specified characters of the Michelin 44-406 and 45-75R16 tires.

Michelin Tire number:	44-406	45-75R16
Type	Flexible wire-bead tire	Tubeless radial ply tire
Tube	Tubeless mounting possible	Tubeless mounting possible
Ply	Radial ply	Radial ply
Seat diameter	405.6 mm	405.6 mm
Outside diameter	500 mm	478 mm
Section width	44 mm	45 mm
Rim type	Crochet	Standard Motorcycle Rim
Rim sizes	19, 21, 23 or 25 mm	30.5 or 34.0 mm
Maximum inflation pressure	7 bar	7 bar
Rolling drag coefficient $C_r$ at 40 km/h	0.0024 [-] at 5 bar	0.00084 [-] at 5 bar 0.00081 [-] at 6 bar
Cornering stiffness $C_\alpha$	22000 [-]	13751 [-]
Mass	150 g	400 g
Loading capacity	100 kg	100 kg
Cost	\$140.00	\$335.00

The mass of the tires varies greatly. The 44-406 is 150 g versus the 45-75R16 of 400 g. The absolute mass difference is 250 g, which is very large. More important is to compare this mass saving with the

mass of the total vehicle. Assuming a total vehicle mass including driver of  $80 \text{ kg}$ , then the mass saving of  $250 \text{ g}$  per tire for three tires in total, is  $0.94\%$ . The mass saving of  $0.94\%$  should be compared with the difference in rolling drag coefficient  $C_r$ .

The  $C_r$  at  $5 \text{ bar}$  for the 44-406 tire is 2.8 times higher than the  $C_r$  of the 45-75R16 tire. The effect of the  $C_r$  on the friction drag of the vehicle is much higher than the mass difference. To be able to compare the mass difference with the difference in  $C_r$  of the two tires, the rolling friction drag force,  $F_r$  is calculated for each tire, by using the relation given in Equation 6.1.

$$F_r = m \cdot g \cdot C_r \quad (6.1)$$

A total vehicle mass including driver,  $m$ , of  $80 \text{ kg}$  is taken as a reference and the gravitational acceleration,  $g$ , is  $9.81 \text{ m/s}^2$ . As can be seen in Table 6.4, the total rolling drag of the 44-406 turns out to be almost three times higher than the 45-75C16 tires. Clearly, the value of the  $C_r$  of the tires is dominant over the mass of tires. Therefore, the Michelin 45-75C16 tire is selected.

Table 6.4: The effect of the rolling friction coefficient and the mass of the 44-406 and 45-75R16 tire.

Michelin tire type	Tire mass	Total vehicle mass	$C_r$ at $5 \text{ bar}$	Total rolling drag $F_{r,f}$
44-406	$150 \text{ g}$	$79.25 \text{ kg}$	$0.0024 [-]$	$1.87 \text{ N}$
45-75R16	$400 \text{ g}$	$80.00 \text{ kg}$	$0.00084 [-]$	$0.66 \text{ N}$

### Rim profile

For the same tire profile, different rim profile sizes can be selected. There are two options for an inner rim width:  $30.5 \text{ mm}$  or  $34.0 \text{ mm}$  [24]. Again, the same trade-off criteria can be used: weight and rolling drag. In the picture below, the inner rim profile 45-75C16 is displayed. The widest rim profile of  $34.0 \text{ mm}$  is selected. Firstly, because a wider profile will result in a wider tire contact patch. A shorter and wider contact patch will eventually result in a lower rolling resistance. The difference in tire contact patches for a wide and narrow tire and the effect on rolling resistance is clarified in Figure 6.5. This effect was found in a study on cycling tires [25]. The second advantage of the wider rim is that the cross-sectional area of the rim increases and therefore, the moment of inertia of the rim profile, which increases its resistance to torsion. On the contrary, for the smaller rim less material will be used, hence the wheel becomes lighter. Since the rim is just a part of the wheel an extra  $3.4 \text{ mm}$  for the rim width will add a negligible amount of extra weight, as it will be produced of carbon fiber composite material which has a very low density of about  $1500 - 1700 \text{ kg/m}^3$ .

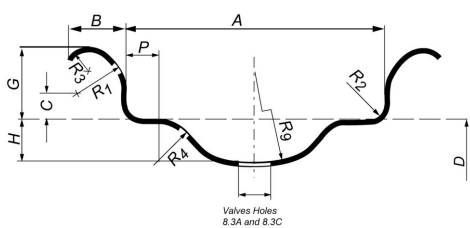


Figure 6.4: The rim profile for the 45-75R16 tire [24].

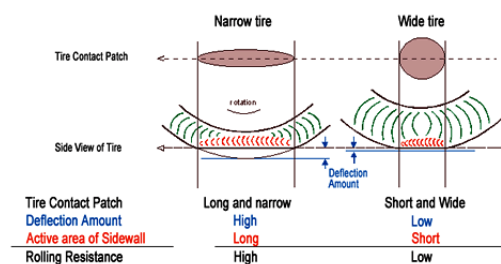


Figure 6.5: Rolling resistance of tire size [25].

## 6.4 Spokes

The spokes are the most highly stressed components of the wheel and they require special attention during the design and assembly, otherwise the wheel will not be reliable. During the design of the spokes

several main decisions have to be made: number of spokes and spoke pattern, thickness of the spokes and orientation of the fibers in the different layers. The larger the spoke cross-section and number of spokes are, the stronger the wheel will be.

### 6.4.1 Front Wheel Spoke Pattern

Spokes can be laced in a variety of patterns in order to improve their performance in terms of strength, stiffness and durability. Spoke patterns are described by the number of times a spoke crosses other spokes. It is possible to have anything from no crossing (most commonly referred to as radial spoking) up to three to four crossing spokes. Through a Finite Element Method the effect of different spoke patterns is analyzed on radial stiffness [26]. It is found that a radially spoked wheel is about 4.6% stiffer than a tangentially spoked one. For a radially spoked wheel with 32 spokes, the vertical deflection at the middle of the contact patch is 0.1688 mm.

Another advantage of radial lacing is the fact that a slight weight reduction can be achieved since the spoke length is shorter compared to that of crossing spokes. Last, but not least, *The Bicycle Wheel* [27] concludes that the most efficient power transfer occurs when the spoke leaves the hub at a 90 ° angle which is the case for the radial spoke wheel. The main disadvantage of this configuration is that it does not resist torque very well. For example, if the driving wheel is to be radially spoked, the torque from the electric motor could cause the spokes to bend. In this sense, the rear wheel must have a certain spoke crossing configuration in order to increase its resistance against the motor torque. For any further analysis of the wheel, the spoke patterns that will be used are summarized in Table 6.5.

Table 6.5: The pattern of the spokes per wheel

Front wheel	Rear wheel
No crossing, radial	Crossing, 2 or 3

### 6.4.2 Spoke Count and Cross-Section of the Front Wheel

The spoke count is an important design parameter which dictates the load resisting capabilities of the structure. The smaller the number of spokes, the higher the spoke stress, since fewer spokes are available to carry the same dynamic load and the redundancy reduces. In order to determine a suitable spoke count, a simple analysis of the load distribution through the spokes is performed. Several simplifying assumptions are made, and are summarized in Table 6.6 and are divided according to their level of importance.

In order to be able to solve the problem quickly, the first and second primary assumptions play an important role. In dealing with a rotating object, the analysis is greatly simplified by assuming that the object is rigid. The approximation that the hub hangs from the spokes is also critical. Without this assumption, the analysis would be rather complicated since the problem is a statically indeterminate one. In the work of Jinny Ng [28] the Von Mises stress distributions of a spoked wheel subjected to a radial load are found. As it can be seen from the stress plot in Figure 6.6, the most critical stresses are experienced at the upper region of the wheel which means that the assumption that the hub hangs from the upper spokes is valid.

Now that the assumptions and their implications are known, it is important to perform the necessary calculations to determine the spoke tension and decide on a number of spokes. Looking at reference bike wheels with carbon fiber spokes, the number of spokes varies from 3 to 10 per wheel side. A preliminary value of 7 is used to calculate the tensile forces. This value is picked with a fail safe consideration in mind. If one of the spokes fails during the race, the wheel must continue to perform its function. For a configuration with 7 spokes, the angle  $\theta$  between two consecutive spokes is 51.5 °. For comparison of tensile forces, two scenarios will be investigated. The first one is the case in which three spokes are

Table 6.6: The assumptions and corresponding implications

Type	Assumptions	Implications
Primary	<ol style="list-style-type: none"> <li>1. The rim is assumed to be rigid</li> <li>2. The hub hangs from upper spokes</li> </ol>	<p>This introduces error since all objects are deformable to some extent.</p> <p>This leads to greater tensile forces in the upper spokes since some of the lower spokes are still in tension and participating in the load transfer but are not considered in the calculations.</p>
Secondary	<ol style="list-style-type: none"> <li>1. The loading is applied in plane through the hub axle and causes no hub deformation</li> <li>2. Small angle approximation</li> </ol>	<p>In reality, the hub is going to be displaced from its initial location and will deform due to the load application; this leads to a difference in the experienced tensile forces.</p> <p>The wheels are cambered and so the actual load in the wheels is the result of the external load multiplied by the inverse of the cosine; this means that the load in the wheel will be slightly larger than the external forces.</p>

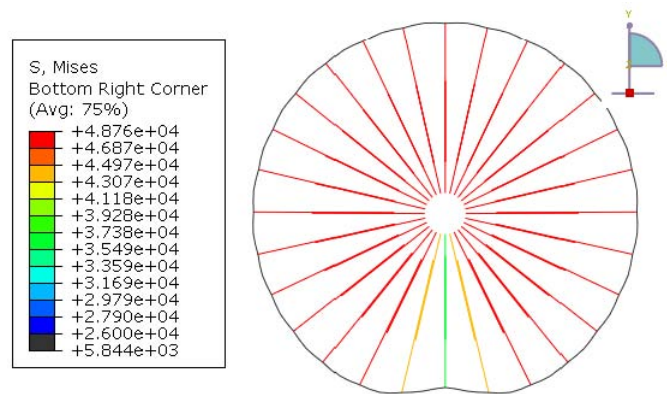


Figure 6.6: Stress plots of spokes

located in the upper half wheel with orientation shown on the left of Figure 6.7. The second case is for four spokes in the upper half wheel with orientation shown on the right of Figure 6.7. The corresponding force equilibrium equations for both cases are summarized in Table 6.7. The inputs for case I and case II are the same and are shown in the left column of Table 6.8 and Table 6.9. The right columns show the corresponding outputs.

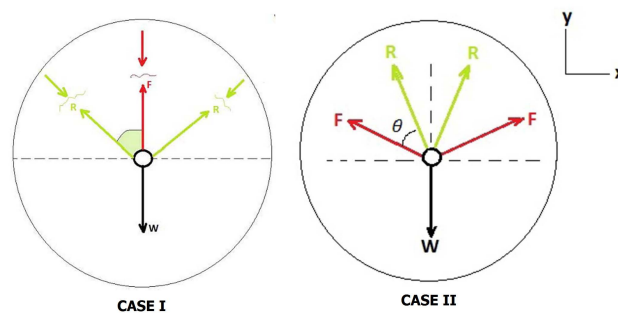


Figure 6.7: Free body diagrams of case I and II

Table 6.7: Force equilibrium equations for case I and case II

Case	Set of equations
I	$\sum F_y = 0 = F + 2R \cos \theta - W$ $R = F \cos \theta$
II	$\sum F_y = 0 = 2R \cos(\theta/2) + 2F \cos(3\theta/2) - W$ $R = \frac{F \cos(\theta/2)}{\cos(3\theta/2)}$

Table 6.8: Inputs and outputs of case I and case II for the front wheel

Inputs		Outputs case I		Outputs case II	
W	2132 N	F	1201 N	F	273 N
$\theta$	51.5°	R	748 N	R	1117 N

Table 6.9: Inputs and outputs of case I and case II for the rear wheel.

Inputs		Outputs case I		Outputs case II	
W	1209 N	F	681 N	F	155 N
$\theta$	51.5°	R	424 N	R	633 N

The most critical tensile force is calculated to be 1201 N. Knowing this tensile force and assuming a cross-sectional shape with certain dimensions, the direct stresses in the spokes can be calculated and compared to the tensile strength of carbon fiber to check whether or not the spokes will fail. In this case, the selected cross-section is not circular, but rectangular. The main structural and manufacturing advantages are summarized below.

Manufacturing advantages:

- The spokes can be produced simply by prepreg lay-up of a laminate and then curing;
- No nipples are required for attachment of the spokes to the rim and hub; the spokes can just be twisted around the hub and glued.

Structural advantages:

- The flat design provides a large bond area; if a good adhesive is used, this can increase the load capacity significantly.
- The spokes are flexible which means that in case of a large compressive load, they will twist or bend and then return back to their original shape, much similar to a spring.

Now that the cross-sectional shape is known, it is important to set up the ply count and the orientation of the fibers. The spokes are primarily loaded in tension, which means that unidirectional plies with 100% 0°-orientation must be used. The material that will be used is *HexTow<sup>TM</sup>* IM 6 carbon fiber with fiber volume content of 60% for which the ultimate tensile strength is 1.5 GPa. *HexTow<sup>TM</sup>* IM6 fiber is a continuous, high performance fiber which has low density, high modulus and good shear strength. Using the definition of stress and knowing that the maximum tensile load in the spokes is about 1200 N, the minimal cross section required to take these loads is about 0.8 mm<sup>2</sup>. Each layer of IM 6 has a thickness of 0.125 mm.

The final cross section dimensions of the spoke as well as the specifications of the material used are indicated in Table 6.10. Two plies of unidirectional fibers are needed and two extra plies for are used, to

make handling of the spokes easier during the manufacturing process, yielding a thickness of  $0.5\text{ mm}$ . The corresponding width of the spoke is  $5\text{ mm}$ .

Table 6.10: Front wheel spoke characteristics

Material	Type of material	Ply thickness	No. of plies	Spoke thickness	Spoke width
IM 6 carbon fiber	Laminate	$0.125\text{mm}$	4	$0.5\text{mm}$	$5\text{mm}$

### 6.4.3 Rear Wheel Spoke Pattern

The rear wheel spoke pattern of the Eco-Runner has to be designed separately from the front wheel pattern. The reason for this is the presence of the hub with its in-wheel motor. The hub of the motor has a diameter of  $220\text{mm}$  which is almost half of the diameter of the wheel. This means that the spokes have to be twice as short. Having straight  $120 - 130\text{mm}$  spokes connecting the rim to the hub might not be the most optimal design choice in terms of structural performance and manufacturing. It is important to note that the rear wheel will be subjected to torque during braking as well as torque from the in wheel motor which means that the spoke pattern has to be adjusted accordingly. Three different concepts for the rear wheel are considered. They are modeled in CATIA v5 in order to obtain the most accurate weight estimation and a better understanding of how the design will look when manufactured. The three concepts are described in the Table 6.11.

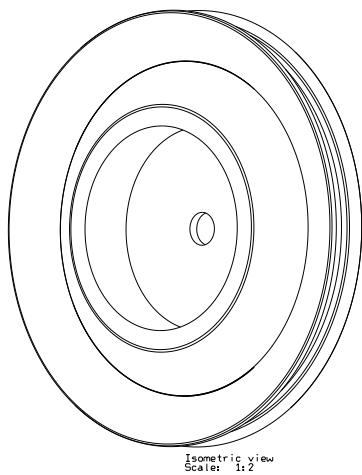


Figure 6.8: Closed cross-section concept

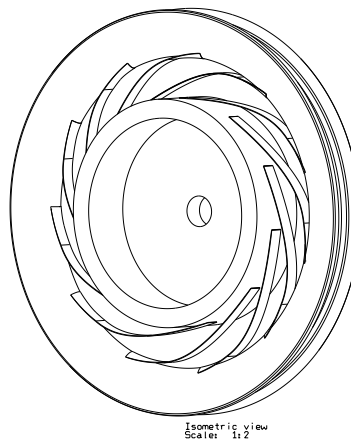


Figure 6.9: Turbine blade concept

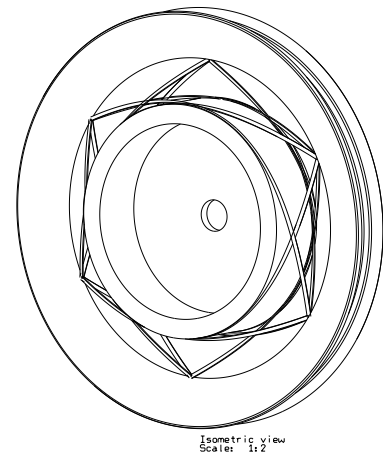


Figure 6.10: Continuous spokes concept

Table 6.13: The characteristics of the three rear spoke patterns.

Concept	Carbon fiber type	Ply count	Fiber orientation	Mass [kg]
Closed cross section	<i>HexTow</i> <sup>TM</sup> IM6	3	$+45^\circ/0^\circ/-45^\circ$	0.080
Turbine blade	<i>HexTow</i> <sup>TM</sup> IM6	5	UD $0^\circ$	0.060
Continuous spokes	<i>HexTow</i> <sup>TM</sup> IM6	6	2 outer :12K carbon weave 4 innermost layers: UD $0^\circ$	0.055

Based on these concepts a trade-off is performed. The criteria and the corresponding weighing factors are shown in Table 6.12. Manufacturability refers to the ease of production of a certain part and has the highest weighing factor, because the Eco-Runner team has limited financial resources

Table 6.11: Thee rear wheel concepts.

Concept	Description
Closed cross-section (Figure 6.8)	The closed cross section concept is essentially a disc wheel. This concept makes use of a carbon fiber casing to connect the rim to the hub. This creates a closed cross section which provides increased resistance in terms of torsion. The carbon fiber casing on both sides of the rim has to be produced using a mold. When the wheel is assembled, the rim and casing are glued together. The casing is then fixed to the hub using adhesive and is cured.
Turbine blade spokes (Figure 6.9)	The turbine blade concept consists of 13 spokes which are tangential to both the hub as well as the rim. The spoke width is 16 mm. The structural advantage of this concept is that the spokes are oriented in direction opposite to that of the braking torque. If a torque is applied in opposite direction to the orientation of the blades, they will be subjected to compressive forces. The spokes are solid and they are designed such that they pick up loads in tension and in compression. In terms of manufacturing, only one spoke mold is needed since all of the spokes have the same shape and cross-section. After the spokes are produced, they are glued to the rim and hub using adhesive. Large bonding areas must be ensured so that no peeling occurs.
Continuous spokes (Figure 6.10)	The idea of this concept is to have 12 continuous spokes going from the top of the rim to the bottom of the rim. These spokes are firmly bonded to the hub in order to provide stiffness against torsion. They do not cross, but rather go around each other. At the hub they are bonded next to each other. Just as the turbine blade concept, large areas for bonding are required, especially at the hub where peeling might occur due to different directions of forces in the spokes and the hub.

and has to be able to produce most of the components on its own. In this sense, the continuous spokes concept has the lowest score since the arrangement of the spokes in the indicated pattern will be tedious to make and has high risks at manufacturing. If the spokes are not positioned and glued correctly, the chance of failure is high. Furthermore, the fact that there are three attachment points per spoke, two at the rim and one at the hub, further increases the possibility of manufacturing error.

In this trade-off, feasibility is related to the risk associated with a novel design concept. Both the turbine blade and the continuous spoke designs are considered as novel concepts. The fact that there is no previous related research on these two spoke patterns introduces a degree of uncertainty and risks. This degree of uncertainty can lead to a bottleneck when it comes to assessing the structural integrity of the spokes, which can further set back the optimization process. Furthermore, the spoke patterns have irregular shapes such that the resulting stresses cannot be estimated easily without a FEM tool. Feasibility is given the second highest weighing factor because even though the designs might be viable and producible, they might require too much time to optimize and guarantee the required structural performance.

Structural Performance is given the third highest weighing factor. Structurally, the wheels are not highly critical and in the case of the Eco-Runner vehicle, resources are limited, so the concepts have to be first assessed on whether or not they can be produced with the given tooling (Manufacturability) and within the given time constraint (Feasibility). In the scope of the preliminary design, structural performance relates to the ability of the design to sustain the given loads without failure. The closed cross-section concept is given the highest score since the design is very similar to that of a disc wheel which has been used by the team for the past three years. The structural concept behind the turbine blade spokes is that their curved shape is tangential to both the hub and the rim. This facilitates an easier load transfer and thus, lower stresses at the end points of the spoke. A drawback of this design is the radial loading capability. The continuous spokes are given the lowest score because their curved nature

Table 6.12: The trade-off summary of three rear wheel spoke patterns.

Criterion \ Option	Manufacturability	Feasibility	Structural Performance	Weight	Cost	Total
Weight factor [%]	30	25	20	15	10	100
Closed Cross Section	4	4	4	2	3	72
Turbine Blade	4	2	3	5	5	71
Continuous spokes	2	2	2	5	5	55

and three attachment points introduce additional forces, which might cause peeling.

Weight is given a significantly lower weighing factor if compared to the other criteria because the entire wheel is made of carbon fiber and the small achievable weight savings become less significant with respect to the total vehicle mass. Table 6.13 shows some preliminary mass estimation of the spokes and the disc.

Cost is assigned the lowest weight factor because the team is usually supplied with the needed materials such as carbon fiber or special molds. The lowest score goes to the closed cross section concept because it requires large molds which have to be specially produced. In case of the turbine blade and continuous spokes concepts, the cost decreases because less material is used. Furthermore, the use of a mold for the turbine blade concept does not increase costs since the mold is small and the relatively simple shape allows production within the team. No special assembly tool is needed for the turbine blade concept.

The results of the trade-off show that the closed cross-section concept and the turbine blade spoke pattern have almost the same score. Feasibility is the one real issue of the blade design option. Since it is an innovative concept which can lead to a significant weight reduction with respect to an optimized disc wheel, it is recommended as the option to be further developed. To show that the design has a potential, a rough analysis of a single spoke has been performed. The spoke is rigidly supported at the top in the curved region where the adhesive bond to the rim is located. The other end of the spoke is free to move and a tensile load of 200 N is applied there. The corresponding displacement and the maximum Von Mises stresses are shown in Figure 6.11 and Figure 6.12. The material, ply count and orientation used for the spoke are the same as the ones indicated in Table 6.13.

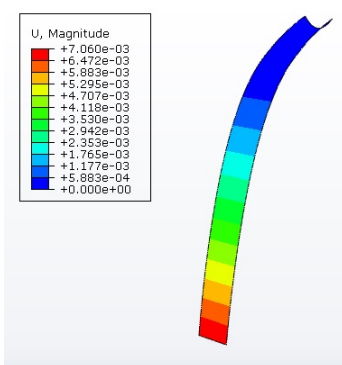


Figure 6.11: Deflection of a blade spoke

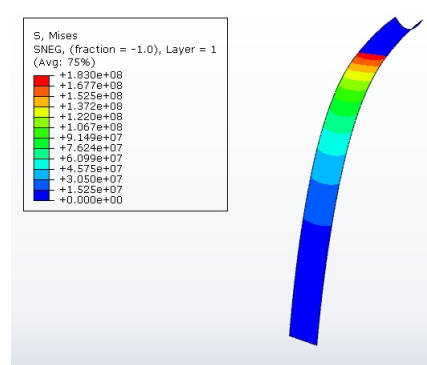


Figure 6.12: Von Mises stresses in a blade spoke

As expected, the deflection is largest at the free end and has a magnitude of 7 mm. The maximum Von Mises stresses are 183 MPa, 8 times below the tensile strength of HexTow™ IM6 carbon fibre. This analysis shows the potential of the turbine blade spoke pattern: the spoke does not fail under the

applied load and it displays a deflection of 4 % its length. The next step in the study of this concept is to superimpose all the loads that the blade is subjected to and perform a complete FEM analysis. Using the stress and deflection results, the material properties, ply count and fiber orientation of the spokes can be varied until an optimized solution is found.

## 6.5 Rims

By means of structural analysis, the thickness of the rim can be determined such that it can carry all the loads. Since the rims will be produced by the TU Delft Eco-Runner team using carbon fiber lay-up, the required thickness of the rim will determine the number of layers of carbon fiber fabric as well as the direction of the fibers needed to withstand all the loads. Because the total production will be done by hand, manufacturing errors can easily occur. Some errors in manufacturing might have catastrophic consequences and are not very unlikely to occur. One of the main errors in producing the rim in carbon fiber is the misalignment of the fibers. A misalignment of  $5^\circ$  for a unidirectional (UD) material could lead to a loss in strength and stiffness up to 20% [29]. Another probable error is that the resin is not very well spread between the fiber, causing dry and weak spots, where the loads are not properly transferred between the fibers. The structural analysis method used is simplified to permit analysis by hand, creating another uncertainty in the design.

To overcome these uncertainties the safety factor,  $f_s$ , is introduced. The safety factor should be at least 2 since the materials are obtained from worthy suppliers to relevant standards operated in normal environments and subjected to loads and stresses that can be determined using checked calculations [30]. Adding the risk of manufacturing errors of  $10^\circ$  misalignment, and weak spots, the total safety factor is set to be 2.5.

### 6.5.1 Inflation Pressure

The internal pressure in a tube will result in hoop stress  $\sigma_{hoop}$  and longitudinal stress  $\sigma_l$  in the skin of the tube [23]. This effect is displayed in Figure 6.13 and the corresponding relations are given in Equation 6.2.

$$\sigma_{hoop} = 2\sigma_l = \frac{pr}{t} \quad (6.2)$$

Where  $r$  represents the radius of curvature of the rim, which is 17 mm. The internal pressure is given by  $p$ , this is the inflation pressure including the safety factor, 17.5 bar.  $t$  stands for the the thickness of the skin, the rim thickness in this case.

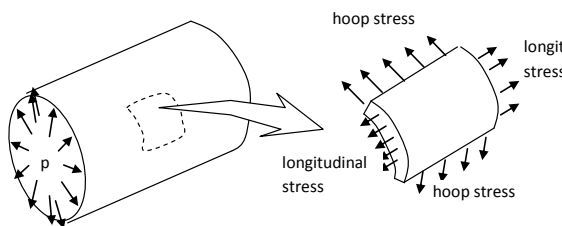


Figure 6.13: Internal pressure resolved in hoop and longitudinal stress [31].

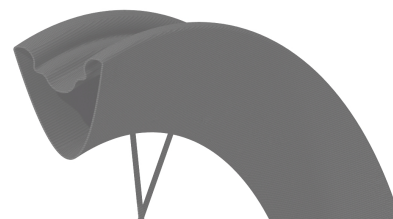


Figure 6.14: Cross-section of the wheel, showing the cross-section of the rim.

The hoop stress will be the critical factor. However, the rim is a hoop around the wheel as well, thus the longitudinal stress can be treated as hoop stress as well. Since the radius of the wheel is larger than the radius of the inner rim profile, the rim should be design for the hoop stress around the wheel. The skin will be loaded in compression in both directions. According to the material properties of the

carbon fiber fabric and epoxy resin, with a fiber direction  $0/90^\circ$ , the compressive strength of the fabric is [32]:  $\sigma_{comp}$  is  $570 \text{ MPa}$ . The required fiber thickness should be  $0.6 \text{ mm}$ . This means that with a fiber fabric thickness of  $0.2 \text{ mm}$  three layers of  $0/90^\circ$  fabric would be sufficient to take the loads due to the tire inflation.

## 6.5.2 Bending Stiffness

To design the rim to prevent it from bending due to the tension in the spokes a simplification of the situation is used. The 12.5% upper part of the rim is taken as a simply supported beam by approximation that is subjected to a load that represents the tension in the spoke. From Section 6.4, this force is found to be  $1201 \text{ N}$ . Requirement W.STF.1 in Table 6.1 stipulates that the radial deflection should not exceed  $0.04 \%$ . For a rim seat diameter of  $406 \text{ mm}$  this corresponds to a maximum deflection of  $\delta$ ,  $0.16 \text{ mm}$ . The formula in Equation 6.3 applies to the situation.

$$\delta = \frac{Fl^3}{48EI} \quad (6.3)$$

The inputs and outputs of the equation are listed in Table 6.14. The Young's Modulus,  $E$ , of  $0/90^\circ$  carbon fiber fabric is  $70 \text{ GPa}$  and for  $+/- 45^\circ$  it is  $17 \text{ GPa}$ . The higher the Young's Modulus, the stiffer the material is, thus the lower the deflection will be. Therefore the  $0/90^\circ$  carbon fiber fabric is selected for the rim. For two layers of  $0/90^\circ$  carbon fiber fabric, the moment of inertia,  $I_{xx}$ , of the rim cross-section is  $1.78 \cdot 10^{-8} \text{ m}^4$ . The maximum deflection is  $0.008 \text{ mm}$  for a thickness of  $0.4 \text{ mm}$ . This maximum deflection is within the requirement including a safety factor.

Table 6.14: Inputs and outputs of equation 6.3

Inputs			Outputs		
$E$	70	GPa	$I_{xx}$	$8.98 \cdot 10^{-9}$	$\text{m}^4$
$\delta$	0.16	mm			
$F$	1201	N			
$l$	0.159	m			

Requirement W.STF.2 in Table 6.1 states that the maximum lateral deflection should not exceed  $0.04\%$ , which again corresponds to a maximum deflection of  $\delta$ ,  $0.1 \text{ mm}$ . In this approach it is assumed that the hub is infinitely stiff and wheel is clamped at the hub. This assumption is acceptable since the hub is connected to the suspension, hence half the wheel will bend around the hub due to the momentum of the lateral force. The maximum lateral force that the wheel should be designed for is  $258 \text{ N}$ . In this approach only half of the applied load is considered as the other half of the rim does not participate in the load transfer. Using Equation 6.4 to check the lateral deflection, a moment of inertia with respect to the y-axis,  $I_{yy}$  is needed for lateral bending. For the rim cross-section with a thickness of  $0.4 \text{ mm}$  this  $I_{yy}$  is given in Table 6.15 and length  $l$  represent a quarter rim length which is  $0.32 \text{ m}$ . The resulting lateral deflection of  $0.13 \text{ mm}$  is within the requirement.

$$\delta = \frac{Fl^3}{3EI} \quad (6.4)$$

Table 6.15: Inputs and outputs of equation 6.4

Inputs			Outputs		
$F$	129	N	$\delta$	0.13	mm
$l$	0.32	m			
$I_{yy}$	$1.6 \cdot 10^{-7}$	$\text{m}^4$			
$E$	70	GPa			

### 6.5.3 Cornering

To make sure that the rim cross-section is stiff enough to take the worst case radial force of 2132  $N$  together with a lateral force of 258  $N$ , including safety factor, these two forces are modeled as shear forces acting on the rim cross-section. As the shear strength of carbon fiber material is known, again the required fabric matrix thickness can be defined to make sure that the rim will not fail. In this structural analysis some assumptions are made, these are listed in Table 6.16. The method used to optimize the

Table 6.16: Assumptions and implications on the structural analysis of the rim

Assumptions	Implications
1. The rim profile is simplified to semi-circular cross-section with a radius of 17 $mm$	The rim will be slightly over-designed.
2. The shear force will be perfectly transferred from the tire to the rim.	The tire and the rim can be seen as one circular cross-section with the same radius. The normal force introduced by the tire on the rim surface are neglected.

cross-section of the rim for the minimum thickness required can be found in sections 17.2 and 17.3 of Aircraft Structures for Engineering Students [23]. For a shear strength,  $\tau$ , of 260  $MPa$ , the result is that the rim shall have a minimum thickness,  $t$  of 0.12  $mm$ . This means that for a fiber fabric thickness of 0.2  $mm$  one layer of  $+/- 45^\circ$  fabric of carbon fiber would be sufficient to take the shear flow due to the normal and lateral force on the road and cornering.

### 6.5.4 Motor Torque and Static Braking Torque

The vehicle shall be able to perform a braking test on a 20% slope. This means that each wheel will be subjected to a radial force due the vehicle weight as well as a torque due to the 20% slope (an angle,  $\alpha$ , of  $11.3^\circ$ ). This torque is caused by the tangential component of radial force of the wheel,  $F_n \sin \alpha$ , and the moment arm of the wheel radius,  $r$ , given in Equation 6.5. Taking a safety factor  $f_s$  of 2.5 into account, a total vehicle mass of 80  $kg$  and a wheel radius of 0.25  $m$ , the total torque on one wheel due to the angle of  $11.3^\circ$  will add up to 96  $Nm$ .

$$T = F_n \sin \alpha r = mg f_s r \sin \alpha \quad (6.5)$$

For the rear wheel, the rim should be designed such that is able to take the torque of the in-wheel motor as well as the torque by the braking on a 20% slope. The in-wheel motor exerts a torque of 1.2  $Nm$  while the torque applied due to the braking in a 20 % slope is about 96  $Nm$ . This means that the all three rims should be design to carry the torque of 96  $Nm$ . Torque in a closed circular section, will result in a constant shear flow [23]. The relation of the torque and the shear flow in the rim is given in equation 6.6, where  $A$  is the enclosed area of the rim and  $q$  is the shear flow. For a wheel radius of 0.25  $m$ ,  $A$  is 0.2  $m^2$ . Then using Equation 6.6 for a torque of 96  $Nm$ , the shear flow in the rim is 245  $N/m$ .

$$T = 2Aq \quad (6.6)$$

$$\tau = \frac{q}{t} \quad (6.7)$$

As the maximum shear flow in the rim is known, the required rim thickness according to the shear strength of the material can be determined by using Equation 6.7. This situation requires a rim thickness of  $2.7 \cdot 10^{-3} mm$  when using  $0/90^\circ$  fabric of carbon fiber.

### 6.5.5 Lay-up

The rims are built from three distinct pieces: two sidewalls and the tire bead. This is shown in Figure 6.15. The two side walls are shaped as circular discs. The main functions of these side walls are to transfer the tension loads from the spokes into rim and to increase the moments of inertia of the rim. Secondly, they are supporting the outer curves of the tire bead of the rim (figure 6.4) to prevent these

form bending. These side walls will be layed-up similarly to the rim profile. The rim is sensitive to bending before the rim is assembled to the spokes. To overcome the risk of any deformations due to handling one extra layer of  $+/- 45^\circ$  is added to the rim. The final lay-up is displayed in Table 6.17.

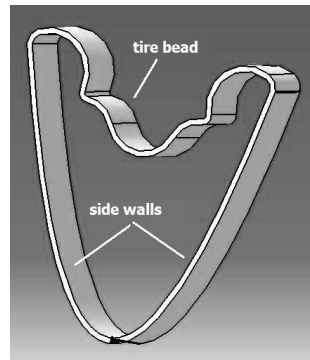


Figure 6.15: A cross-section of the rim profile showing the tire bead and the supporting side walls

Table 6.17: The lay-up of carbon fiber fabrics and its required thickness,  $t$ , for the rims.

Fabric	Fabric thickness [mm]	Required $t$ [mm]	No. of layers	Layer $t$ [mm]
0/90°	0.2	$\geq 0.6$	3	0.6
$+/- 45^\circ$	0.2	$\geq 0.12$	1	0.2
Total rim thickness				0.8

## 6.6 Hub

The hub is responsible for the lateral and torsional stiffness of the wheel. The larger the hub length, the smaller the tensile force in the spokes and the larger the torsional stiffness of the wheel. The dimensions and material specifications of the front and rear wheel hub are summarized in Table 6.18.

### 6.6.1 Hub Design

For the calculations of the hub width, the upper part of the hub is neglected since it is assumed that all loads are going to be transferred directly from the hub to the chassis mountings. As shown in Figure 6.16, when a lateral force,  $F_L$ , is applied, the right side spokes are loaded in tension. The left side spokes are loaded in compression and can be neglected. The experienced lateral force  $F_L$  is distributed among the spokes which acts below the center line of the wheel. According to the presented load case, the lateral cornering force that the vehicle must sustain is 258 N. For this cornering force, the angle between the spokes and the hub is set to be  $16^\circ$  which corresponds to a tensile force of about 400 N per spoke. This tensile force is three times lower than the critical tension given in Table 6.8. The hub width corresponding to an angle of  $16^\circ$  is 70 mm.

### 6.6.2 Rear Wheel Hub

The design of the rear wheel hub is dependent on the dimensions of the in-wheel motor. The inner diameter of the rear wheel hub is 194 mm. The motor is placed within the hub and the axle for the suspension is connected through the bearings with the motor. As the rear wheel is subjected to high torsional loads and the rear wheel hub should be fail safe, it is made of four plies of carbon fiber epoxy matrix. The four plies are layed-up in the following order:  $+/- 45^\circ$ , 0/90°,  $+/- 45^\circ$ , 0/90°.

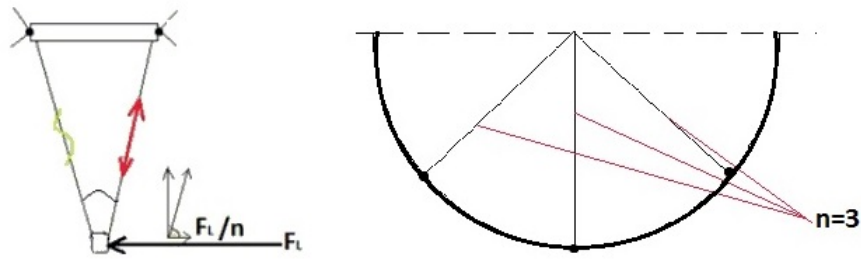


Figure 6.16: The free body diagram (FBD) of the front view (left) of the wheel being subjected by a lateral force and a FBD of the side view (right)

Table 6.18: Dimensions and material specifications of the front and rear wheel hub.

	Front wheel hub	Rear wheel hub
Inner diameter	26 mm	32 mm to 194 mm
Outer diameter	40 mm	200 mm
Width	70 mm	70 mm
Thickness	0.8 mm, four plies	0.8 mm, four plies
Material	Carbon fiber, epoxy	Carbon fiber, epoxy

## 6.7 Bearings

Due to resource limitations and since the bearings are an off-the-shelf product, and the former Eco-Runner team had investigated the effect of bearing size thoroughly it is decided that the same type of bearings will be used. The advantage of choosing the same bearings is that the manufacturer is already known. The bearings size is defined in the design and then purchased via selecting from the SKF catalogue [8]. Different bearings for the front and the rear wheel are chosen, because the front and the rear axles on which the bearings will be used are different in size. The sizing of the axle is based on the loads the wheels have to carry. It will not cost extra resources to select different types of bearings, because these are off-the-shelf products. The specifications of the selected bearing are give in Appendix C.

## 6.8 Production Plan

This subsection includes the explanation of the production of all parts of the wheels as well as the assembly method used between the wheel parts.

### 6.8.1 Lay-up of Rim

As the rim and the spokes will be made out of carbon fiber epoxy matrix, a mold of the product shape is needed. This mold is made out of aluminum, because it can be easily manufactured by milling. For the rim tire bead and the side walls a negative mold is used, to make sure that the outer profile is matching the required rim profile as given by Michelin. In the mold for the rim, the location of the valve should be determined, such that the valve can be placed before the lay-up and that it is thoroughly integrated into the rim. For the same reason as mentioned in Section 4.7.1 the lay-up is done using prepreg carbon fiber fabrics. For the rim, the first lay-up is done with a  $+/- 45^\circ$  fabric. A layer of  $0/90^\circ$  fabric follows and than another layer of  $+/- 45^\circ$  fabric. Next, the rim side walls are layed-up on a negative mold as well. First the fabric is cut in the right shape, and layed-up in the mold.

## 6.8.2 Lay-up of Spokes

The lay-up of the spokes is done using five prepreg layers of UD fibers, on a negative mold. An extra layer of epoxy is applied on this mold initially as a protection layer over the spokes, since they are vulnerable. The front wheel spokes are not cured before being attached to the rim and the hub.

## 6.8.3 Spoke Attachment

By making small incisions in the sidewall layers, the spokes can be pulled through. The spokes are attached to the rim side walls by an adhesive and a carbon fiber patch that are cured together under pressure. This method provides a large surface on which the flat spokes are connected to the rim side walls. The large contact surface provides good load transfer to the rim and it limits locations of high stress. This method does not require any nipples for attachment or any holes have to be made in the rim, these will only weaken the load transfer, while the adhesive and curing the carbon fiber patch will fortify the connection. This method is simple and saves weight.

## 6.8.4 Lay-up of Front Wheel Hubs

The front wheel hubs are made in three parts: Two outer flanges and the middle cylinder that covers the axle. First, the hub flanges are made. In a later stage, the cylinder that connect the two flanges are applied. This is done after the spokes are place in tension, see Section 6.8.6. The prepreg carbon fiber layers of the flanges are cut in circular patches. Cuts are made in the middle of these circles with a length of the hub inner diameter. Then these patches are placed around a metal shaft, such that the cut flanges cover the corners, as shown in Figure 6.19. Next, the plies that cover the first  $5\text{ cm}$  of the axle are wound around the shaft, such that there is some overlap between the middle part of the hub and the flanges as can be seen in Figure 6.20.

## 6.8.5 Lay-up of Rear Wheel Hub

The rear wheel hub is layed-up on a positive mall to make sure that the rim of the in-wheel motor will fit exactly in the hub. The rim of the in-wheel motor is slightly clamped and set in place by using an adhesive.

## 6.8.6 Pre-tensioning the Spokes

The spokes of the front wheels are pre-tensioned after they are connected to the rim side walls and the hub. First, the rim and the rim side walls are pressed and cured together, then the spokes, still only attached at the rim are loosely place on the hub flanges. This is done such that the spoke lengths measure the distance from the rim to the center of the hub before being attached to the hubs. The next step is to bond the spokes to the hub flanges by means of an adhesive. The two hub flanges are pulled apart, creating tension in the spokes as they are pulled into a position that requires them to cover a greater distance. As a last step, the middle section of the hub is placed between the hub flanges to set the distance. These parts are then cured together. The rear wheel spokes are cured, until they are



Figure 6.17: Flat spokes are inserted in a small incision in the rim side wall [33].



Figure 6.18: A carbon fiber patch is applied on the spoke and the rim side wall [33].



Figure 6.19: Lay-up of the hub using a shaft mold. Flanges cut in the fabric cover the corners [33].

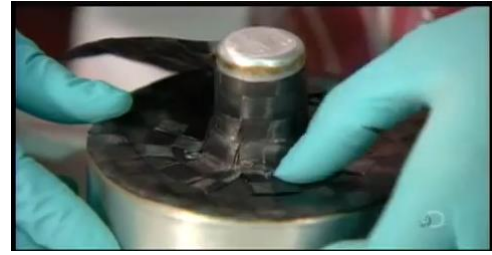


Figure 6.20: Lay-up of shaft and pressing the overlapping flanges in the corners [33].

solidified. They will not be pretensioned, but are simply attached to the surface of the hub by using an adhesive.

## 6.9 Mass and Cost Budget

The mass budget of the wheels including all the components is shown in Table 6.19.

Table 6.19: Mass of the wheels

	Front Wheel [g]	Rear Wheel [g]
Tire 45-75R16	400	400
Rim	90	90
Rim side walls	120	120
Spokes	14	60
Hub	60	300
Valve	20	20
Glue and patches	50	50
Bearings (2x)	44	60
<b>Total mass</b>	<b>798</b>	<b>1100</b>

Carbon fiber is the main material used for production of the wheels. The total amount (in  $m^2$ ) of the carbon fiber material needed for the rims, hubs and spokes is added together and 40% extra is accounted for the material losses during cutting. The cost of the carbon fiber material and all other wheel components is indicated Table 6.20. Furthermore, the costs of are rather high. This number is partly based on the costs of the molds used for the wheels of the Eco-Runner 3. Since the wheels of the new design are made out of more barbon fiber parts than the Eco-Runner 3 these costs will be slightly higher.

Table 6.20: Cost of the wheels

Item	Cost per item [€]	No. of items	Cost [€]
Tire 45-75R16	265.00	3	795.00
Valve	5.00	3	15.00
Bearings	5.00	6	30.00
Adhesive and patches			20.00
Molds			6000.00
Carbon Fiber (Rims, Hubs, spokes)	90.00 €/m <sup>2</sup>	5.6 m <sup>2</sup>	504.00
<b>Total costs</b>			<b>7364.00</b>

## 6.10 Verification and Validation Procedures

The verification for the deflection in lateral and radial direction of the total wheel structure needs more time and expertise in computational structural analysis. It is required to model the total wheel structure and the way the loads are transferred between the rim, spokes and hub before manufacturing. Another requirement to be verified is that the spokes indeed do not buckle, when in compression on the lower half of the wheel. This verification should be performed by means of computational structural analysis as well.

In order to validate the design, some tests need to be performed on the total wheel structure:

- The lateral stiffness shall be tested by hanging the wheel with the axis of rotation in vertical direction constrained at the hub. A weight can be suspended from the rim to represent the lateral force. The displacement of the rim can be measured and the material strain can be recorded using strain gauges and extensimeters.
- The radial stiffness shall be tested by clamping the wheel at the hub with the axis of rotation in horizontal direction. In this case, the radial load can be represented by a weight that is applied vertically on the top of the rim.

## 6.11 Conclusion and Recommendations

The preliminary study of the spokes, rim and hub has helped quantify their load bearing capabilities and overall dimensions. The performed calculations have taken into account both the bending of the rim section and its axial tensile stiffness as well as the axial tensile stiffness of the spokes. Furthermore, the stresses through the rim due to the tire inflation pressure have been calculated. Within the spoke analysis, an extensive study of spoke patterns has been performed and a novel concept has been chosen for the rear wheel. In terms of material selection, carbon fiber was chosen for the spokes, rim and hub. The reasons for this decision are mainly related to the high specific properties of the material, its low density as well as manufacturing considerations such as spoke-rim and spoke-hub attachments. Depending on the loads that the wheel components have been subjected to, the corresponding number of plies and orientation of fibers have been selected. For the front wheel spokes, four layers of unidirectional fibers have been used; the rear wheel spokes have four layers of unidirectional fibers; the rim has three layers of fabric with  $0/90^\circ$  and  $+/- 45^\circ$  orientation and the hub is composed of four plies. With this new design of the front and rear wheels a weight saving of 57% is obtained compared to the wheels of the Eco-Runner 3. Having the complete specifications of all wheel parts, a recommendation for a manufacturing plan has been made.

### 6.11.1 Compliance Matrix

It can be concluded that all of the requirements have been taken into account during the structural analysis for the spokes, rim and hub. The performed check is shown in Table 6.21. Requirement W.D.2 is not satisfied, since the bearing coefficient can not be determined without a test. The requirement is marked with a circle, because the status is not known yet. However, it is important to note that this check is the first of many before the wheel design is used in an Eco-marathon. As a next step, it is recommended that a further study of the interaction between the spoke and the rim is done. Until now, all of the parts have been considered as separate components and sized as such. However, in order to achieve a fully optimized design, the relation between the rim and spokes defining parameters has to be further investigated.

Table 6.21: Compliance matrix of the wheels

Category	ID#:	Requirement:	Check
Drag	W.D.1	Have a maximum rolling friction coefficient of 0.0027 [-] on an asphalt surface in dry conditions.	✓
	W.D.2	Have a maximum bearing friction coefficient of 0.001 [-].	○
Strength	W.STG.1	Support a maximum vertical load of 915.6 N.	✓
	W.STG.2	Withstand a lateral cornering force of 258 N.	✓
	W.STG.3	Withstand a longitudinal acceleration force of 27.8 N.	✓
	W.STG.4	Withstand the longitudinal braking force required to hold the vehicle immobile when placed on a 20° incline.	✓
Stiffness	W.STF.1	Have a maximum radial deflection of 0.04% of its original length.	✓
	W.STF.2	Have a maximum lateral deflection of 0.04% of its original length.	✓

### 6.11.2 Final Wheel Design

The final design of the wheels is shown in Figure 6.21 and Figure 6.22.



Figure 6.21: Front wheel



Figure 6.22: Rear wheel



# 7 Electronic Systems

This chapter shows the electrical system of the Eco-Runner vehicle. In this section, a block diagram of the whole system, hard and software diagrams, data handling diagram, and some parts of the system are determined and described. Finally, a cost and mass budget has been made and in the final section some recommendations are given for future research.

## 7.1 Electrical System

This section contains the layout of the electrical system. Figure 7.1 shows the electrical system block diagram. The system is split up into several blocks, power is indicated with lines and signals are indicated with arrows.

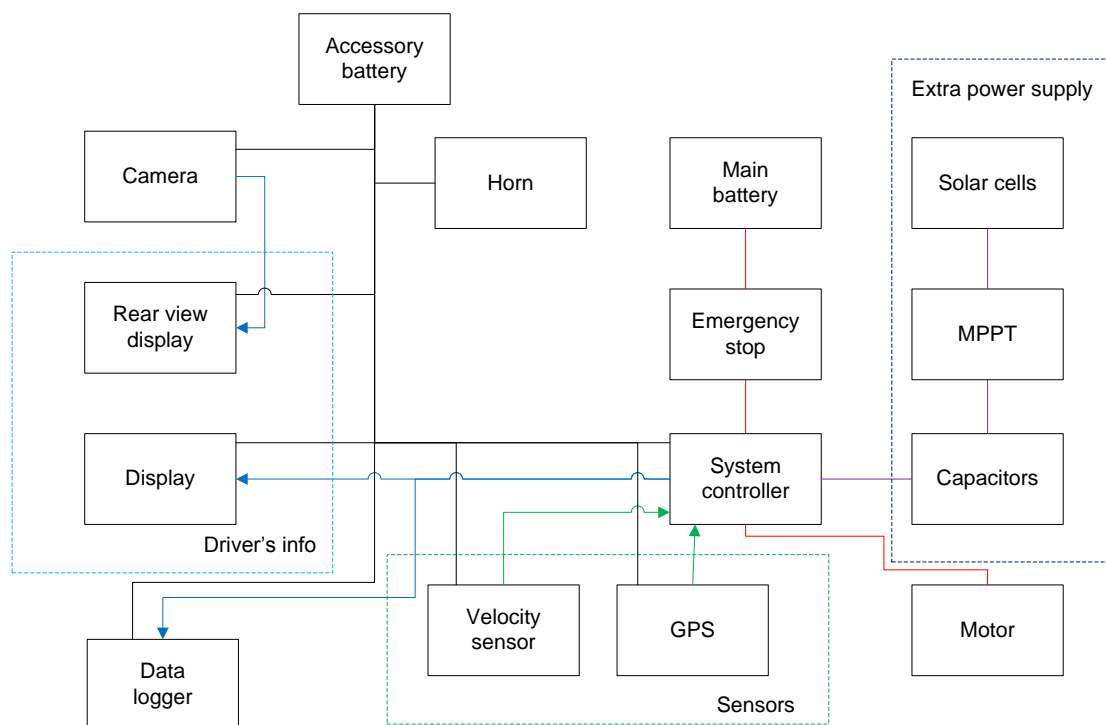


Figure 7.1: Electrical system diagram

The main block in the diagram is the system controller. The system controller is powered by the accessory battery and controls the power to the motor. The power of the motor comes from the main battery and from the solar cells. The system controller determines if the power comes from the solar cells or from the main battery. In between the system controller and the main battery there is the emergency stop, which is required by the rules.

For the extra power supply, also some extra steps are necessary. First, a maximum power point tracking (MPPT) is necessary. This device is used to get maximum power from the solar cells. It is also used for getting the output voltage on the desired voltage, as does a DC-DC converter. A separate DC-DC converter could be used, however most MPPT's consist of a DC-DC converter. As discussed in Chapter 8, no constant power is needed by the motor. It is better to store the energy from the solar cells

in capacitors. This way the highest amount of energy can be used from the solar cells.

The lines coming from the sensors are signal lines. The signals are an input for the system controller. The signals are used for data logging and for the driving strategy. They also supply the information to the driver on a display.

Finally, there is the accessory battery circuit. The accessory battery supplies power to the camera, horn and the rear view display. The camera gives a signal to the rear view display to give the pilot a better visibility.

### 7.1.1 Hardware Diagram

Figure 7.2 shows the hardware diagram of the Eco-Runner. The central blocks are the general power system with power coming from the battery management system (BMS), consisting of the battery and DC-DC converters, and the maximum power point tracking (MPPT), which is connected to the solar cells. The system controller gets input from the sensors and the driver's input. This input will be converted to an output, which goes to the displays for the driver, the data logger and the motor.

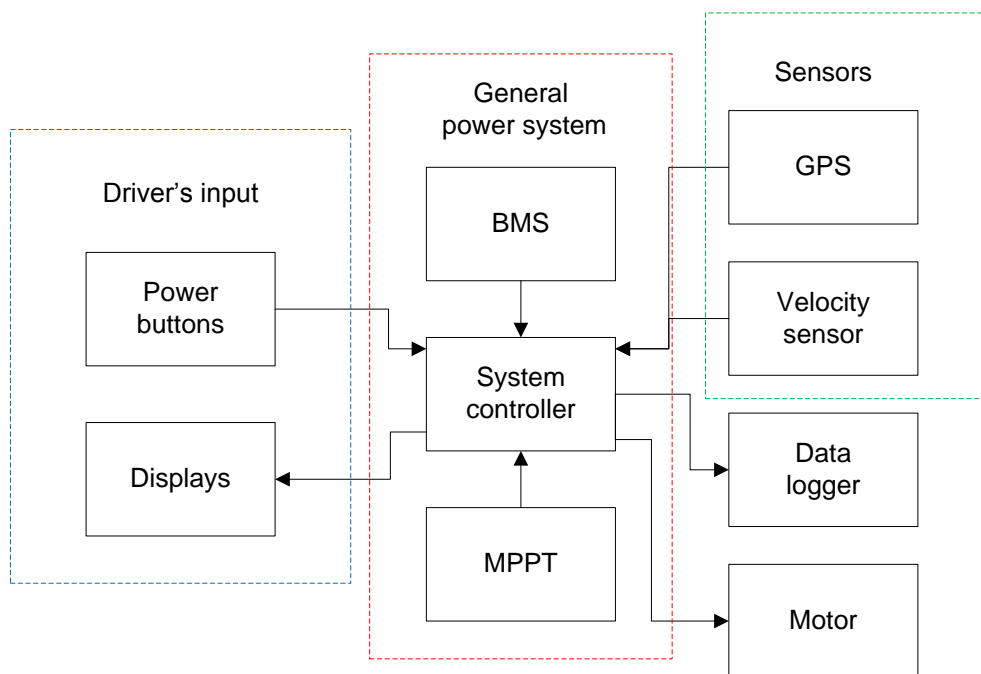


Figure 7.2: Hardware diagram

### 7.1.2 Software Diagram

Figure 7.3 shows the software diagram. The software diagram consists of a loop coming from the driver's input to the system controller memory, which then goes to the driver's display. This display gives the information again for the driver's input. Next to this loop there is one box, the data logger. The data logger logs all the data of the vehicle for analysis after the race. This data consists of when the vehicle is accelerating and the location of the vehicle, which shows what driving line the driver took.

### 7.1.3 Data Handling Diagram

The data handling diagram can be found in Figure 7.4. The figure not only shows the data handling within the vehicle, but also with the scouts, who are placed at certain places around the track, and the command center. The command center receives all data from the scouts and the vehicle and decides

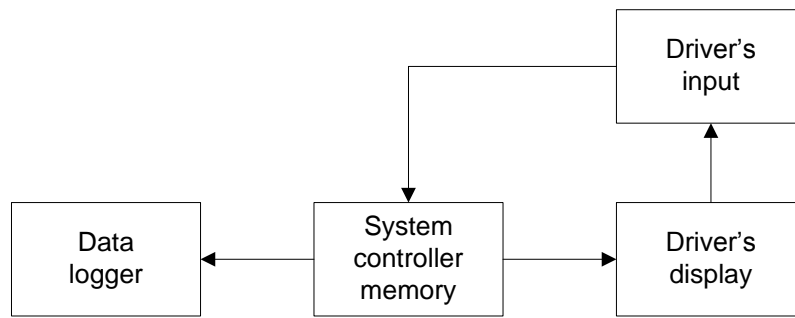


Figure 7.3: Software diagram

what the best strategy for the race at a particular point in the race is. This strategy then is send to the vehicle. The data obtained by the scouts are the road, vehicle, race and weather conditions. The road conditions consists of information about the track it self. For example, there could be some debris from other cars on the track. The vehicle conditions are also useful, because it could be that some parts of the vehicle are starting to fail under the loads. It could be possible that the fairings are starting to drag on the ground. The race conditions consist of the location of the other participants on the track and if it possibly is necessary to overtake or to let one overtake. Finally, the weather conditions are monitored by the scouts. In case of rain the vehicle should stop as soon as possible, because it could damage the electronics in the vehicle. The electronics could be protected by putting it in a box, however this would probably increase the temperature of the electronics and also the weight of the vehicle would increase. Rain would also decrease the grip of the vehicle and the vehicle would be harder to steer by the driver. It is better to stop when it starts to rain.

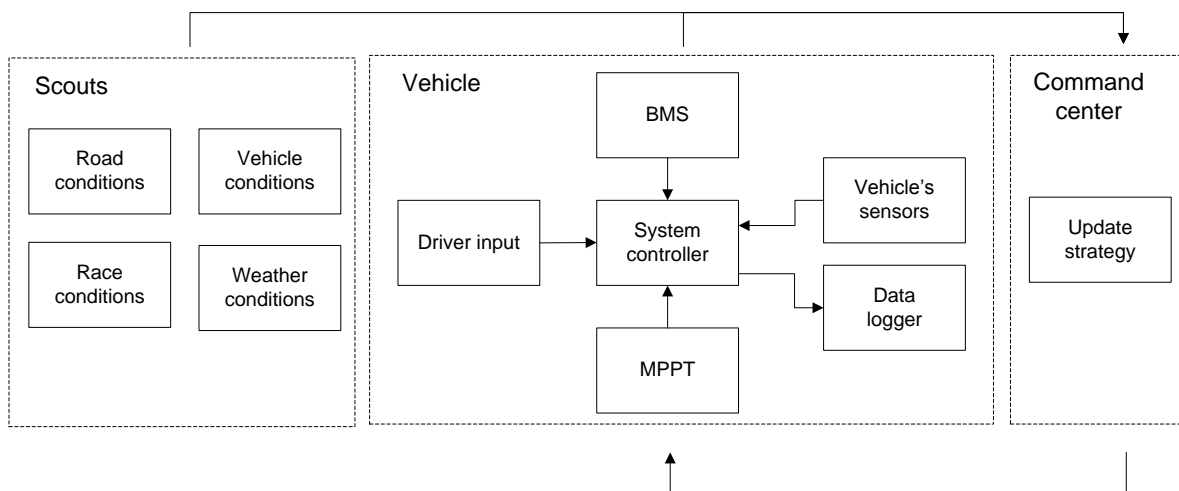


Figure 7.4: Data handling diagram

## 7.2 Communication Flow Analysis

In this section the communication flow is described. The major system in the communication flow is the microcontroller (e.g. an Arduino). Other subsystems of the Eco-Runner vehicle are controlled directly by the pilot, thus no communication flow takes place other than direct communication. The microcontroller gets an input velocity from the velocity measurement device, for an accurate velocity, and decides if it needs to increase the velocity or not, because one of the requirements is a minimum average velocity over the race of 25 *km/h*. If the average velocity is too low at a particular moment, the microcontroller signals the electric motor to accelerate.

Another signal from the microcontroller goes to a display to the driver to show the average velocity and the velocity at that moment. The driver has the ability to overrun the microcontroller's decision of increasing or decreasing the velocity in case the pilot and the team think that the minimum average velocity will not be met at the finish.

The final signal coming from the microcontroller goes to a small computer (e.g. a Raspberry Pi) for data logging the velocity. This makes it possible to check after the race if the right driving strategy was used for the highest possible efficiency.

### 7.3 Propulsion Battery

For the battery there are not many options to use. As is explained in the mid-term report [13] only lithium-ion batteries are allowed. At the moment, lithium cobalt oxide is the best choice. It has the highest energy density and specific energy from the available lithium-ion batteries on the market. In the future, this type of battery can be replaced with lithium-sulfur, since it has a much higher energy density than lithium cobalt oxide. However, these batteries are not yet on the market, because they are not proven to be reliable enough. From all lithium cobalt oxide batteries available on the market the Panasonic NCR-18650A is considered as one of the best and proven to be reliable. Specifications of this lithium-ion can be found in table 7.1.

Table 7.1: Specifications of a single Panasonic NCR-18650A cell [4]

Panasonic NCR-18650A		
Capacity	3100	<i>mAh</i>
Voltage	3.6	<i>V</i>
Mass	45.5	<i>g</i>
Diameter	18.6	<i>mm</i>
Length	65.2	<i>mm</i>

The discharge characteristics of this cell can be found in figures 7.5 and 7.6. From the first figure can be concluded that it is possible to discharge the battery in 2.0 *lt* (load time) with a current of 5900 *mA*. There is also another Panasonic cell available on the market, the NCR-18650PD, which has a higher allowed current of 10 *A*. However, since there is not much known about these cells and the high risks, as being described in section 7.3.1, it was chosen to use the more reliable NCR-18650A. Using this current and the voltage given by the battery, the power of the battery can be calculated using Equation 7.1.

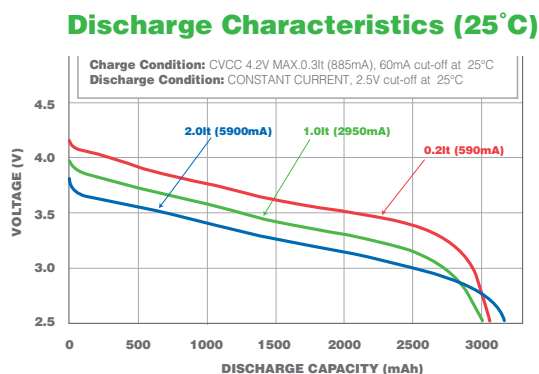


Figure 7.5: Discharge characteristics for different load times

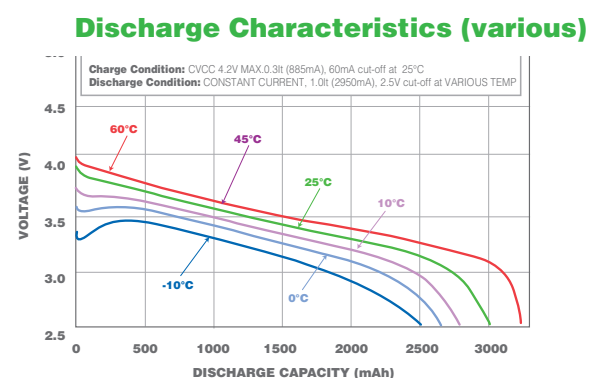


Figure 7.6: Discharge characteristics for different temperatures

$$P = U \cdot I = 3.6 \cdot 5.9 = 21.24[W] \quad (7.1)$$

From the motor data, Appendix D, obtained from the previous Eco-Runner team it can be concluded that power needed to accelerate from low velocities is  $100\text{ W}$ . This is the maximum power the battery has to deliver. When the vehicle is driving at a higher velocity, its efficiency is higher and the power needed to accelerate the vehicle is lower. This is due to the design range of the motor. From Equation 7.2, it can be concluded that for the maximum power needed by the motor five NCR-18650A batteries are needed in series.

$$n = \frac{P_{motor}}{P_{battery}} = 100/21.24 = 4.71 \quad (7.2)$$

The next step is the needed capacity to complete the race. Since the targeted efficiency of  $0.790\text{ km/Wh}$  and the total race distance of  $16.12\text{ km}$  is known, the energy needed for this can be calculated according to Equation 7.3.

$$E_{total} = \frac{s_{race}}{\eta} = \frac{16.117}{0.790} = 20.4[Wh] \quad (7.3)$$

The capacity of the Panasonic NCR-18650A is given in ampere-hours. This can be transformed to watt-hours by multiplying it with the voltage. The resulting capacity then becomes  $55.8\text{ Wh}$ . This is higher than the energy calculated in Equation 7.3. From this can be concluded that the cells do not have to be placed parallel. Considering the results from the simulation in Chapter 8 this should be more than sufficient energy to complete the race.

From this it can be concluded that five cells are required. The total weight of the battery would become  $227.5\text{ gr}$ . Since one cell only weights  $45.5\text{ gr}$  adding some extra cells will not decrease the efficiency a lot. Adding some extra cells, however, would increase the voltage and decrease the current needed. This will increase the battery performance and lowers the heat in the cables from the battery to the motor. More power becomes available for the motor, since the motor can use up till  $150\text{ W}$ . When six cells are used, the voltage provided by the battery is exactly in the voltage range of the motor as can be seen in section 7.5. So no DC-DC converter has to be used, which would decrease the efficiency of the total electronic system.

The resulting specifications of the Eco-Runner battery can be found in Table 7.2.

Table 7.2: Resulting battery

Eco-Runner battery		
Type	Panasonic NCR-18650A	
Parallel cells	1	
Cells in series	6	
Total number	6	
Voltage	21.6	$V$
Capacity	3100	$mAh$
Mass	273	$g$

### 7.3.1 Risk Analysis

During its lifetime the battery is exposed to certain risks. Major risks are listed below, after which they are mapped in Section 2.5:

1. lowering performance due to charge/discharge cycles;
2. failure due to too many charge/discharge cycles;

3. failure due to deep discharge;
4. lowering performance due to a bad battery management controller.

The lowering performance due to charge and discharge cycles is impossible to avoid, however the performance decreases slowly till the real failure of the battery. This failure is e.g. that it does not charge anymore. The failure of the battery due to the charge and discharge cycles can be very catastrophic, because this failure can lead to an explosion or fire of the battery. This is happening when the battery is short circuit. This can happen when the internal membrane, separating the positive and negative electrodes, is starting to break down due to internal heat. Failure of the battery can also cause a lot of damage to other parts of the vehicle and should absolutely be avoided.

Deep discharge should really be avoided. Deep discharge is happening when the voltage of the battery is below a certain point. Deep discharge causes a lot of performance loss to a lithium-ion battery and can lead to failure of the battery. The battery management system is really important for lithium-ion batteries. However, every lithium-ion battery is supplied with its own controller. If this controller is being used for charging and discharging the probability of failure is very low. If it is decided to use a different controller the probability of this risk will increase a lot, because for lithium-ion batteries it is very important that charging and discharging is done correctly due to the sensitivity of the membrane in the battery.

## 7.4 Solar Cells

For the battery electric vehicle class in the Shell Eco-marathon it is allowed to use solar cells, according to the rules [9]. Since the energy gained from the solar cells is not measured for the efficiency of the vehicle, they should definitely be added. For the next Eco-Runner it is chosen to use the ZTJ Photovoltaic Cell, an advanced triple-junction solar cell for space applications. Specifications of this cell can be found in Table 7.3.

Table 7.3: Specifications of a single cell [5]

Emcore ZTJ Photovoltaic Cell		
Voltage	2.41	<i>V</i>
Current	16.5	<i>mA</i>
Power	0.04	<i>W</i>
Mass	0.084	<i>gr</i>
Area	100	<i>mm<sup>2</sup></i>
Efficiency	29.39	<i>%</i>

According to the rules it is allowed to use  $0.17 \text{ m}^2$  for solar cells. This results in a total weight of  $0.14 \text{ kg}$  and a power of  $67.7 \text{ W}$ . However, the specifications are obtained by an intensity of  $1353 \text{ W/m}^2$  and the average solar intensity in the month May in Rotterdam is only  $750 \text{ W/m}^2$  [13]. Correcting the power gained by the solar cells for this intensity would result in a power of  $37.5 \text{ W}$ .

As can be seen in the results from the driving strategy, this would be enough to power the vehicle from lap two till ten. Only in the first lap when the vehicle has to accelerate from  $0 \text{ m/s}$  it is not enough and it has to use the battery.

To get this power from the solar cells, a maximum power point tracker (MPPT) is needed. Since the output of the solar cell is depending on solar intensity, temperature and total resistance, a MPPT is needed to get the maximum power from the solar cells, this is done by smoothing the output of the current and voltage.

## 7.5 Motor

In the mid-term report [13], a trade-off was made for the motor. From the trade-off, the best result was the in-wheel brushless DC motor. Mainly because, in theory, it had the highest efficiency. For the next Eco-Runner, it is decided to go with the same motor as the previous Eco-Runner. This motor was developed by the company Mitsuba from Japan and is made specifically for the Eco-Runner. It is designed to work on the voltage coming from the hydrogen fuel cell. This does not have to be a problem for the lithium-ion powered vehicle designed in this report, since the battery from Section 7.3 is in the voltage range of the motor.

Specifications of the motor can be found in Table 7.4. These are data obtained from Mitsuba. More data about the motor can be found in Appendix D. These are data obtained by the current Eco-Runner team during testing.

Table 7.4: Motor specifications obtained from Mitsuba

Mitsuba M00512-IV		
Voltage	12	<i>V</i>
Rated output	50	<i>W</i>
Maximum output	150	<i>W</i>
Maximum efficiency	93	or more %
Diameter	194	<i>mm</i>
Length	106	<i>mm</i>
Weight	3.4	<i>kg</i>

The motor controller used for the motor will also be the one supplied by Mitsuba. Since this one is specifically made for this motor, it will have the best performance. The input voltage of the controller is 12 *V* till 24 *V*. As can be seen in Section 7.3, the voltage of the battery is in the range of the motor controller.

## 7.6 Other Systems

### 7.6.1 System Controller

The general controller in the electric system was decided to be a microcontroller, as was explained in the mid-term report [13]. On the market many microcontrollers are available in different sizes and placed on different boards. One of the most used microcontrollers is the Arduino UNO R3. It is the newest board in the Arduino series. These microcontrollers are easy to use and program. Also they are not expensive (€25). The power used by the Arduino should be measured before using it. Since it depends on what the Arduino has to do, no real estimation can be made at this point. Some specifications of the Arduino can be found in Table 7.5.

Table 7.5: System controller specifications [6]

Arduino Uno R3		
Microcontroller	ATmega328	
Input voltage	7 – 12	<i>V</i>
Digital I/O Pins	14	
Analog Input Pins	6	
Flash memory	32	<i>KB</i>
SRAM	2	<i>KB</i>
EEPROM	1	<i>KB</i>
Clock speed	16	<i>MHz</i>

## 7.6.2 Data Logger

For the data logger, it is chosen to use a Raspberry Pi model B, because it is easy to use and it is used a lot in combination with the system controller. A Raspberry Pi is a singleboard computer using an ARM processor. On this computer it is possible to install an operating system (OS) called Raspbian. This is a Linux based OS. The Raspberry Pi can be connected to the Arduino, discussed in Section 7.6.1, to log all the calculations and measurements done by the Arduino. This data can be used after the race to check if everything was working properly and maybe some extra changes are necessary on some points. The specifications of the data logger can be found in Table 7.6. There is also a model A version of the Raspberry Pi available on the market, which uses less power and has less internal memory. However, since the data logger is allowed to be powered by the accessory battery the model B version is the better choice.

Table 7.6: Specifications of the data logger [7]

Raspberry Pi model B		
Memory (SDRAM)	512	<i>MB</i>
Input voltage	5	<i>V</i>
Input current	700	<i>mA</i>
Input power	3.5	<i>W</i>
Length	85.6	<i>mm</i>
Width	53.98	<i>mm</i>
Mass	45	<i>g</i>
Storage	SD card	

## 7.6.3 Accessory Battery

The rules of the Shell Eco-marathon state that it is allowed to have one propulsion battery and one accessory battery [9]. Since it is beneficial to use the propulsion battery only for powering the motor, all other parts should be connected to the accessory battery. The accessory battery should be able to power the horn, driver's display, camera, camera displays, data logger, and the system controller. For the dimensions and specifications of this battery, first separate systems should be analyzed for the amount of power they need. When this is known, the accessory battery can be designed. The only constraint is that it should be a lithium-ion battery. As explained in Section 7.3, the Panasonic NCR-18650A cell shows the best performance and should also be used for the accessory battery.

## 7.7 Cost and Mass Breakdown

The cost and mass breakdown of the electrical system can be found in Table 7.7. In the table it can be seen that the total mass of the electrical system is  $5.378 \text{ kg}$ . Comparing this with the weight of the electrical system of the previous Eco-Runner of  $14.140 \text{ kg}$ ,  $8.762 \text{ kg}$  has been saved. Because of the use of a battery instead of the fuel cell used in the Eco-Runner 3. However the solar cells, including the MPPT, decrease this weight saving again.

For the total cost of the vehicle, many parts that the Eco-Runner team already bought are included. For example the motor, system controller, camera's, displays, horn and cables are already available. These parts are indicated (\*) in the table. Only the propulsion battery and the solar cells are not available yet.

Table 7.7: Cost and mass breakdown of the electrical system

	Amount	Single part		Total system		
		Cost [€]	Mass [g]	Total cost [€]	Total mass [g]	
Propulsion battery	6	5	45.5	30	273	
Motor	1	1800	3400	1800	3400	*
MPPT	1	150	750	150	750	
System controller	1	25	30	25	30	*
Data logger	1	35	45	35	45	
Solar cells	1	3000	140	3000	140	
Accessory battery	1	35	40	35	40	*
Camera	2	30	50	60	100	*
Displays	3	20	50	60	150	*
Horn	1	10	400	10	400	*
Cables	1	10	50	10	50	*
<b>Total</b>				<b>5215</b>	<b>5378</b>	

## 7.8 Recommendations

For the next Eco-Runner, more research should be done on the electronics. With a good and complete electronic system, the efficiency of the vehicle can increase further. Not every part of the electronic system is discussed in this report due to a lack of time. Every subpart should be investigated separately and should be optimized for weight saving, performance and power consumption. Not only for the propulsion battery powered parts, but also for the parts powered by the accessory battery.

More effort should be put in the solar cells. For example, in storing the energy in supercapacitors and in how to place them on the body for the maximum power output. For the design in this report, the solar cells are placed on top of the vehicle as can be seen in Section 9.7. It could be beneficial to place them under an angle or more on the back of the vehicle. Since the energy from the solar cells is 'free energy', as it does not count for the energy used during the race, they should definitely be further investigated.

## 7.9 Compliance Matrix

Looking at the requirements set in the mid-term report [13], it can be concluded that not all of them have been met. The performed check is shown in Table 7.8. The requirement EI.R.4 is not met, because battery management systems were not looked into sufficiently. EI.R.5 is not met, since this is a requirement that has to be kept in mind when installing all the parts in the body. Since the brakes have not been further investigated, requirement EI.I.6 and EI.I.7 are not met either. The final requirement that is not met, is requirement EI.Pb.3. From the Shell Eco-marathon rules, the control systems are allowed to be powered by the accessory battery. This way, the requirement becomes much less important.

Table 7.8: Compliance matrix electronic systems

Category	ID#:	Requirement:	Check
Rules	EI.R.1	All parts of the drive train shall be within the confines of the body cover.	✓
	EI.R.2	The maximum voltage on board at any point shall be less than 48 V nominal and 60 V max.	✓
	EI.R.3	The vehicle shall only contain one propulsion battery and one accessory battery.	✓
	EI.R.4	Battery Management Systems (BMS) tailored to this chemistry shall be installed to control and protect the battery against risk of fire.	○
	EI.R.5	The propulsion battery or super capacitors, both positive and negative circuits shall be electrically isolated from the vehicle frame and the accessory battery circuit.	○
	EI.R.6	The electric storage devices shall be lithium-ion batteries.	✓
	EI.R.7	The solar cells shall be fully integrated into the bodywork of the vehicle.	✓
	EI.R.8	The total combined surface area of the solar cells shall be less than 0.17 m <sup>2</sup> .	✓
Interfaces	EI.I.1	The motor will fit in the body	✓
	EI.I.2	The motor shall be compatible with the wheels and the steering system	✓
	EI.I.3	The battery will fit in the body.	✓
	EI.I.4	The battery will deliver enough power for the motor to operate.	✓
	EI.I.5	The solar cells will be integrated in the body.	✓
	EI.I.6	The regenerative braking will be working together with the motor and normal brakes.	X
	EI.I.7	The storage system will work together with the other electrical systems with the motor and normal brakes	○
Mass budget	EI.Mb.1	The total drivetrain shall have a maximum mass of 3.5 kg.	✓
	EI.Mb.2	The electronic systems shall have a maximum mass of 2 kg.	✓
	EI.Mb.3	The solar cells will deliver more power than the power required by the addition of the mass.	✓
Power budget	EI.Pb.1	The drivetrain shall be able to provide an average velocity of 25 km/h to the vehicle.	✓
	EI.Pb.2	The drivetrain shall be able to provide a maximum velocity of 35 km/h to the vehicle.	✓
	EI.Pb.3	The control systems for the electronics shall have a maximum power of 3 W.	X

# 8 Driving Strategy

This chapter deals with the driving strategy for the Shell Eco-marathon. Infinite racing strategies exist, of which the best should be selected. One might for example use a constant propulsive force, whereas another chooses to drive at a constant velocity. Not every strategy is as energy efficient as another. In this chapter, a simulation model is created to compare several strategies. Both an analytical and a numerical model is built, after which the simulation is verified. A validation plan is presented as well. Moreover, several strategies are tested with the model and a sensitivity analysis is performed, showing the influence of vehicle parameters on the performance in the race. Then, the operations and logistics and the communication flow is analyzed. Finally, a conclusion is drawn and recommendations are given.

Before actual modeling, assumptions are made simplifying the model significantly. The assumptions are listed below and explained thereafter.

1. A simplified track model is used.
2. The vehicle behaves as a unicycle instead like a tricycle.
3. The motor is used on its most efficient setting.
4. No wind exists around the track.
5. Tire slip angles are small.
6. All laps are similar and no other vehicles are on the track.
7. All systems (except for the motor) have a 100% efficiency.
8. No solar cells are installed on the vehicle
9. Atmospheric conditions are constant.

The first assumption implies that the track has very regular properties. For one, the track is flat, removing the effect of inclination- and banking angles. Furthermore, turns in the track have a constant radius. It is also assumed that the track has no width, because the vehicle is following a single line instead of a track with a width. The second assumption states that the vehicle has only one tire, instead of three. This helps simplifying the calculations for the cornering drag a lot. According to [10], the unicycle model yields a 20% higher cornering drag than the more realistic tricycle model. Since the cornering drag is only a fraction of the total drag, the unicycle estimation is valid. The unicycle also implies that the vehicle does not rollover while turning. Tire slip angles, mentioned in the fifth assumption is the angle between the tire and the path. As the velocity of the vehicle is not likely to exceed  $9\text{ m/s}$ , the angle can be assumed small. Assumption six, laps two to nine are similar is because the vehicle does not have to start at  $0\text{ m/s}$  and does not have to slow down for the finish. So the vehicle starts the lap at a velocity and ends on the same velocity. For lap one and lap ten a different strategy has to be decided. Also, it is assumed that there are no other vehicles on the track. In reality there are other vehicles that have to be overtaking or will overtake the Eco-Runner. However, because of a lack of time this was not implemented in the simulation.

## 8.1 Analytical Model

In this section the analytical model is considered. In this model the track is continuous and the velocity is kept constant. The propulsive force is calculated by using the fact that it has to compensate for every drag force. These drag forces are the aerodynamic drag, rolling resistance, slope resistance and the cornering drag force. The aerodynamic drag force can be calculated as follows:

$$F_a = C_D \cdot \frac{1}{2} \rho \cdot v_{air}^2 \cdot A_f \quad (8.1)$$

The rolling resistance can be calculated according to Equation 8.2

$$F_{r\parallel} = C_r \cdot m \cdot g \cdot \cos \alpha \quad (8.2)$$

If the inclination angle of the track is not zero, also a slope resistance would have acted on the vehicle:

$$F_{r\perp} = m \cdot g \cdot \sin \alpha \quad (8.3)$$

Adding Equation 8.2 and 8.3 would result in the total rolling resistance. The final force acting on the vehicle is the cornering drag force. For calculating the cornering drag, first the centripetal force has to be calculated according to Equation 8.4. Using this force, the cornering drag force can be calculated using Equation 8.5.

$$F_y = m \frac{v^2}{r} \quad (8.4)$$

$$F_t = \left| \vec{F}_y \right| \sin \left( \frac{\left| \vec{F}_y \right|}{C_\alpha} \right) \quad (8.5)$$

Because the velocity is assumed to be constant, the acceleration has to be zero. Using Newton's second law the resulting force acting on the vehicle also has to be zero. This results in the following equation for the propulsion force:

$$F_p = F_t + F_a + F_{r\parallel} + F_{r\perp} \quad (8.6)$$

When this propulsion force is known, the efficiency of the motor can be found from the test results of the motor from the previous Eco-Runner Team. This motor will also be used for the next Eco-Runner as is being explained in Chapter 7. Using these values the energy lost can be determined with Equation 8.7.

$$E_{lost} = \int_{s_{start}}^{s_{finish}} F_{prop} \cdot \eta_{motor} \cdot ds \quad (8.7)$$

Using the lost energy and the total distance on the track, the efficiency of the vehicle can be calculated according to Equation 8.8.

$$\eta = \frac{E_{lost}}{s_{track}} \quad (8.8)$$

## 8.2 Numerical Model

Whereas the previous section elaborated on an analytical method for determining the energy efficiency of a particular driving strategy, this section presents a numerical procedure. The procedure is also presented in a flow chart, which can be transformed into a useful design tool for the driving strategy in MATLAB. The calculation procedure and the assumptions are similar to the analytical model.

For the numerical model, first a strategy should be selected as an input. Then, the track is divided into numerous segments. From the track data, track properties, such as radius of curvature, are retrieved. The next step of the program involves calculating the drag- and propulsive forces, dynamic values, such as the velocity and acceleration, and the energy used at each track segment. When the calculations for each track segment are finished, the results of the strategy are computed. The output consists of the energy efficiency of the vehicle for driving ten laps, which is the number of laps driven in the competition. A flow chart of the simulation is presented in Figure 8.1. Here it can be seen that the program has several independent modules, each with different in- and outputs.

**Initialization:** The program is started, and the required input parameters are entered by the user. Inputs are strategies, vehicle characteristics and the time interval from the time vector. Other inputs are data of the motor and track, as well as the air density  $\rho$  of  $1.225 \text{ kg/m}^3$ .

**Begin at first strategy:** The first strategy is selected to start the program. Inputs are all strategies, the first strategy is the output.

**Begin at "Start" of the track:** The first track segment is selected. The input is  $s$ . Outputs are the initial conditions (e.g.  $v_0$  and  $E_{lost,0}$ ).

**Calculate drag forces:** The drag of the vehicle at the particular track segment is determined. Inputs are  $v$ ,  $\rho$ ,  $A_f$ ,  $C_D$ ,  $m$ ,  $C_r$ ,  $C_\alpha$  and the track data. The output is the total drag force acting on the vehicle.

**Calculate propulsive forces:** The force by the motor propelling the vehicle is computed. Inputs are  $v$ , the motor data, the total drag force and the strategy. The propulsive force and the efficiency of the motor are given as an output.

**Calculate dynamic values:** Dynamic values, such as  $s$ ,  $v$ ,  $a$ , but also  $t$  are calculated, hence they are outputs. Inputs are the propulsive- and total drag force, as well as the time interval and the vehicle mass. It must be noted that the calculated  $t$ ,  $s$  and  $v$  are defined at the very end of the relevant track segment, whereas  $a$  is the acceleration during the segment.

**Calculate energy:** Here, the energy spent on the defined track segment is defined. Inputs are  $v$ , the time interval and the motor efficiency. The single output is the energy spent.

**Reached the "Finish"?** After calculating everything for a distinct track segment, another segment should be treated, unless the final segment was reached.

**Determine results:** The results of the strategy are calculated. This is done with the inputs:  $s$ ,  $t$ ,  $v$  and the energy spent at each segment. The outputs are the vehicle efficiency over one lap, its mean velocity and its end velocity for each lap.

**Treated all strategies?** If there are more strategies to be treated by the program, the cycle is repeated. Otherwise, the program moves on.

**Display comparison of strategies:** Inputs are the

strategies and the vehicle efficiency, mean velocity and end velocity of each strategy. Then, an output is produced consisting of an overview of each strategy with its characteristics. Finally, a choice between the different strategies can be made by the user.

**Termination:** The program is terminated. Windows and variables are cleared if demanded by the user.

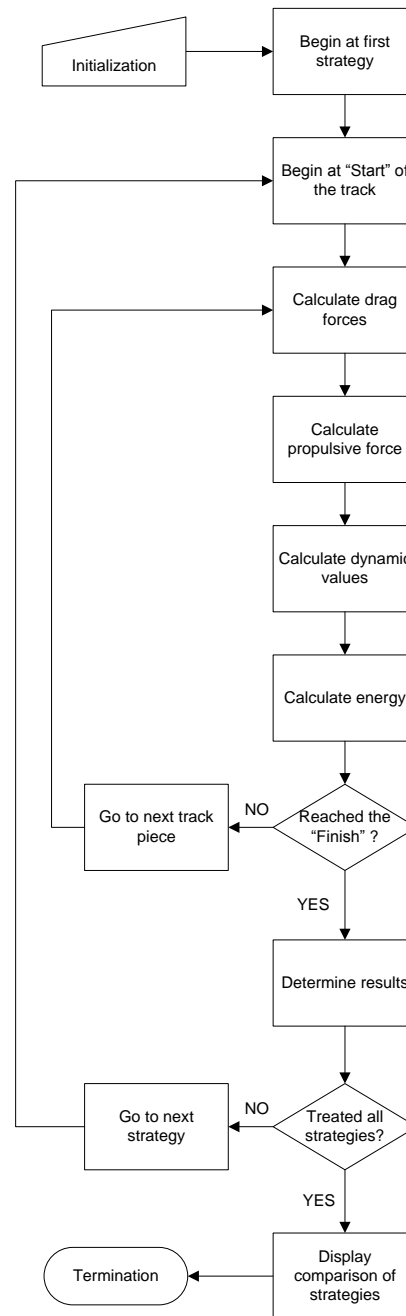


Figure 8.1: Flow chart for the simulation program

### 8.3 Strategies and Results

For finding the best strategy for the race, several strategies were composed. Requirements on strategies are an average velocity and an end velocity of  $7.5 \text{ m/s}$ , such that the race is completed within the time limit and the results are valid for the entire race, instead of a single lap. The corresponding track sections are shown in figure 8.2. The tested strategies were:

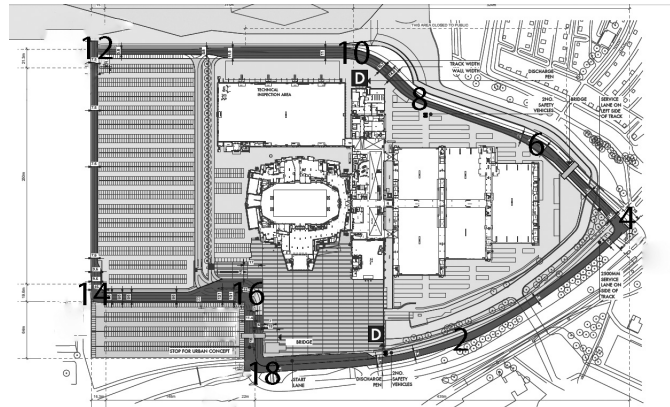
1. Stay at a constant velocity of  $7.5 \text{ m/s}$  on straights and in all corners. This is the only strategy that does not use the assumption of having the motor on its highest efficiency. For this strategy the motor efficiency is based on its propulsion force, which should be equal to all the drag forces.
2. Drive continuously on the maximum efficiency of the motor at a given velocity.
3. Drive at the maximum efficiency of the motor at the given velocity, but turn off the motor when the velocity becomes higher than  $7.5 \text{ m/s}$ .
4. Turn the motor off in every corner, after which the velocity is increased to more than  $7.5 \text{ m/s}$ . The motor is working on its highest efficiency for the given velocity.
5. Drive at highest efficiency of the motor, but turn the motor off in every corner except for section 2 of the track. Increase the velocity for turning off the motor till the average velocity is higher or equal than  $7.5 \text{ m/s}$ .
6. Same strategy as strategy five, however, now the motor is also turned on in section 18.
7. Turn the motor only off in the sharp corners (radius less than  $25 \text{ m}$ , track sections: 4, 12, 14, 16 and 18), drive at the highest efficiency of the motor and turn off the motor when velocity is higher than  $7.7 \text{ m/s}$ .
8. Same strategy as strategy 7, but the motor is now turned on in the final corner.

Table 8.1: Constants used in the simulation

Parameter	Value	Unit
$A_f$	0.285	$\text{m}^2$
$C_D$	0.075	–
$C_r$	0.00081	–
$C_\alpha$	13751	–
$m$	73.6	$\text{kg}$
$v_0$	7.5	$\text{m/s}$
$\rho$	1.225	$\text{kg/m}^3$
$dt$	0.1	$\text{s}$

More details on the maximum efficiency of the motor can be found in Appendix D. For the third strategy, it is possible to turn the motor off at  $7.5 \text{ m/s}$  because of the high propulsion force the vehicle gets from the motor, which will give the vehicle a large acceleration and increase the velocity higher than the average required velocity. The average velocity for turning off the motor was selected by testing. For the final result the average velocity and the velocity at the end of the lap should both be higher or equal than  $7.5 \text{ m/s}$ . The velocity at the end of the lap should also be  $7.5 \text{ m/s}$ , since only lap is simulated. For lap two to nine to be similar the starting and finishing velocity should be the same, because the end velocity of the previous lap is the begin velocity of the next lap. The constants used in the simulation can be found in Table 8.1. The results from the simulation can be found in Table 8.2. The final column shows the velocity for which the motor is turned off. Since the second strategy does not have a turning off velocity, it does not contain a value. In the simulation the time interval for every calculation was  $0.1 \text{ s}$ . There is no strategy involving brakes, because brakes are only causing more energy losses, hence decrease the vehicle efficiency.

Figure 8.2: Track subdivided in sections, corresponding to appendix E



From strategy 3, the energy lost and the total drag is plotted in figure 8.3 and 8.4.

Table 8.2: Results from the simulation

Strategy	$E_{total}[J]$	$s[m]$	$t[s]$	$\bar{v}[m/s]$	$v_{finish}[m/s]$	$\eta[km/kWh]$	$v_{max}[m/s]$
1	2962	1617	218	7.41	7.33	1966	7.5
2	4215	1617	188	8.58	8.57	1381	—
3	2759	1617	215	7.50	7.50	2110	7.5
4	2852	1617	212	7.64	7.53	2041	7.7
5	2854	1617	212	7.64	7.53	2040	7.7
6	2838	1617	214	7.55	7.60	2051	7.6
7	2855	1617	211	7.65	7.53	2039	7.7
8	2823	1618	214	7.55	7.57	2063	7.6

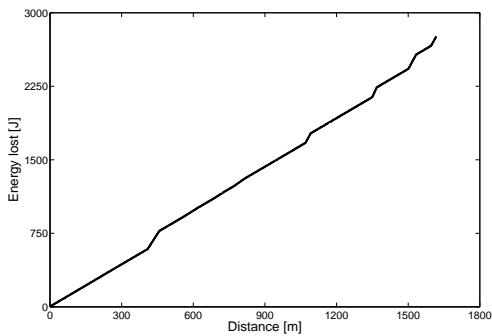


Figure 8.3: Energy lost during a lap

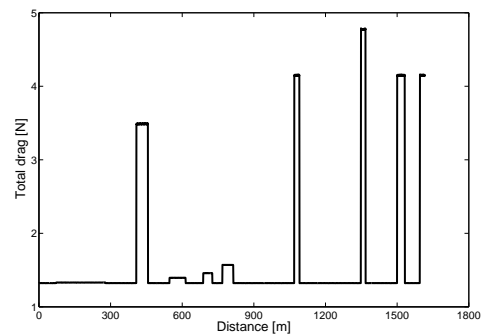


Figure 8.4: Drag forces during a lap

## 8.4 Verification

After the flow chart for the simulation is transformed into a design program, the program has to be verified. Since the program consists of separate units, each can be verified independently. When every unit is verified, a system test is conducted. The system test should make sure that each unit is connected to another correctly. The units to be checked are the following:

- calculation of drag forces;

- determination of propulsive force;
- calculation of dynamic values;
- computation of energy efficiency.

The input values for verification can be found in Table 8.1. The only differences are that for the verification a mass of the vehicle of 29 kg was used and that the velocity used is 7.5 m/s, just for verification of the units.

### 8.4.1 Drag Forces

As already described in Section 8.1, the drag forces acting on the vehicle comprises of the aerodynamic-, rolling- and cornering drag. Each is defined differently, and is therefore verified separately. Note that the inclination angle is neglected in the simplified track model assumption, hence slope drag is neglected here as well. To verify each component, a calculation of the drag is performed both analytically and numerically using the same input values. It is expected that no discrepancies arise, since the equations used are similar.

The aerodynamic drag can be calculated analytically using Equation 8.1. Filling in the input values results in:

$$F_a = C_D \cdot \frac{1}{2} \rho \cdot v_{air}^2 \cdot A_f = 0.075 \cdot \frac{1}{2} \cdot 1.225 \cdot 7.5^2 \cdot 0.285 = 0.74 \text{ [N]}$$

For the rolling drag, Equation 8.2 is used. The inclination is assumed to be 5°.

$$F_{r\parallel} = C_r \cdot m \cdot g \cdot \cos \alpha = 0.00081 \cdot 79 \cdot 9.81 \cdot \cos 5^\circ = 6.25 \text{ [N]}$$

The slope resistance then can be calculated using Equation 8.3.

$$F_{r\perp} = m \cdot g \cdot \sin \alpha = 79 \cdot 9.81 \cdot \sin 5^\circ = 67.5 \text{ [N]}$$

The total drag force can be calculated using Equations 8.4 and 8.5. For the verification, a radius of 30 m is assumed.

$$F_y = m \frac{v^2}{r} = 79 \cdot \frac{7.5^2}{30} = 148.1 \text{ [N]}$$

$$F_t = \left| \vec{F}_y \right| \sin \left( \frac{\left| \vec{F}_y \right|}{C_\alpha} \right) = 148.1 \cdot \sin \left( \frac{148.1}{13751} \right) = 1.60 \text{ [N]}$$

The output of the single units of the simulation can be found in Table 8.3. Since the same equations are used, both results are equal as expected. However, it is verified that every single unit is working properly.

Table 8.3: Analytical and numerical results for drag forces

Parameter	Analytical result [N]	Numerical result [N]
$F_a$	0.74	0.74
$F_{r\parallel}$	6.25	6.25
$F_{r\perp}$	67.50	67.50
$F_t$	1.60	1.60

### 8.4.2 Propulsive Force

The calculation of the propulsive force in the analytical model is done using Equation 8.6. For the verification of this single unit, it is assumed that all drag forces together are 4.00 *N*. This results for the analytical model in an equal propulsive force of 4.00 *N*.

Whereas discrepancies for the drag forces acting on the vehicle do not exist between the analytical and numerical model, it was expected that these do arise for the propulsive force. This is because in the numerical model the motor data from Appendix D are included. Comparison is shown in Table 8.4. From this can be concluded that the propulsive force unit is verified.

Table 8.4: Analytical and numerical results for the propulsive force

Parameter	Analytical result [ <i>N</i> ]	Numerical result [ <i>N</i> ]
$F_p$	4.00	4.08

### 8.4.3 Lost Energy

Besides the drag- and propulsive forces, the energy lost by the vehicle on a certain track segment can be verified. The track segment used for comparison is the first long corner on the track, as can be seen in Appendix E. This time, for the analytical model, the efficiency of the motor was checked with the motor data. Again, verification is achieved by comparison of analytically and numerically obtained results. These are presented in Table 8.5. The difference can be explained by the fact that the velocity stays constant in the analytical model. In the numerical model, the velocity changes by small steps due to the fact that the propulsion force is not always equal to the total drag force.

Table 8.5: Analytical and numerical results for the lost energy

Parameter	Analytical result [ <i>J</i> ]	Numerical result [ <i>J</i> ]
$E_{lost}$	342.20	356.50

### 8.4.4 System Test

Now that the program units are verified, the overall system should be checked. This is done by calculating the vehicle efficiency. Again, these are determined both analytically and numerically. In the analytical model, Equation 8.7 is used. This equation involves an integral over the entire track. Although it is known that the propulsive force is dependent on the location on the track, a definition of their relation remains unclear. As a result, the analytical model was simplified further by the simplified track assumption. Now, a discrete number of track segments is considered, each with well defined characteristics, hence Equation 8.7 changes.

$$E_{lost} = F_p \cdot \eta_{motor} \cdot \Delta s \quad (8.9)$$

Together with the constant velocity assumption in the analytical model, the propulsive force results to be constant over each track segment. Consequently, a comparison can be made between the (simplified) analytical and the numerical model in Table 8.6.

Table 8.6: Analytical and numerical results for the energy efficiency

Parameter	Analytical result [ <i>km/kWh</i> ]	Numerical result [ <i>km/kWh</i> ]
$\eta$	1828	1759

The difference between the analytical- and the numerical results for the energy efficiency of the vehicle is only 3.8 %. This difference is small enough to state that the simulation tool is verified. The small discrepancy is the result from dividing the track into discrete segments.

## 8.5 Validation Plan

For the validation of the driving strategy, the simulation should be checked with the data obtained in the real event. Since, the model is very much simplified and a lot of assumptions were made, there will probably be a significant difference between the results from the simulation and the real results. Also, in the real event a lot of vehicles are on the track at the same time and the pilot has to overtake, or is overtaken by, several other participants, which will have a negative effect on the efficiency. Moreover, the pilot is steering, so the line chosen at one lap will not be exactly the same as another.

## 8.6 Sensitivity Analysis

Since every subsystem is affecting the performance of the vehicle. The driving strategy is also influenced by every subsystem. A good overview of the effects of three major design parameters: the mass, the rolling drag coefficient and the aerodynamic drag index is shown in Figures 8.5 till 8.7. These figures show the increase or decrease of the efficiency when changing the design parameter. For the sensitivity analysis the constants from Table 8.7 were used.

Table 8.7: Constants used in the simulation

Parameter	Value	Unit
$A_f$	0.3	$m^2$
$C_D$	0.1	–
$C_r$	0.00081	–
$C_\alpha$	13751	–
$m$	80	$kg$
$v_0$	7.5	$m/s$
$\rho$	1.225	$kg/m^3$
$dt$	0.1	$s$
<i>Strategy</i>	3	–

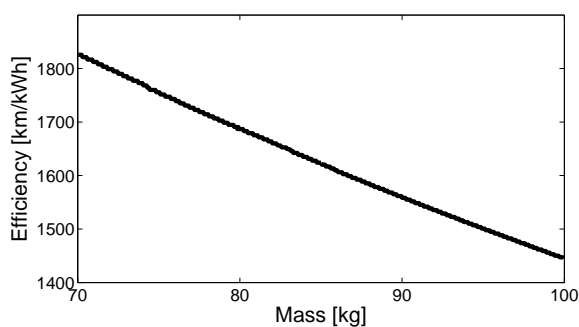


Figure 8.5: Sensitivity analysis for the mass

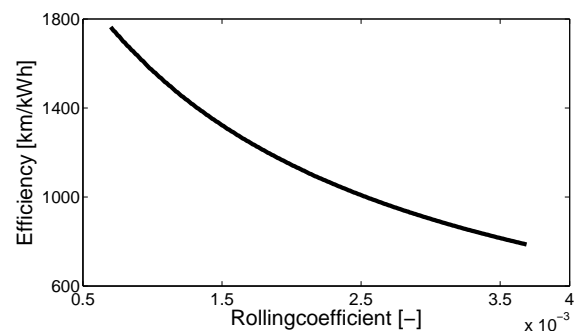


Figure 8.6: Sensitivity analysis for the rolling drag coefficient

Figure 8.5 shows the influence of the mass on the efficiency. From the figure, it can be concluded that the efficiency decreases linearly with respect to the mass. Figure 8.6 shows the effect of changing the rolling drag coefficient on the total efficiency. Decreasing the rolling drag coefficient would increase the efficiency of the vehicle a lot. However, with the Michelin tire for the prototype class cars the rolling drag coefficient of 0.00081 is already really low. Finally, in Figure 8.7 the effect of the aerodynamic drag index is shown. For this sensitivity analysis the aerodynamic drag index ( $A_f \cdot C_D$ ) was chosen and not the frontal area or aerodynamic drag coefficient, because both parameters are linked together. It is hard to change one of the parameters without changing the other one. From the figure, it can be concluded

that the aerodynamic drag coefficient has a large effect on the vehicle efficiency.

Next to these three important parameters, also other parameters affect the driving strategy. Other design parameters that also affect the driving strategy a lot, are for example the specifications of the motor, the battery and solar panels. The influence of these parameters are not further explained, since the main focus of this report is on mass, rolling drag and aerodynamic drag.

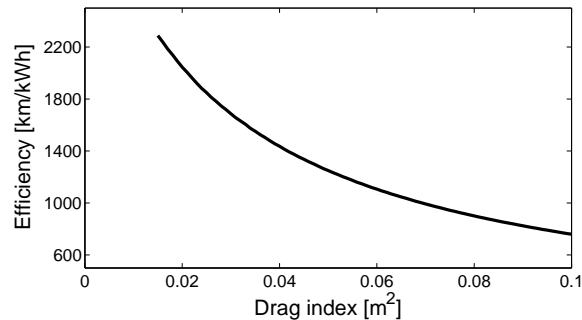


Figure 8.7: Sensitivity analysis for the aerodynamic drag index

## 8.7 Operation and Logistic Concept Description

In this section the focus is set on procedures during the Shell Eco-marathon. The general operational steps are shown in Figure 8.8. First, the vehicle has to be transported from its garage to the paddocks of the event. The team gathers and prepares the vehicle and the pilot for the race. Next is the technical inspection, which is done by the organization of the Shell Eco-marathon. In order to optimize the performance of the vehicle further, it should be transported to the track for a test run. As long as there is time available, this process is repeated such that the vehicle is ready to race without any flaws. After the race, the vehicle is transported back to the garage. The steps vehicle transportation (V.T.), team organization (T.O.), race preparation (P.) and race (R.) are explained in more detail below.

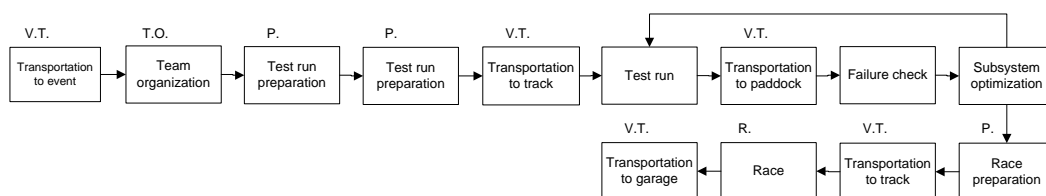


Figure 8.8: Flow diagram of the main steps during the operation of the Eco-runner for a race event

### Team Organization (T.O.)

As can be seen in Figure 8.9, the Eco-Runner Team starts with assigning team members to particular subsystems. Furthermore, the equipment needed during the event has to be transferred to the paddock such that the team members have all the equipment required to modify the vehicle for the race. Lastly, the technical documentation of the Eco-Runner vehicle has to be handed in to the organization before starting the race.

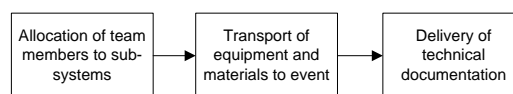


Figure 8.9: Flow diagram of the steps for the organisation of the Eco-Runner team

## Vehicle Transportation (V.T.)

During the event, the vehicle will have to be transferred from the garage to the paddock and to the track itself. In order to protect the vehicle it is carefully placed onto a rolling carriage. It may also be covered with a plastic to protect the vehicle from rain. When the destination is reached, the vehicle should be carefully placed back on the ground. This process is shown in Figure 8.10.

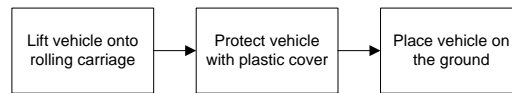


Figure 8.10: Flow diagram of the steps for the transportation of the Eco-Runner

## Race Preparation (P.)

An important step during the race-event is the race preparation. This is shown in Figure 8.11. Every subsystem is checked and inspected if it is installed properly onto the vehicle and it is controlled that everything works correctly. Also the pilot must be prepared for the race. He or she must be informed about the racing strategy and track conditions. The team must ensure that the pilot can race safely with the vehicle. Before Eco-Runner can compete in the race, a technical inspection is performed by the Shell Eco-marathon organization. To check if the vehicle is designed within the rules.

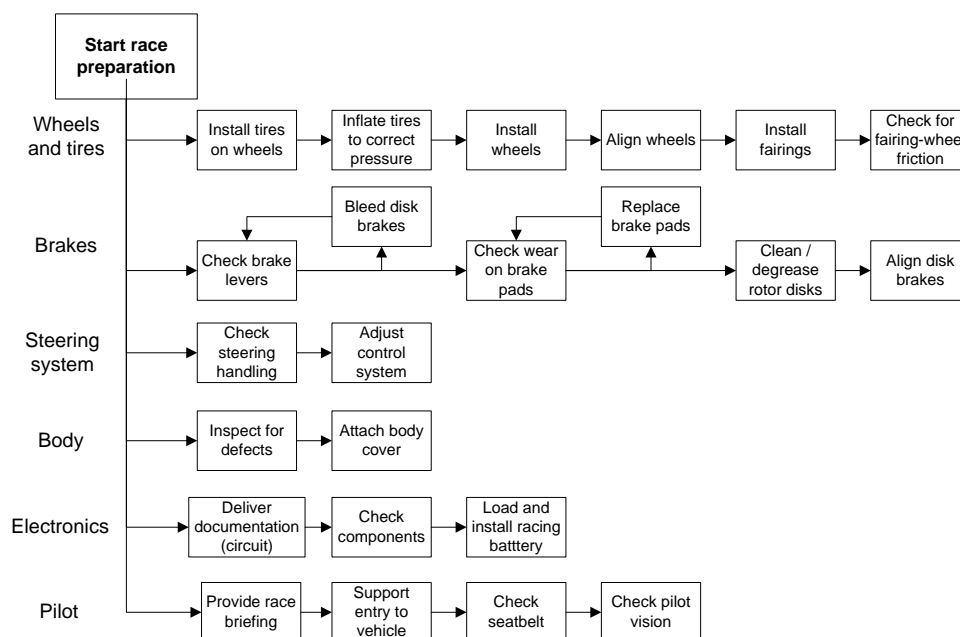


Figure 8.11: Flow diagram of the main steps for the preparation of the Shell Eco-marathon race in the paddocks

## Race (R.)

During the race, communication is a crucial aspect. One central command post has to be set up. This unit communicates with team members positioned around the track to have the current track conditions and monitor traffic. The driving strategy is updated from the command post as well. This is then communicated to the pilot who also gives feedback about the race to this unit. The communication flow is described in more detail in Section 7.2. The process of communication during the race is shown in Figure 8.12.

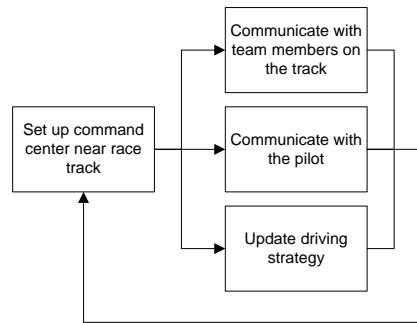


Figure 8.12: Flow diagram of the main steps during the Shell Eco-marathon race for the Eco-Runner Team

## 8.8 Conclusion and Recommendations

This chapter discussed the development of a simulation tool for the driving strategy for the Shell Eco-marathon. The simulation model was created using simplifying conditions, based on an analytical energy model. This model was then used again to verify the computer program.

It can be concluded that the best strategy for the race is strategy 3, use a feedback servo mechanism around  $7.5 \text{ m/s}$  while using the motor at its most efficient condition. This particular strategy will result in an energy efficiency of  $2110 \text{ km/kWh}$ . It must however be noted that this efficiency is based on one standard lap with a start- and end velocity of  $7.5 \text{ m/s}$  minimally. This implies that the acceleration to cruising speed, which is expected to cost most energy is neglected. The last lap is likely to cost less energy than other laps, as the end velocity of the lap is not required to be  $7.5 \text{ m/s}$ . Besides that, assumptions like the simplified track and the unicycle model significantly increases the efficiency of the vehicle. Finally, a pilot is incapable of following the strategy well enough to achieve the simulated efficiency. Causes may be other participants, not steering according to the perfect line or even the influence of wind on the track. Currently, it remains very hard to quantify the difference between the real and the simulated ideal vehicle efficiency.

Since the simulation program is a simplified model, a lot of improvements can be made. One improvement is the addition of a wind parameter in the model. Wind influences the airspeed around the vehicle, hence it affects the aerodynamic drag. Although a constant wind vector is not too complicated to add to the model, one might argue its usefulness. Since Ahoy is located in the city of Rotterdam, even constant wind is disturbed by buildings, causing the magnitude and direction to be very unpredictable. Another improvement to the model can be made by testing the motor more extensively. Currently, the motor is tested only for certain velocities. When this spectrum is enlarged, more strategies can be considered by the simulation program. More obvious improvements to the model can be made by using a more detailed track model or by assuming tricycle behavior for the vehicle. A more detailed track model includes slope drag, due to inclination angles on the track. Moreover, turn radii are not constant during a turn, as a turn is not perfectly circular in reality. It is expected that this improvement significantly increases the accuracy of the simulation. The tricycle model was already stated to be more accurate than the unicycle model, as it is much closer to reality in this case. Finally, the first and the final lap should also be investigated. Since a lot of energy is used in the first lap, this would lower the efficiency of the vehicle a lot. Choosing the right strategy for this first lap, will probably be quite beneficial. Although the model accuracy is increased by these modifications, it is expected that the programming effort and the computational time are increased substantially.

Another recommendation that can be made is to use a different method for the simulation. Now, an holistic approach is used where complete strategies are simulated. One may also choose to evaluate certain track elements separately. This approach could lead to an optimal strategy for driving certain parts of the track. An advantage of an holistic approach, as seen in this chapter, is that an energy

efficiency for the race can be computed, which is not possible when the other method is used. It is recommended to also investigate the track elements separately, which may lead to a more detailed racing strategy.

# 9 Vehicle Characteristics

In this section the design of the next Eco-Runner is presented. Before reaching a final design, however, some general features should still be defined. After that, the reliability, maintenance, availability and safety of the vehicle is estimated. Then, the internal- and external layout of the Eco-Runner is presented. Furthermore, a breakdown of cost and mass is shown for every subsystem of the vehicle. Finally, key figures for the vehicle are given.

## 9.1 Body Configuration Parameters

During the design of the body some parameters had to be set constant to optimize the design. First of all, the body and wheels were fitted around the driver which was based on the manikin in CATIA. The weight of the manikin was set to  $50\text{ kg}$  and its length to  $1.6\text{ m}$ . The hip width was set at  $0.35\text{ m}$ . Based on this model, the wheelbase was determined, since the placement of the driver has the most influence on the position of the center of gravity. This is due to the fact that the mass of the driver is the largest portion of the total vehicle mass.

### 9.1.1 Ground Clearance

According to [14] an airfoil shaped vehicle has the best aerodynamic characteristics for a ground clearance which is between 0.1 and 0.2 times the width of the vehicle. Since the body has a width of about  $590\text{ mm}$ , the ground clearance is optimal between  $59\text{ mm}$  and  $118\text{ mm}$ . However, the suspension of the front wheels is also of great importance for the characteristics of the vehicle and it is also taken into account for the ground clearance. So during the design of the ground clearance, a trade-off was made between designing for a lighter design or an aerodynamic better design. After some calculations, it showed that it would be better to optimize the design for the suspension, instead of the ground clearance. Since the structure of the suspension can be reduced in size and mass this has a greater advantage than the aerodynamic advantage. After adjusting the height in CATIA, the ground clearance with respect to the suspension turned out to be  $150\text{ mm}$ .

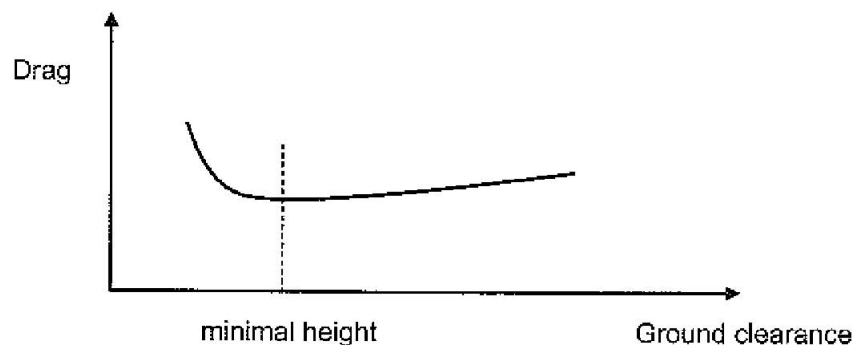


Figure 9.1: The drag of the vehicle versus the ground clearance. The drag bucket shows the minimum height of the vehicle from minimum drag [14]

### 9.1.2 Camber

The camber was determined by looking at the aerodynamic design, the structural design, the roll stability and the rolling friction coefficient. For the aerodynamic and structural design it is beneficial to design

the body such that the fairings are integrated in the body, since the frontal surface area and the weight will be lower. From Figure 9.2 it follows that the minimum rolling friction will be at zero camber. This is disadvantageous for the frontal surface area, since the fairings will be bigger. If there is no camber, then the fairings will stand on the side of the body which will disturb the smooth flow on the left and right side of the body. It will also decrease the stability of the vehicle. An increase in camber will increase the cornering performance of the body since the grip is increased during cornering. The camber was optimized such that the dimensions of the body could be minimal, and the length of the fairings could be as small as possible. The maximum camber was set by the space required for the driver and the track width. In the end, the best option for the camber with the chosen airfoils for the body and the fairings turned out to be an angle of  $6^\circ$ .

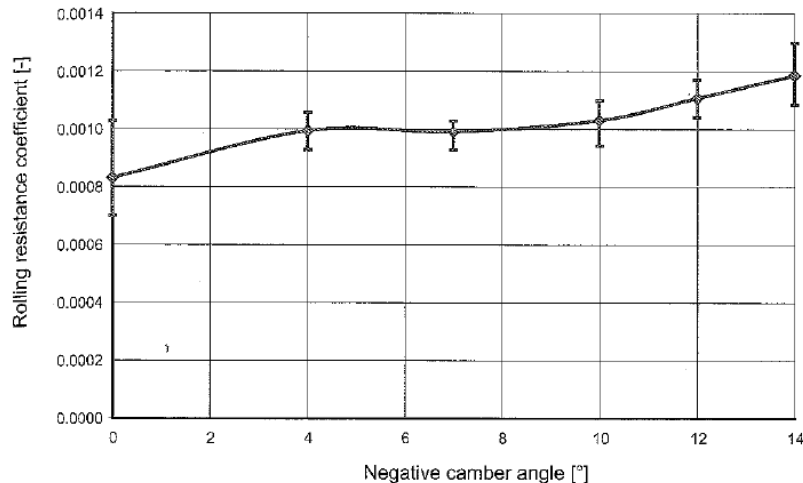


Figure 9.2: Effect of camber on rolling resistance coefficient [10]

### 9.1.3 Wheelbase

The wheelbase was based on the space required for the driver and the position of the center of gravity, since the center of gravity should be within the wheelbase to have a stable configuration. Also, the wheelbase influences the aerodynamics of the vehicle, since the larger the wheelbase, the larger the yaw angle for the rear wheel steering needs to be. After optimizing the wheelbase, the length turned out to be  $1.2\text{ m}$ . For this wheelbase, the rear wheel needs a deflection angle of  $12^\circ$  to be able to make a turn with a radius of  $6\text{ m}$ , which is required by the Shell Eco-marathon rules.

### 9.1.4 Track Width

The track width is minimal in order to minimize the frontal surface area. Also, the track width was already set at  $500\text{ mm}$  during the preliminary design.

### 9.1.5 Position of the Wheels

The wheels are positioned such that the front wheels are in front of the center of gravity and still as far to the rear wheel as possible. In this way, the flow is kept laminar over the body as long as possible. Obviously, the most rear position of the rear wheel is determined by the body size. As a result, the front wheels center lines will be  $1.2\text{ m}$  in front of the rear wheel's center line, as this is the wheelbase.

### 9.1.6 Position Fairings

The position of the fairings are determined by the position of the wheels. The fairings are positioned such that the center of the fairings coincides with the center of the wheels.

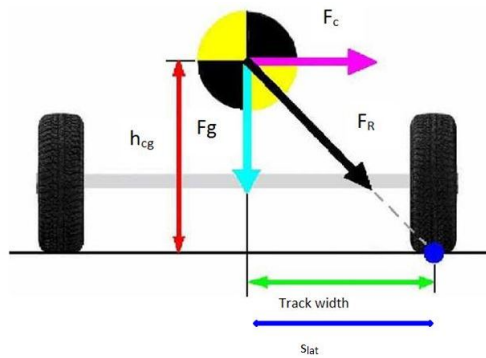


Figure 9.3: Front view with cornering forces [34]

### 9.1.7 Size Wheel Fairings

The size of the front fairings is determined such that the fairing fits as close as possible around the front wheels. The size of the rear wheel fairings is determined such that the rear wheel can still maximally deflect for steering. All these dimensions are kept as small as possible to keep the weight of the fairings low and to avoid the fairings scraping the ground when a bump is encountered.

### 9.1.8 Ground Clearance Fairings

The fairings should not scrape the ground when encountering a bump of  $15 \text{ mm}$ . Since the curvature of the bumps encountered will differ quite a lot a safety factor of two was taken into account. This results in a ground clearance of  $30 \text{ mm}$ .

## 9.2 Rollover Stability

The rollover stability needs to be determined to ensure that the vehicle does not roll over during cornering. By looking at Figure 9.3, the roll over stability was determined.

The centripetal acceleration was calculated by assuming a total vehicle mass of  $80 \text{ kg}$ , a minimum expected turning radius of  $18 \text{ m}$  according to the driving strategy and a maximum velocity of  $8 \text{ m/s}^2$ . This turn radius is based on the track data presented in Appendix E.

$$F_c = \frac{m \cdot v^2}{r} = \frac{80 \cdot 8^2}{18} = 284.5 \text{ [N]} \quad (9.1)$$

The gravitational force:

$$F_g = m \cdot g = 80 \cdot 9.81 = 784.8 \text{ [N]} \quad (9.2)$$

The centripetal acceleration:

$$a_c = \frac{F_c}{m} = \frac{284.5}{80} = 3.6 \text{ [m/s}^2\text{]} \quad (9.3)$$

The ratio of centripetal acceleration over gravitational acceleration,  $g_{\text{force}}$ , during cornering is:

$$g_{\text{force}} = \frac{a_c}{g} = \frac{3.6}{9.81} = 0.37 \text{ [-]} \quad (9.4)$$

Angle of resultant force with respect to the vertical plane:

$$\theta = \tan^{-1} \left( \frac{F_c}{F_g} \right) = \tan^{-1} \left( \frac{284.5}{784.8} \right) \approx 20^\circ \quad (9.5)$$

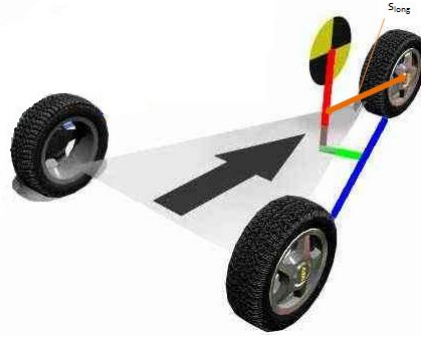


Figure 9.4: The line going from the front wheel to the rear wheel is the axis of rotation in case the vehicle rolls over. The line going from the center of gravity to the axis of rotation is the resultant  $s_{lat}$ . [34]

The distance from the center plane to the position where the resultant force will intersect with the ground ( $s_{lat}$  see Figure 9.2):

$$\tan(20^\circ) \cdot h_{cg} = s_{lat} \quad (9.6)$$

The distance from the contact point to the rear wheel contact point with the ground to the center of gravity is the resultant ( $s_{long}$  see Figure 9.4) .

$$\frac{s_{lat}}{\tan(12^\circ)} = s_{long} \quad (9.7)$$

The vehicle is stable when:

$$s_{long} < c_{glong} \quad (9.8)$$

$$s_{lat} < c_{glat} \quad (9.9)$$

After measuring the vehicle with the driver in CATIA, the center of gravity is found. The center of gravity in the lateral direction is almost zero, since the rear suspension is the only mass which is not symmetrical. The center of gravity with respect to the ground is about 295 mm from the ground and 560 mm in front of the contact point of the rear wheel with the ground. The  $s_{lat}$  is 107 mm.  $s_{long}$  is 514 mm from the rear wheel contact point in longitudinal direction. From Equations 9.8 and 9.9 it can be seen that the total vehicle will not roll over during cornering. The roll over stability is calculated for all the major parts of the vehicle, like wheels, body, driver and motor. All the smaller subsystems are not used for these calculations, but they need to be kept in mind during the placement of all the smaller subsystems.

### 9.3 Braking Stability

Another stability which needs to be considered is the braking stability. When the center of gravity is too much in the front of the vehicle, the vehicle will tip over during braking. For the calculations, the position of the center of gravity from the roll over stability is used again. The braking force is obtained from the braking requirements. The braking requirements are based on the brake test of the Shell Eco-marathon for which the vehicle should be able to stand still on a slope of 11.3°. And from table 6.2 the braking force is obtained.

$$F_{slope} = m \cdot g \cdot \sin(\alpha) = 80 \cdot 9.81 \cdot \sin(11.3^\circ) = 154 [N] \quad (9.10)$$

$$F_g = m \cdot g \cdot \cos(\alpha) = 80 \cdot 9.81 \cdot \cos(11.3^\circ) = 770 [N] \quad (9.11)$$

$$F_{brake} = 384 [N] \quad (9.12)$$

By taking the moment around the center of rotation the braking stability can be obtained.

$$M_{center} = F_{slope} \cdot z_{wheel} - F_g \cdot x_{wheel} + F_{brake} \cdot r_{wheel} \quad (9.13)$$

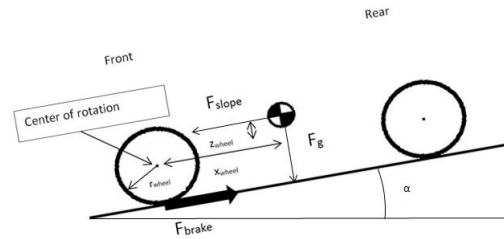


Figure 9.5: Braking stability

The vehicle is stable if:

$$M_{center} < 0 \quad (9.14)$$

Filling in the numbers:

$$M_{center} = (154 \cdot 0.045) - (770 \cdot 0.410) + (384 \cdot 0.250) = -213 \text{ [Nm]} \quad (9.15)$$

From this it is clear to see that the vehicle will not tip over during braking. Of course, this calculation is based on some simplified assumptions. This means that if the vehicle is not loaded correctly, the vehicle can become unstable.

## 9.4 RAMS Characteristics

RAMS is an acronym for Reliability, Availability, Maintainability and Safety. It is common to define these system characteristics as probabilities. Since the vehicle is not produced yet, it is very hard to quantify these probabilities at this moment. As a result, rough estimates and expectations of the RAMS characteristics are provided.

### 9.4.1 Reliability

The reliability of a system is defined as the probability that a system will perform in a satisfactory manner for a given period of time when used under specified operating conditions [35]. The total Eco-Runner vehicle including all its components can be described as several subsystems in a series and parallel network. When concerning only the main subsystems of the design, such as: body, suspension, steering, braking, wheels, motor, and battery, this system can be seen a series network. This means that if one of these subsystems fail, the entire vehicle fails and the mission will be aborted. The series network for reliability is presented in Figure 9.6. The reliability is primarily based on the failure rate, that is the number of failures over the total operating time. When the failure rate ( $\lambda$ ) of every system is obtained, the vehicle reliability can be determined from Equation 9.16.

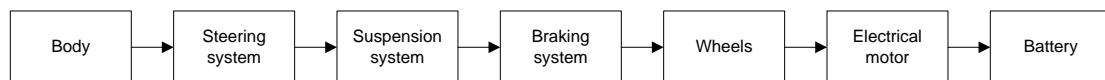


Figure 9.6: Reliability network for the Eco-Runner vehicle

$$\lambda = \sum_{i=1}^n \lambda_i \quad (9.16a)$$

$$R = e^{-\lambda t} \quad (9.16b)$$

Failure rates can only be obtained through careful testing of the respective subsystem. Although there is currently no test data available, an estimation of low accuracy can be made. It is expected that the total system has an average reliability. The body does not consist of many moving parts and therefore is

expected to be reliable. The wheels are expected to be a little less reliable, although this design is widely used, the tension in the spokes is critical and the rear wheel is a novel, immature concept. The steering, suspension, braking systems and the electrical motor are much less reliable as they do contain many moving parts. As a result, these subsystems are expected to have an average reliability. The battery is expected to have a low reliability, since from experience it is known that the failure rate of Lithium-ion batteries, when not charged and discharged properly, is quite high. During the race the battery is pushed to its maximum potential, that is why it is assumed to have a low reliability.

### **9.4.2 Availability**

The availability of a system is determined by the probability that a system is ready. Ready is defined as taking the vehicle and driving, directly. This is mostly dependent on the time required for maintenance and the likelihood that the system fails, making it impossible to directly drive the vehicle [35]. Like reliability and maintainability, it is very hard to quantify the availability probability at this stage in the design process. Since the final design is estimated to have an below average reliability and a high maintainability, the availability is expected to be below-average. Therefore concise testing is mandatory before mission is performed.

### **9.4.3 Maintainability**

The maintainability is seen as the ability of a system to be maintained. A high maintainability indicates that the system can be maintained easily and subsystems are well accessible, resulting in a low maintenance time. The inserts used to connect components to the body are small metal plates laminated into the body. Bolts are then used to attach the body to a particular component. Since bolts are used, components can easily be taken out of the body. This significantly increases the accessibility, hence decreases the maintenance time. The Eco-Runner vehicle can therefore be seen as a vehicle with a high maintainability.

### **9.4.4 Safety**

The safety of a system can be described as the probability that no harm is done to users and equipment. In the Eco-Runner design, safety is mostly guaranteed by following the Shell Eco-marathon 2013 rules carefully [9]. Many safety rules are required for the design. As the rules played an important role in the design process, it can already be stated that the safety of design will be quite high. A more accurate statement about the safety can be given when the vehicle is successfully produced and tested extensively. The most important function of the vehicle concerning safety is providing protection to the pilot, the other competitors and spectators.

## **9.5 Cost and Mass Breakdown**

In this section, an overview is presented for the estimated cost and mass breakdown for the Eco-Runner vehicle. First a cost- and then a mass breakdown is performed.

### **9.5.1 Cost Breakdown**

The cost breakdown for the subsystems discussed in the detailed design can be found in Table 9.1. Some subsystems were not considered during the detailed design. The assumption is made that these components (such as a fire extinguisher and a horn) can be taken out of the previous Eco-Runner vehicle. Therefore, the cost of these components is not taken into account. For some subsystems, no mold or extra off-the-shelf components are needed and the production of several subsystems will certainly be done by the Eco-Runner team self.

Table 9.1: Cost breakdown for monocoque body, wheels, suspension and electronic subsystems.

	Monocoque body	Wheels	Suspension	Electronics	Overall
Material [€]	1580	504	125	0	
Components [€]	0	860	0	5215	
Mold [€]	2000	6000	0	0	
Production [€]	450	0	0	0	
<b>Total [€]</b>	<b>4030</b>	<b>7364</b>	<b>125</b>	<b>5215</b>	<b>16680</b>

## 9.5.2 Mass Breakdown

An overview of a detailed mass breakdown for the total vehicle can be found in Table 9.2. A total vehicle mass of  $23.4 \text{ kg}$  is obtained by adding all the masses from every component together. Therefore, it can be concluded that the  $30 \text{ kg}$  mass budget requirement is met.

The masses for a sub-system are estimations based on calculations during the detailed design. The masses for subsystems that were not handled in the detailed design were taken from the previous Eco-Runner vehicle. The mass breakdown is also represented in a pie chart, shown in Figure 9.7. This pie chart shows that the body and the electronics have the largest contributions to the total vehicle mass.

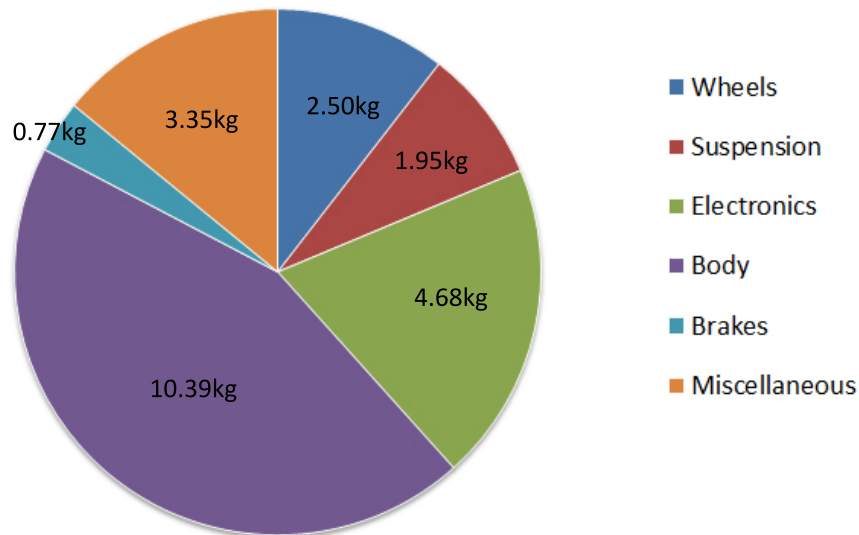


Figure 9.7: Pie chart of the vehicle mass breakdown

Table 9.2: Total mass breakdown for the Eco-Runner vehicle

Subsystem	Mass [kg]	Subsystem	Mass [kg]
<b>Body</b>		<b>Suspension</b>	
Total	<b>10.40</b>	Total	<b>1.95</b>
Windows	1.00	<b>Front suspension</b>	<b>0.33</b>
Monocoque	6.79	Axle	0.15
Inserts	0.60	Upper bracket	0.09
Coating	2.00	Lower bracket	0.07
		Inserts and bolts	0.03
<b>Wheels</b>		<b>Rear suspension</b>	
Total	<b>2.50</b>	Total	<b>1.62</b>
Front wheel (one)	0.80	Rod	0.27
Hub	0.06	Axle	0.38
Bearings	0.04	Rail	0.31
Rims	0.21	Bolts and nuts	0.04
Spokes	0.01	Bearing	0.02
Tire	0.40	Bracket	0.31
Glue and patches	0.05	Steering rod	0.20
valve	0.02	Springs & mounting	0.03
rear wheel	0.90	Push-pull attachment	0.06
Hub	0.30	<b>Electronics</b>	
Bearings	0.06	Total	<b>4.68</b>
Rims	0.21	Propulsion battery	0.27
Spokes	0.06	Motor	3.40
Tire	0.20	MPPT	0.75
Glue and patches	0.05	System controller	0.03
valve	0.02	Data logger	0.05
<b>Miscellaneous</b>		Solar Cells	0.14
Total	<b>3.15</b>	Accessory battery	0.04
Steering stick	0.35	Camera	0.10
Wheel covers (inside)	0.30	Display	0.15
Seat belt	1.00	Horn	0.40
Fire extinguisher	1.20	Cables	0.05
Mirrors	0.20	<b>Brakes</b>	
		total	<b>0.77</b>
Mounting parts	0.10	Brake set (incl. lever)	0.60
		Disks	0.17
<b>Total vehicle mass</b>	<b>23.4</b>		

## 9.6 Vehicle System Characteristics

In Table 9.3, all design choices of all subsystems are summarized. The key figures of the vehicle performance characteristics are given in Table 9.4. Finally, the body dimensions are displayed in Table 9.5.

Table 9.3: Total vehicle configuration

Vehicle system	Configuration
Wheel configuration	2-1 tadpole
Wheel placement	Combined inside and outside of the body, with fairings
Driver positioning	Driver laying down
Front and rear vision	Windows, internal mirrors and additional cameras
Body shape top view	Airfoil RU-21T- 00632D
Body shape side view	Airfoil BO-173T-00735D-047L
Body structure	Monocoque
Body materials	Toray T300 carbon fiber, Nomex honeycomb sandwich structure
Steering	Rear steering, push-pull cable
Front suspension	Embedded, thru axle
Front suspension material	Aluminum 7075
Rear suspension	Bracket and rails, 4 rods
Rear suspension material	Aluminum 7075, carbon fiber
Braking	Disk, both sides forced, front and rear
Automobile lay-out	Rear wheel driven
Wheels	Spoked
Wheels materials	Toray T300 carbon fiber, HexTow <sup>TM</sup> IM 6 carbon fiber
Tires	Michelin 45-75-R16 tubeless
Motor	Brushless in-wheel Mitsuba M00512-IV
Battery	6 Panasonic NCR-18650A
Solar cells	Emcore ZTJ Photovoltaic Cell
Energy storage	Ultracapacitor
Control system	Microcontroller Arduino Uno R3

Table 9.4: Vehicle performance characteristics

Performance characteristic	Key figures	Unit
Energy efficiency $\eta$	2110	$km/kWh$
Total vehicle mass $m$	23.6	$kg$
Driving velocity $v$	7.5	$m/s$
Laminar flow region	90	%
Drag coefficient $C_D$	0.085	—
Rolling friction coefficient $C_r$	0.00081	—
Rolling drag	0.06	$N$
Motor efficiency	93	%
Solar power	33	$W$

## 9.7 Internal and External Lay-out

The external layout of the final design of the Eco-Runner vehicle is shown in Figure 9.8 and Figure 9.9. In Figure 9.11 it is shown how the driver is positioned within the vehicle. The internal lay-out of the vehicle can be seen in Figure 9.10. The batteries and electronics are attached to the bulkhead, near the rear

Table 9.5: Body dimensions

	Dimension	Unit
Body length	2.750	<i>m</i>
Body width	0.587	<i>m</i>
Wheelbase	1.200	<i>m</i>
Track width	0.500	<i>m</i>
Frontal area	0.285	<i>m</i> <sup>2</sup>
Minimum ground clearance	0.150	<i>m</i>

suspension, as shown in Figure 9.12. The electronics are located in the large box in the middle and the batteries are placed in the smaller boxes on the sides. Finally, an exploded view of the total vehicle and all the subsystems is given in Figure 9.13.

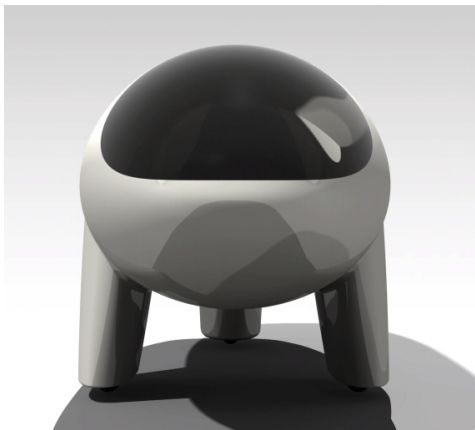


Figure 9.8: Front view

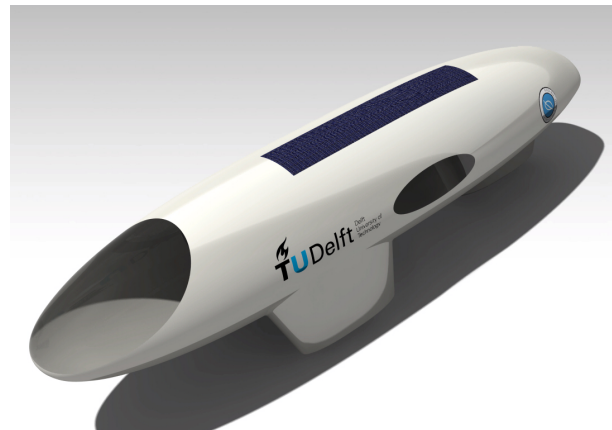


Figure 9.9: Isometric view

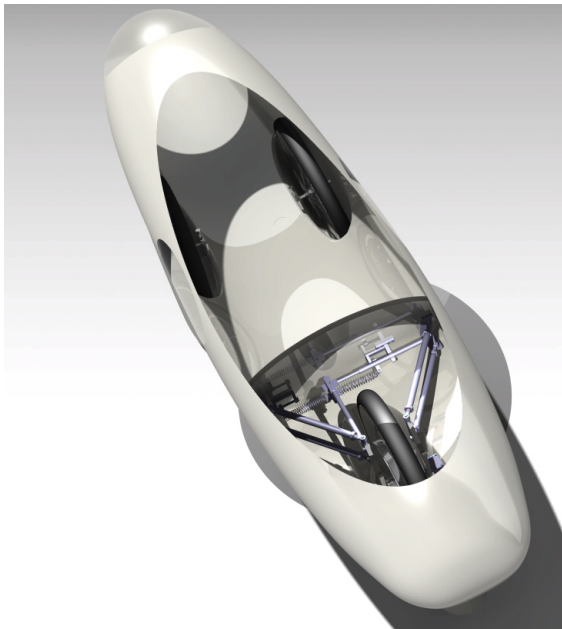


Figure 9.10: Internal lay-out

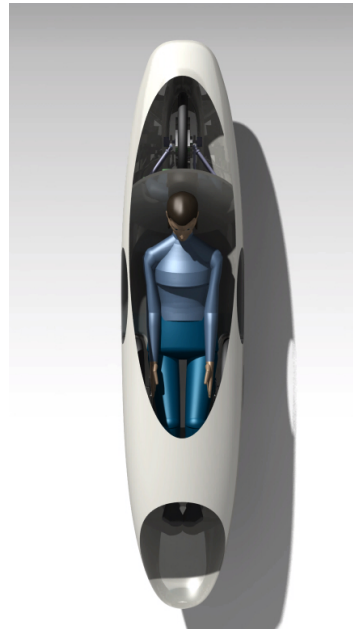


Figure 9.11: Top view

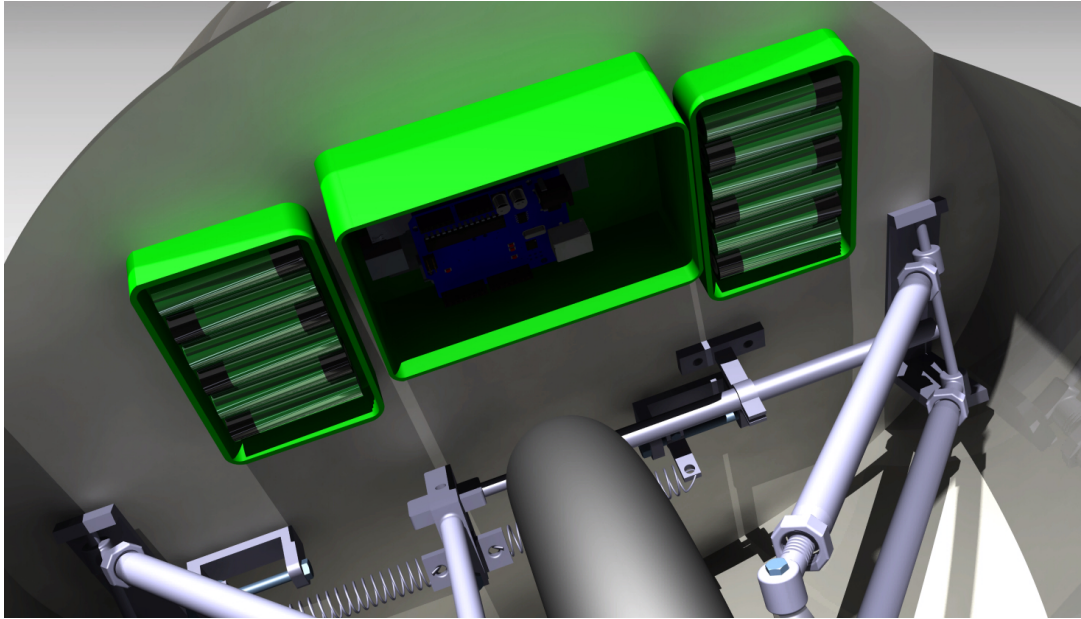


Figure 9.12: Internal view

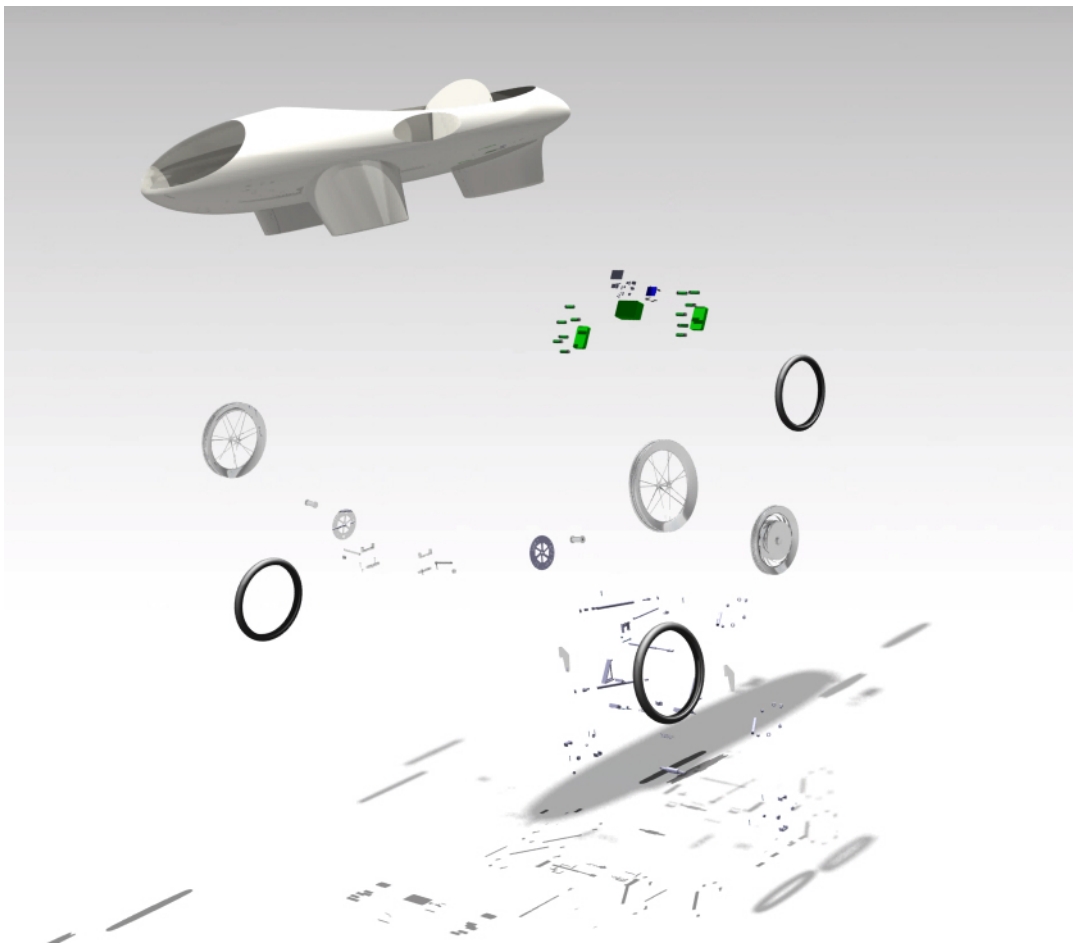


Figure 9.13: Exploded view of the Eco-Runner



# 10 Future Prospects of the Design

Now that the next Eco-Runner has been designed, plans have to be made for the future of the project. Since the goal of the DSE is to provide valuable information for the TU Delft Eco-Runner team of 2013/2014 and give them a head start, the next steps for the design are presented. First of all, a general development strategy for the design is shown. Then, a more specific manufacturing, integration, and assembly plan for the subsystems and the vehicle is given. Finally, a Gantt chart is provided, showing a proposed planning for the Eco-Runner project over the next year.

## 10.1 Project Development

This section presents the steps that should be undertaken when developing the Eco-Runner in the future. An effective development strategy is vital to the overall success of any project because it ensures that materials, equipment, and human resources will be available on time. The development strategy can be shown in a flow diagram, this is done in Figure 10.1. Eleven main steps must be completed before the actual manufacturing can start. Some of the steps are marked with an asterisk. The asterisk indicates a bottleneck. Bottlenecks are constraints and restrictions in the process which might appear during the development. A bottleneck can also occur if previous activities are delayed. It is really important to locate them beforehand, such that discontinuities in the development process are minimized.

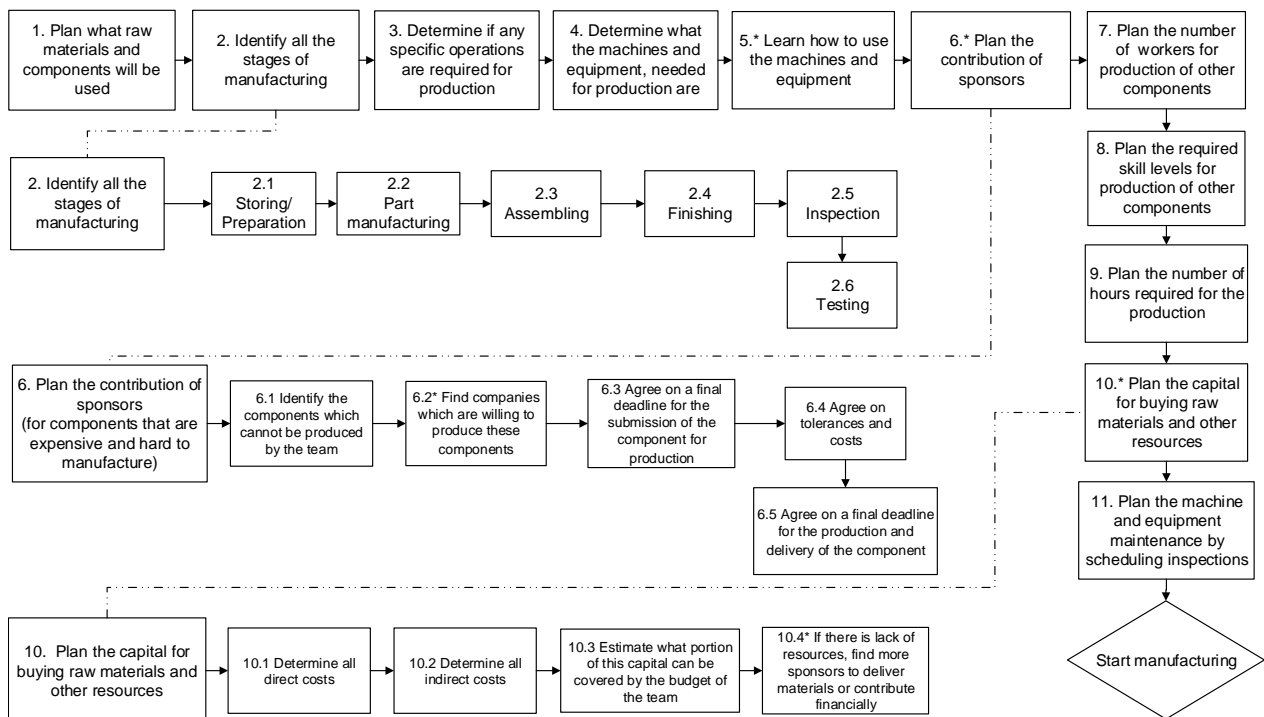


Figure 10.1: Functional flow diagram of the development strategy

The flow diagram shows that a bottleneck might arise at step 5, learning to use the machines and the equipment. As new people join the Eco-Runner team every year, new people have to be taught how to operate certain machines. This can be time consuming and lead to a low quality of the produced components. Another bottleneck may arise at step 6.2. Sponsors are hard to find, especially in current times considering the economic crisis. As a result, this step is identified as a bottleneck. The last

bottleneck is identified at step 10 in the development strategy. As step 10.4 states, a lack of resources requires more sponsoring. As mentioned before, sponsors are generally hard to find these days.

## 10.2 Manufacturing, Assembly and Integration Plan

To assemble the vehicle from its constituent parts, first all the subsystems need to be produced. In Figure 10.2, flow diagrams illustrate the general production activities required for each subsystem. Figure 10.3 shows the flow diagram for the assembly, the dashed lines indicate when the production of the subsystems should be finished and are required as input for the assembly.

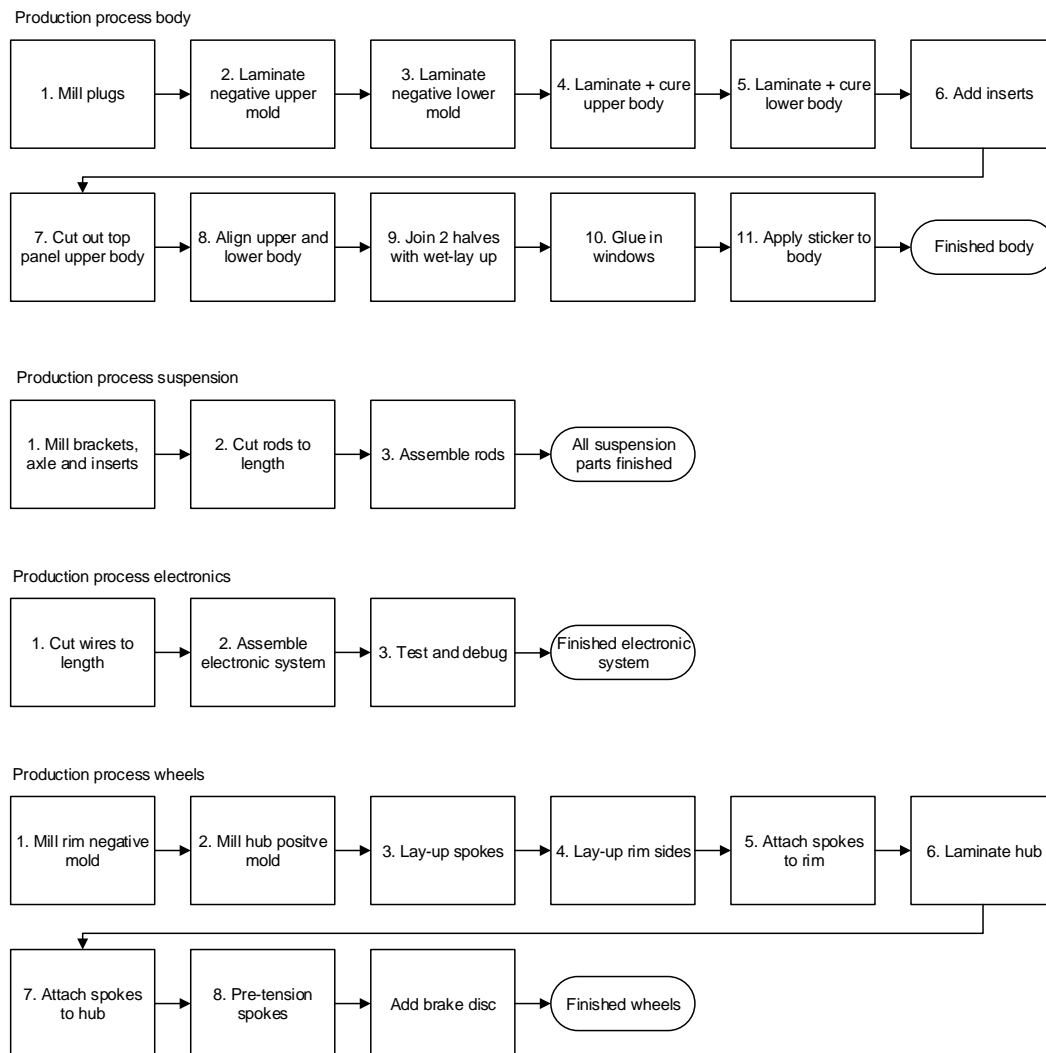


Figure 10.2: Flow diagram of the manufacturing process of the body, suspension, electronics and wheels

The production of the body is critical. It is a large part and the production is labor intensive, but it is also in essence a big bracket to which all the other parts need to be assembled. The assembly cannot start if the body is not finished. Other parts can be fitted to the body individually. The part that needs the most production time needs to be finished first. This should already be considered in the design phase. The design should be finished earlier or more human resources should be assigned to the production of the body.

Some remarks for the production processes of the subsystems follow. Milling of the plugs is most likely outsourced and if so, must be scheduled. The milling company might not be able to mill the plugs

at a desired moment in time. Ordering off-the-shelf parts should be scheduled and tracked to make sure the parts are in house for the assembly. As testing the electronic system is first assembled outside the car. Calibrating and debugging is easier because of higher accessibility and a controlled environment. The assembly of the electronic system can then start before the body is finished.

The production of the different systems can be done in parallel. However, some production processes take longer and are required earlier in the assembly. Note that the assembly can be done in one week, such that there is only a few days margin when every part should be finished for optimal efficiency.

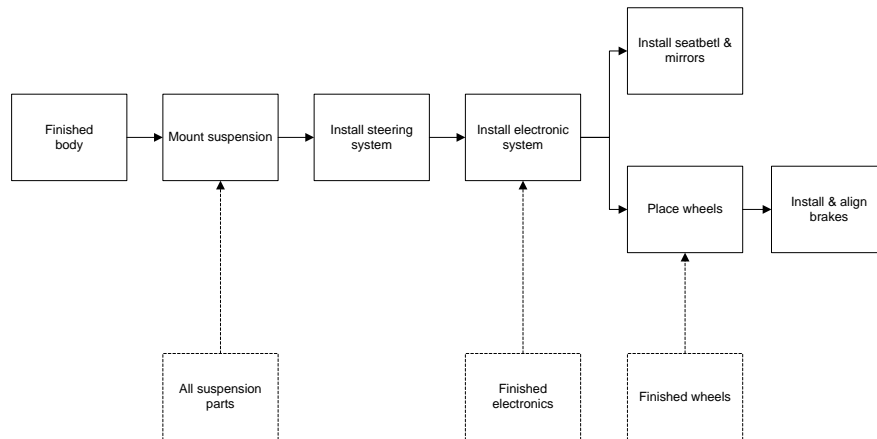


Figure 10.3: Flow diagram of the manufacturing process of the body, suspension, electronics and wheels

The assembly starts with mounting the suspension and steering system. This is done before the assembly of the electronic system as the drilling of some holes is required for the assembly and this might cause problems if the electronic system is already mounted. The electronic system is mounted next, because without the wheels and mirrors, more space is available for assembly. The brakes can only be aligned after the wheel with the brake brake is in place.

### 10.3 Project Gantt Chart

After this DSE, the story of the Eco-Runner continues. Since Eco-Runner is a D:Dreamteam, they will start over again in September with a new team and use the information from the performed DSE. Basically, the Eco-Runner team will perform the same design process as in the DSE more extensively. A design process will be the start, which will be continued by production and validation. In May, the Shell Eco-marathon will be the end of an intensive year for the Eco-Runner Team. The project Gantt chart can be seen in figures 10.4 and 10.5 where all the activities that will be done next year are summed up and placed on the timeline.

First, in the beginning of September, the team is organized. Tasks and responsibilities are assigned to the new team members. The goals and requirements for next year are set. Afterwards, a literature study will be performed. In this literature study, all information from previous years and other teams will be ready to get familiar with all aspects of the Shell Eco-marathon. In this phase, also the reports of this DSE will be analyzed and all useful information can be used. After this literature study, the team should come up with new concepts. The team can also combine good concepts from the previous years and optimize based on experience. Afterwards, the team will get as much feedback as possible on their concepts from old team members and the supervisors of the D:Dreamhall. After gathering all the information and feedback, trade-offs between different concepts will be made.

In the beginning of November, these subsystem concepts will be worked out in detail. This includes making CAD drawings and producing a mock up to check dimensions of integration of all subsystems. Strength calculations will be performed. Next, the decision has to be made if the parts will be produced

by the team or if it will be outsourced. Feedback will be needed for production from professionals, like DEMO on campus or other manufacturing companies. When the parts are produced by the team, the team should get familiar with the machining and production process.

In the beginning of February, it is time to start the production. For some parts, practice will be needed. Attention will be given to tolerances, since this is afterwards during the assembly. When the production is performed, validation test can be performed. These tests can include strength tests, wind tunnel experiments and a mock up to test the electronics. Afterwards, the assembly is done. Since problems can be found during assembly, a problem-solving approach is needed.

In the beginning of May, the car should be ready and the testing can start. Since driving strategy and driving experience can make a big difference on the race, the driver should make some test laps. Then the race will take place. After the race, all performed work of the past year should be documented for the next team. New team members should be found to ensure the future of the team.

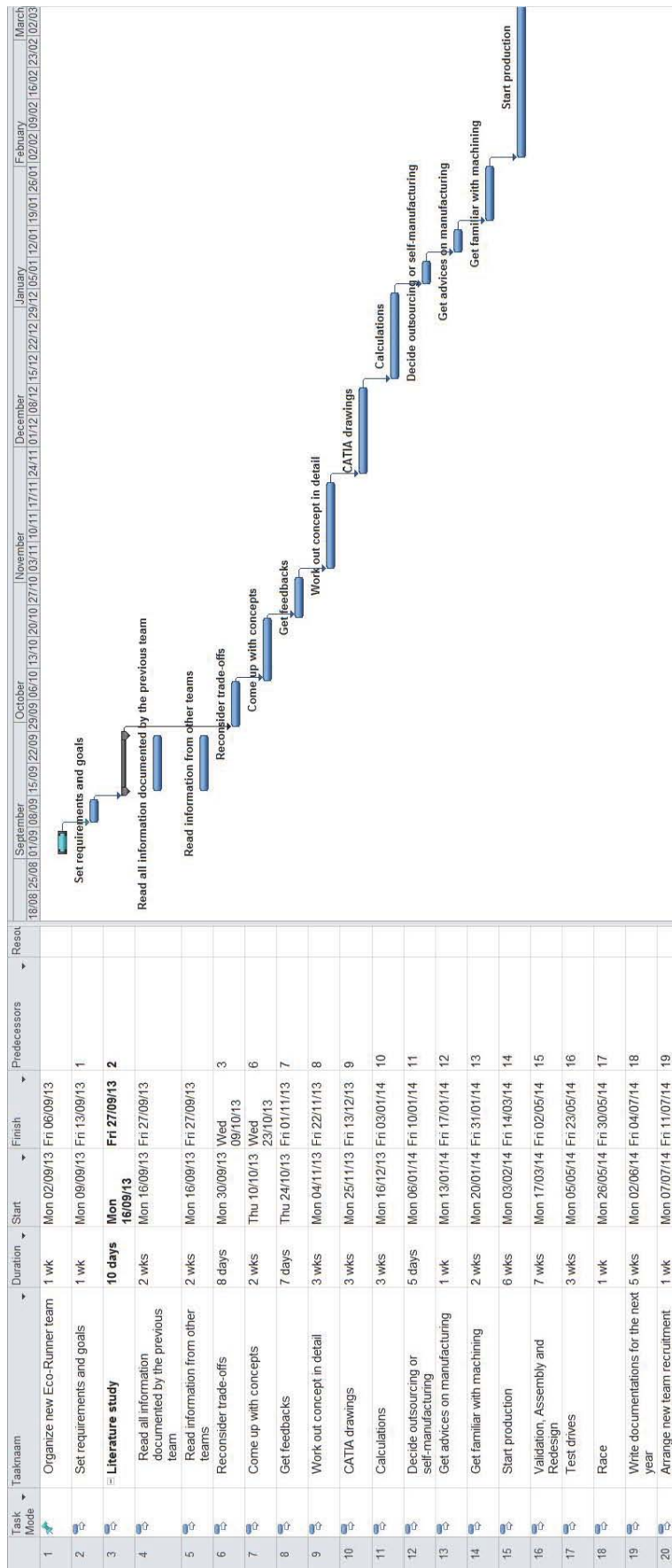


Figure 10.4: Post DSE Gantt chart part 1

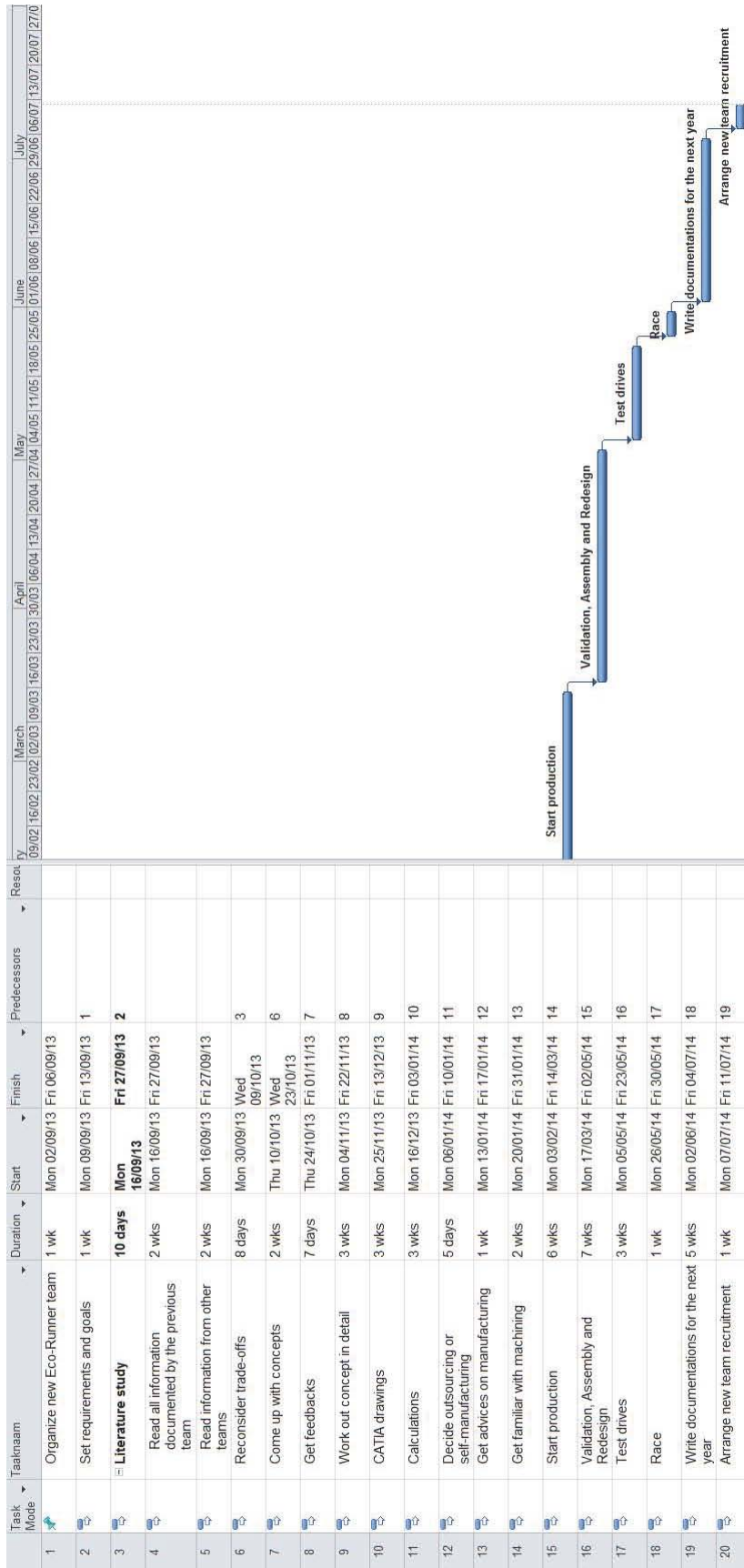


Figure 10.5: Post DSE Gantt chart part 2

# 11 Conclusion and Recommendations

This report is the final document in a series of documents about the design of the next Shell Eco-marathon vehicle from TU Delft. The vehicle is required to be capable of driving at least  $790 \text{ km}$  on only  $1 \text{ kWh}$  of energy. This report described the detailed design of the vehicle. The vehicle was broken down to five subsystems:

- body aerodynamics;
- body structure;
- suspension;
- wheels;
- electronic systems.

Besides these subsystems a simulation tool, aimed at determining the best driving strategy for the race was developed.

A detailed design for the aerodynamics of the body was achieved using computational fluid dynamics (VSAERO). Fairings are designed around the wheels to ensure a minimum aerodynamic drag. The structural aspects of the body were verified using finite element analysis (Abaqus), leading to a minimal body weight. The body consists of carbon fiber (Toray T300) and (Nomex) sandwich panels, and is produced through prepreg lay-up. The mold for the production of the body will exist out of an upper and a lower mold. The lower part again is separated into 3 parts to make the demolding a bit easier. When the prepreg lay-up is done the parts will go into an autoclave to cure the resin. Spoke wheels are used, with both the rim and the spokes made from carbon fiber. On the rim, a tubeless tires designed specifically for the Shell Eco-marathon (Michelin 45-85R16), causing minimal rolling friction, is used. Wheel components are produced through lay-up and assembled by using adhesives and curing.

The overall design proved to be a great improvement of the current Eco-Runner in terms of weight. The next Eco-Runner weighs  $45\%$  less than the current design. The significant weight reduction and the impressive aerodynamics lead to a design that well fulfills its energy efficiency requirement. The vehicle is estimated to be capable of driving at an energy efficiency of  $2110 \text{ km/kWh}$  in ideal conditions (no wind, dry road, etc.).

For the future, it is recommended to further optimize the aerodynamics. Mainly due to time limitations, the aerodynamics of the body were not fully optimized. Wind tunnel tests could be performed to validate the results obtained from CFD calculations. Moreover, the simulation model for the driving strategy can be further developed to estimate the vehicle efficiency more accurately. The structure of the body could still be optimized more by doing more research on the stress distributions in the body, such that the structure can be optimized to withstand these stresses. In general, it is highly recommended to further optimize the vehicle so that the energy efficiency of the design can be increased even further.



# Bibliography

- [1] "T300 Data sheet," <http://www.toraycfa.com/pdfs/T300DataSheet.pdf>, 2012.
- [2] Shercliff H., "Property Information, Maximum Service Temperature," [http://www-materials.eng.cam.ac.uk/mpsite/properties/non-IE/max\\_service\\_temp.html](http://www-materials.eng.cam.ac.uk/mpsite/properties/non-IE/max_service_temp.html), 2011.
- [3] Callister W.D., *Materials Science and Engineering*, John Wiley & Sons, Inc., 7th ed., 2007.
- [4] Panasonic Corporation of America, "NCR18650A Lithium Ion," <http://www.panasonic.com/industrial/includes/pdf/ACA4000CE254-NCR18650A.pdf>, 2011.
- [5] "ZTJ Photovoltaic Cell Datasheet," [http://www.emcore.com/wp-content/uploads/ZTJ\\_Datasheet.pdf](http://www.emcore.com/wp-content/uploads/ZTJ_Datasheet.pdf), 2012.
- [6] "Arduino Uno Datasheet," <http://arduino.cc/en/Main/arduinoBoardUno>, 2013.
- [7] "Raspberry Pi Model B Datasheet," <http://www.raspberrypi.org/faqs>, 2013.
- [8] SKF Group, "SKF Energy Efficient deep groove ball bearings," 2008.
- [9] Shell Eco-Marathon, "Official Rules 2013," 2013.
- [10] Santin J.J., Onder C.H., Bernard J., Isler D., Kobler P., Kolb F., Weidmann N., Guzzella L., "The world's most fuel efficient vehicle," vdf Hochschul verlag AG aan der ETH Zurich, 2007.
- [11] Bouquet T., van Egmond J., "AERODYNAMISCH ONTWERP ECO-RUNNER 3," Eco-Runner internal document.
- [12] Kumar, B., <http://www.answers.com/topic/transition-point>.
- [13] van der Heide A., et al, "Eco-Runner mid-term Report," TU Delft, Faculty of Aerospace Engineering, May 2013.
- [14] Tamai G., *The Leading edge*, Robert Bentley Publishers, 1999.
- [15] "HexWeb Honeycomb Sandwich Design Technology," [http://www.hexcel.com/Resources/DataSheets/Brochure-Data-Sheets/Honeycomb\\_Sandwich\\_Design\\_Technology.pdf](http://www.hexcel.com/Resources/DataSheets/Brochure-Data-Sheets/Honeycomb_Sandwich_Design_Technology.pdf), 2000.
- [16] Bunyawanichakul P., Castanie B., Barrau J., "Experimental and Numerical Analysis of Inserts in Sandwich Structures," Springer, 2005.
- [17] "Sandwich Panel Fasteners Design Manual," [http://www.shur-lok.com/product\\_dls/Design\\_Manual.pdf](http://www.shur-lok.com/product_dls/Design_Manual.pdf), 1996.
- [18] "Faserverbundwerkstoffe Composite Technology," <http://www.r-g.de/en/>, 2013.
- [19] Goel A., "Economics of Composite Material Manufacturing Equipment," Massachusetts Institute of Technology, Department of Mechanical Engineering, September 2000.
- [20] Elliott R., "Deflection of beams," <http://www.clag.org.uk/beam.html>, 2010.
- [21] Hibbeler R.C., *Mechanics of Materials*, Pearson Education Centre, 2008.
- [22] "Carbon Fibre Shop," <http://www.carbonfibreshop.co.uk/PBCPPlayer.asp?ID=1166515>, 2012.
- [23] Megson T.H.G., *Aircraft Structures for Engineering Students*, Elsevier Science and Technology, 2012.

- [24] "E-Shop for Shell Eco-marathon Asia," <http://www.semasiaeshop.com/partners.php>, 2013.
- [25] Future Publishing Limited, "Vectran keep Conti inflated," [http://autobus.cyclingnews.com/tech/?id=2005/features/conti\\_tech](http://autobus.cyclingnews.com/tech/?id=2005/features/conti_tech), 2005.
- [26] "Spoke Patterns," <http://www.astounding.org.uk/ian/wheel/patterns.html>, 2010.
- [27] Brandt J., *The Bicycle Wheel*, Avocet inc, 1993.
- [28] Ng J., "Finite Element Analysis of a Bicycle Wheel," Rensselaer Polytechnic Institute Hartford, Connecticut, 2012.
- [29] Bergsma O., *Process for thermoplastics and thermoset composites*, TU Delft, Production of Aerospace Systems (AE2207), 2013.
- [30] ROYMECH, "Factors of Safety," [www.roymech.co.uk/Useful\\_Tables/ARM/Safety\\_Factors.html](http://www.roymech.co.uk/Useful_Tables/ARM/Safety_Factors.html), 2008.
- [31] Kassapoglou C., "Fuselage Door Design," TU Delft, Structural Analysis and Design (AE2211), 2013.
- [32] Performance Composites Ltd, "MechDesign Properties of Carbon Fibre Composite Materials," [http://www.performance-composites.com/carbonfibre/mechanicalproperties\\_2.asp](http://www.performance-composites.com/carbonfibre/mechanicalproperties_2.asp), 2009.
- [33] Douzoglou A.L., "How it's Made!" <http://www.beyondaero.com/how-its-made/>, 2012.
- [34] Ethier P.M., "Simpel visual analysis of 3-Wheeler stability," <http://c11.qc.ca/Professeurs/Mecanique/ethierp/3-wheels/stabill1.htm>.
- [35] van Tooren M., "AE3S01 System Engineering and Technical Managment Techniques," TU Delft reader, 2006.

# A Visualization of the Aerodynamic Design Process

## Step 1

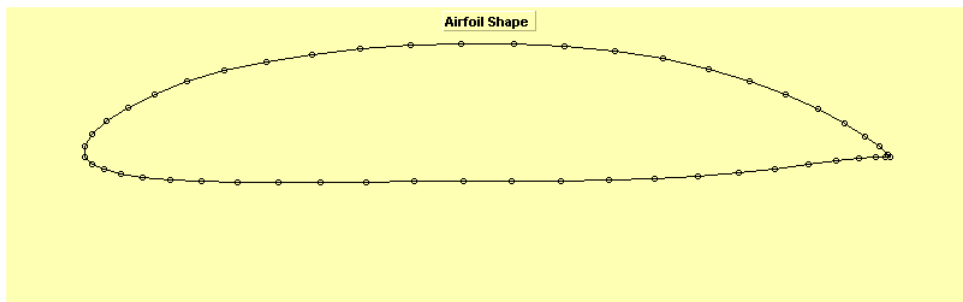


Figure A.1: Javafoil output

## Step 2

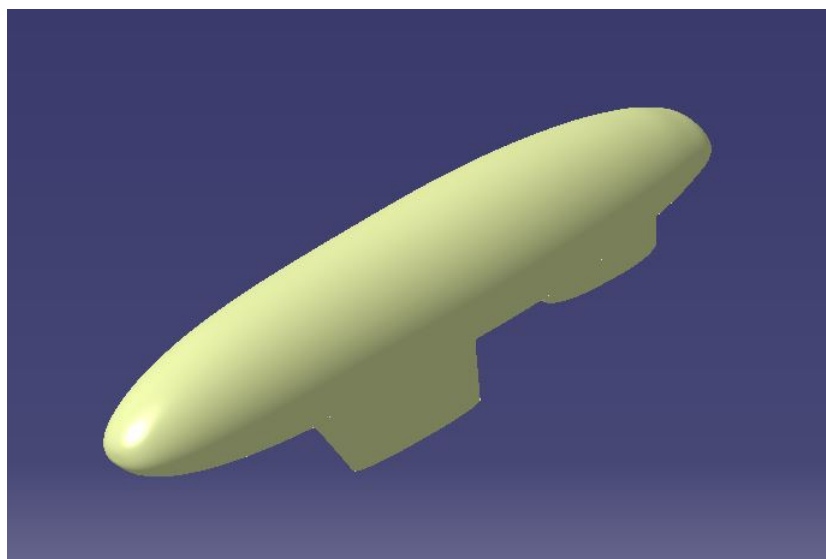


Figure A.2: CATIA output

### Step 3

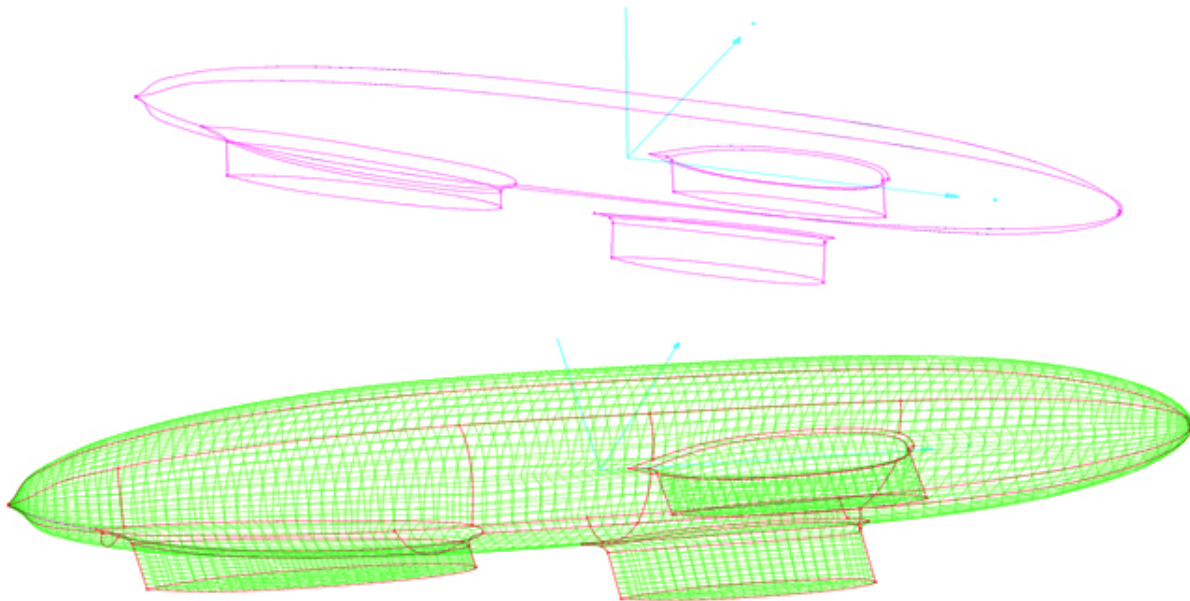


Figure A.3: Gridgen input and output

### Step 4

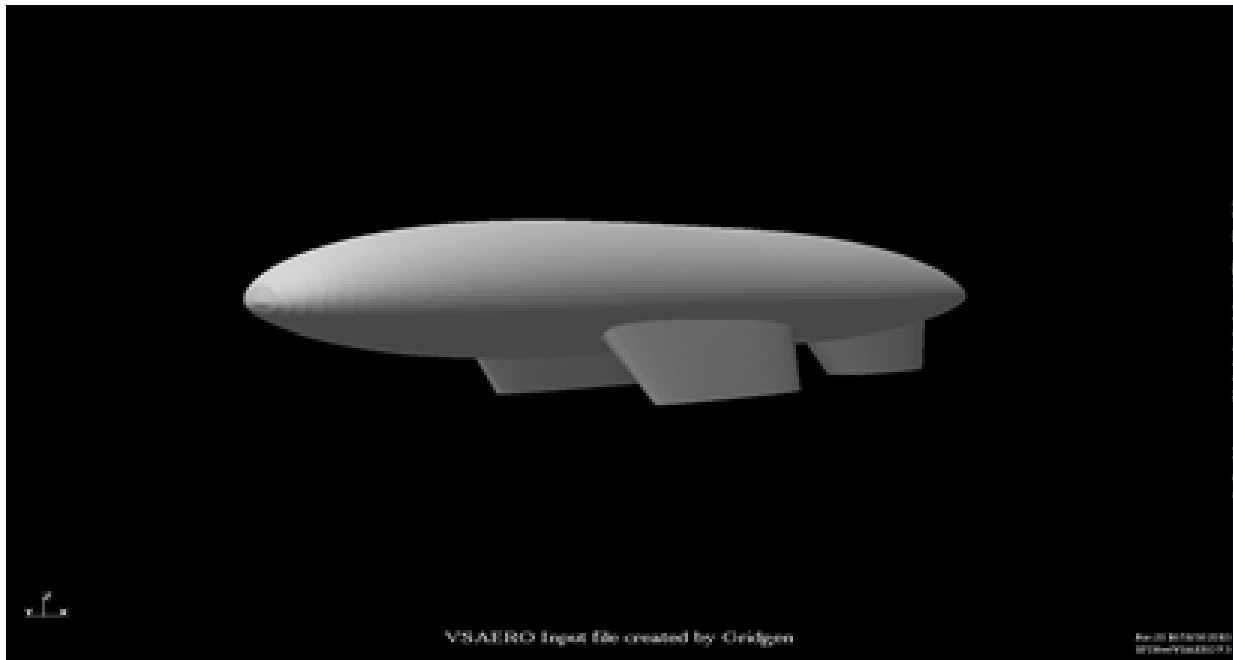


Figure A.4: VSAERO input

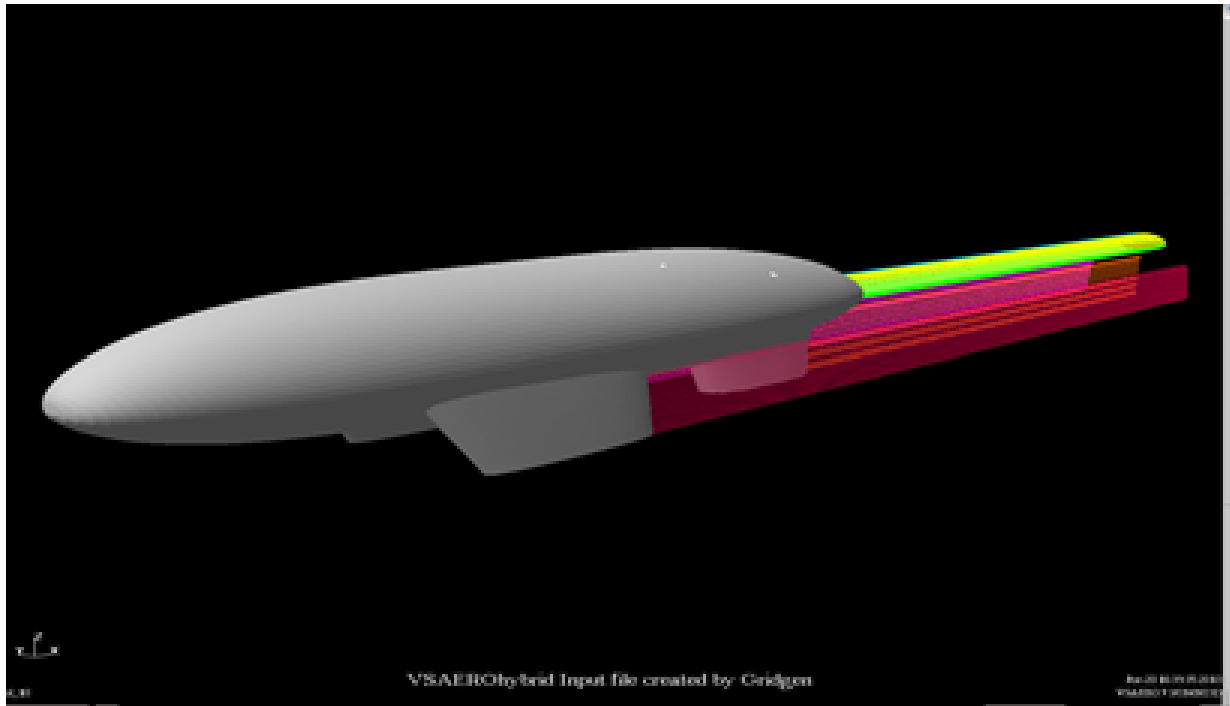


Figure A.5: Adding wakes

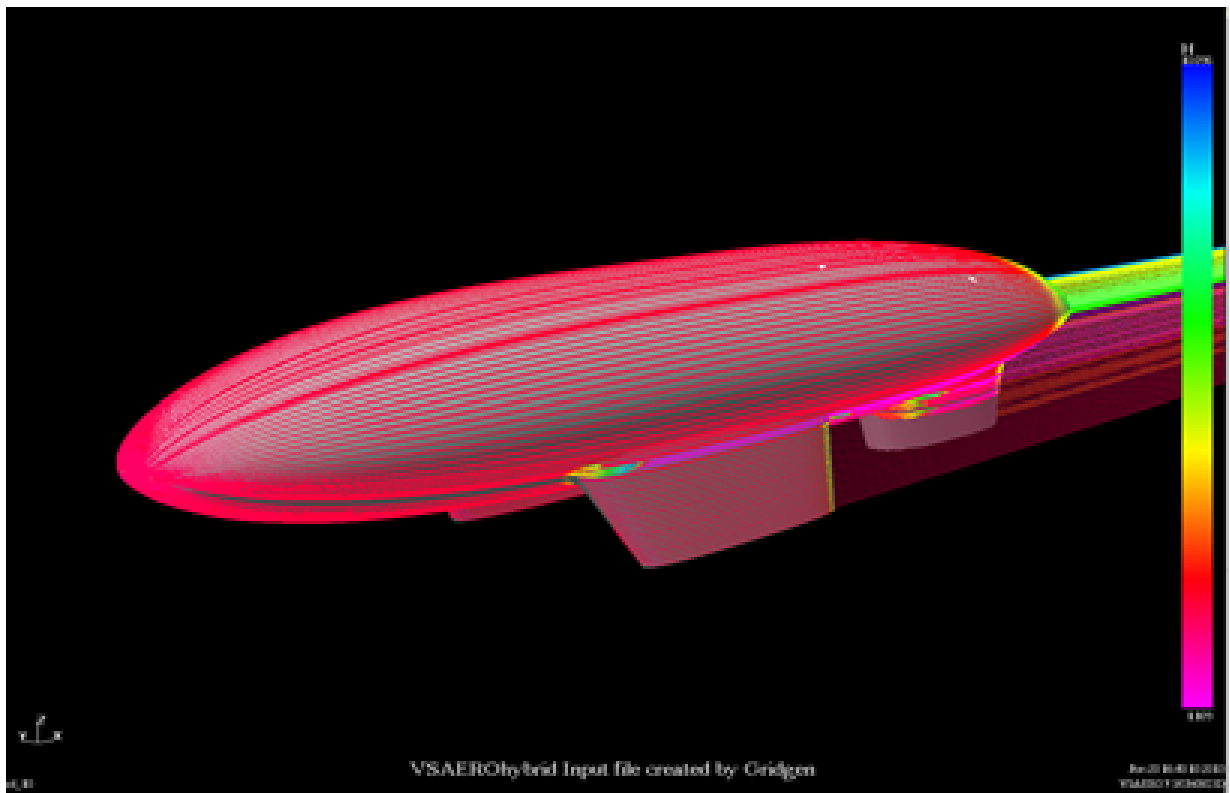


Figure A.6: Output VSAERO



# B Mass Spring System

The Eco-Runner can be modeled as a mass spring system, as shown in Figure B.1. It is interesting to get to know the exact forces that will be introduced in the suspension and transferred to the body. The load case is a bump of  $0.015\text{ m}$  that hits first the front wheels and afterwards the rear wheel. Due to this bump, the center of gravity will undergo a displacement and a rotation.

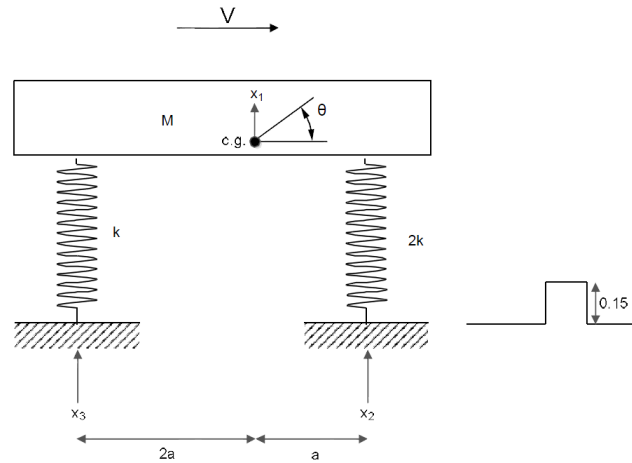


Figure B.1: Schematic drawing of the mass spring system

In Figure B.1 it is observed that the two front wheels are modeled as a spring with spring stiffness coefficient of  $2k$  and the rear wheel as a spring with only  $k$  as spring stiffness coefficient. The  $k$  from an Eco-Runner tire is found from an experiment where the tire is pushed on a scale and the deformation is measured. This spring coefficient is found to be  $65400\text{ N/m}$ . The location of the center of gravity is approximated on  $1/3$  of the total wheel base.

From this model, the following equilibrium equations were found:

$$M\ddot{x}_1 = -3kx_1 + 2kx_2 + kx_3 \quad (\text{B.1})$$

$$J\ddot{\theta} = -6k\theta a^2 + 2kx_2 a - 2kx_3 a \quad (\text{B.2})$$

Afterwards, Equation B.1 and B.2 were combined in a state space system. In this state space system, two step inputs were used. These step inputs illustrate the bump that hit first the front wheels and after  $0.17\text{ s}$  the rear wheel. This time interval is based on the wheel base and a driving velocity of  $6.95\text{ m/s}$ . Using the `lsim` function in MATLAB, the translation and rotation of the center of gravity is obtained. Combining both, the displacement of the wheels is found. Knowing the spring constant, the forces introduced are obtained using equation B.3.

$$F = k \cdot \Delta x \quad (\text{B.3})$$

These forces are plotted over time for both the front and rear wheels and can be seen in figures B.2 and B.3. The variation in amplitude is due to the fact that the maximum translation and maximum rotation does not occur at the same time.

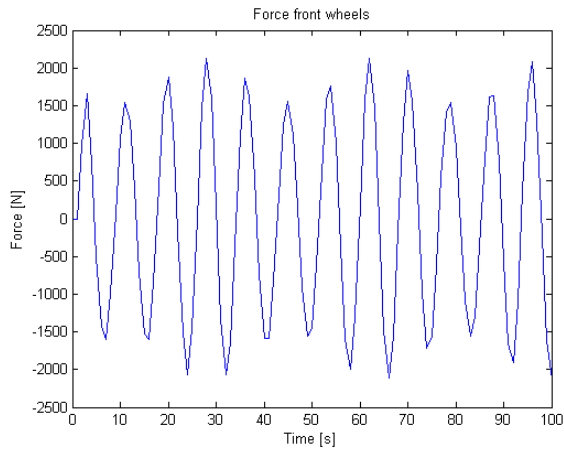


Figure B.2: Forces introduced to the front wheels due to a bump

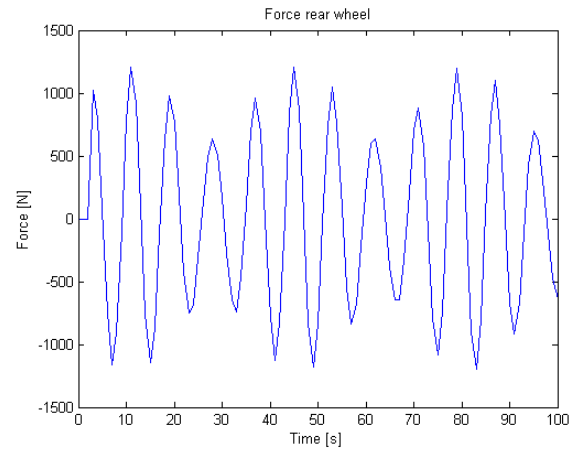


Figure B.3: Forces introduced to the rear wheel due to a bump

It is observed that the maximum force on the rear wheel is  $1209\text{ N}$  and on the front wheel  $2132\text{ N}$ . Since the front wheels are modeled as a spring of  $2k$ , the force found is actually distributed over both wheels. As it is possible that in cornering all forces will come on one wheel with a stiffness  $k$ , both wheels will be designed on this maximum force.

# C Bearings

Table C.1: Bearing specifications [8]

	Front wheel	Rear wheel
Bearing type	Ceramic ball (Si3N4)	Ceramic ball (Si3N4)
Sealing	Shield on one side	Shield on one side
Designation	E2-6000-2Z	E2-6002-2Z
Clearance	C3	C3
Shaft dimension $d$	10 mm	15 mm
Outer diameter $D$	26 mm	32 mm
Bearing width $B$	8 mm	9 mm
Mass	19 g	30 g

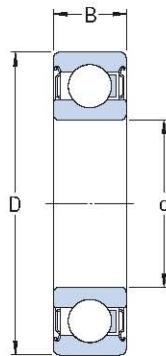


Figure C.1: A cross-section of the bearing



# D Motordata

In this appendix the motor data can be found. These motor data is obtained by the current Eco-Runner Team. The motor is an electrical brushless motor specifically designed by the company Mitsuba for the Eco-Runner. The motor data were found by testing the motor. To get smoothen the data obtained by the test, a MATLAB script was supplied by the current Eco-Runner team. The results of this script can be found in Figure D.1. On the horizontal axis is the velocity at which the vehicle is moving and on the vertical axis the propulsion force delivered to the vehicle by the motor. The colors in the graph represent the efficiency of the motor. Everything below zero means that it is not a valuable data point. No testing was done on these points, or the results were not within the 'two times standard deviation' boundary.

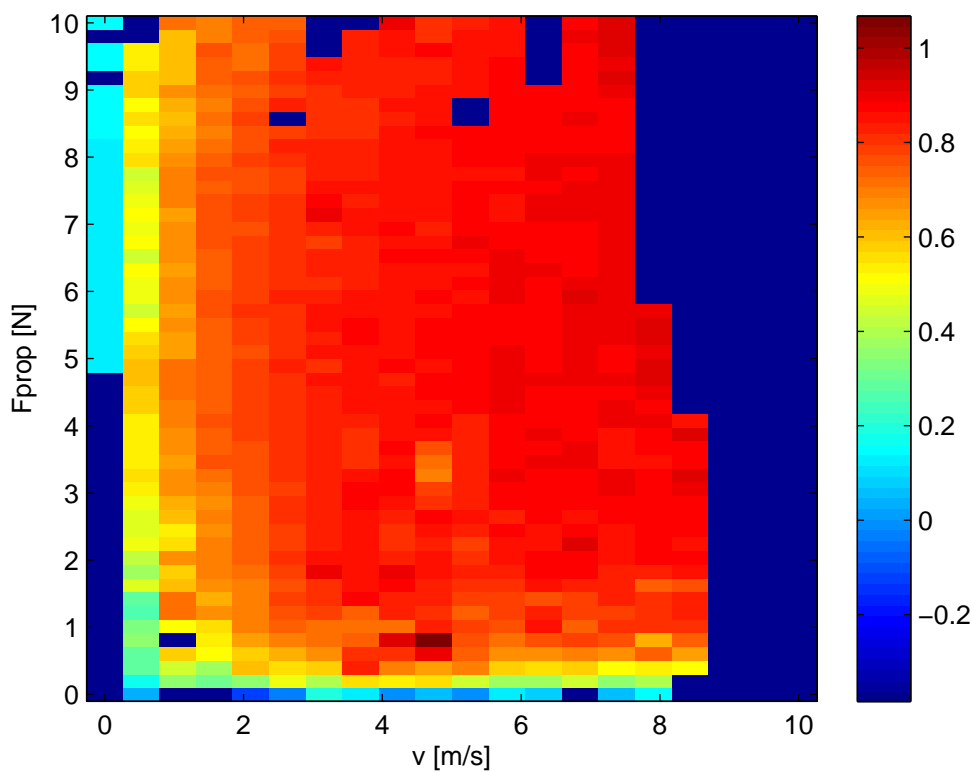


Figure D.1: Efficiency measured by testing the motor



# E Track Rotterdam Specifications

In this appendix, the track in Rotterdam where the race is held this year and next year can be seen. All specifications and dimensions are indicated which are important for determining a driving strategy. A simplified model of the track, used for the simulation, can be found in Table E.1. For the simplified model, the banking angle and the inclination is assumed to be zero.

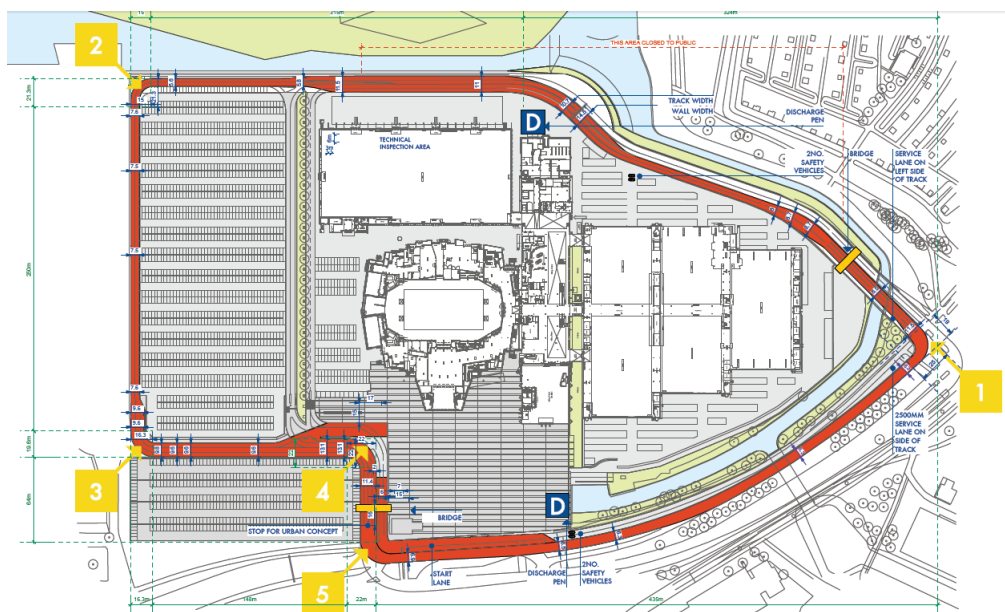


Figure E.1: Map of the race track in Rotterdam for the Shell Eco-marathon

Table E.1: Simplified model of the track

$s_{start}$ [m]	$s_{end}$ [m]	Radius [m]
0	72	infinite
72	279	404
279	408	infinite
408	457	24
457	547	infinite
547	614	131
614	688	infinite
688	726	96
726	768	infinite
768	814	71
814	1069	infinite
1069	1091	21
1091	1348	infinite
1348	1368	19
1368	1500	infinite
1500	1532	21
1532	1595	infinite
1595	1617	21



# F Logbook

This appendix presents the logbook for the final report in table F.1. The logbook shows who wrote and checked which part of the report. Before reading the logbook it must be noted that the logbook gives a distorted image of the actual work done. The logbook merely shows who wrote what, not considering who helped designing a certain system. Moreover, time consuming work, like creating CAD drawings, MATLAB scripts or even concept sketches are not shown in the logbook. Furthermore, every group member has read and checked the report personally, which is not shown in the logbook either. The editors mentioned in table F.1 only indicate the primary editor, who is sometimes more like a co-writer.

Table F.1: Authors and editors per written section

	<b>Section</b>	<b>Written by</b>	<b>Checked by</b>
<b>Front Matter</b>	Preface	Jurriaan	Oane
	Nomenclature	Jurriaan	Oane
	Summary	Elena	Jori
	Introduction	Jurriaan	Alexander
<b>Pre-design considerations</b>	Market Analysis	Elena, Jan-Frederik	Marco
	Sustainable Development Strategy	Elena, Jan-Frederik	Jurriaan
	Functional Breakdown	Nienke & Jurriaan	Alexander
	Functional Flow	Bo	Ruben
<b>Body Aerodynamics</b>	All	Alexander, Bo	Ruben
<b>Body Structure</b>	All	Jan-Frederik	Jori
	Production Plan	Jan-Frederik, Marco	Oane
<b>Suspension</b>	All	Marco, Jori	Jan-Frederik
<b>Driving Strategy</b>	All	Jurriaan, Oane	Bo, Nienke
<b>Electronic System</b>	All	Oane, Ruben	Jan-Frederik
<b>Wheels</b>	All	Elena, Nienke	Marco
<b>The Design</b>	Body Configuration Parameters	Ruben	Jori
	Rollover Stability	Ruben	Marco
	Braking Stability	Ruben	Elena
	RAMS Characteristics	Jurriaan	Nienke
	Cost and Mass Breakdown	Jan-Frederik	Alexander
	Design Overview	Nienke	Jurriaan
	Risk map	Jori	Jan-Frederik
<b>After Project</b>	Project Development	Nienke	Elena
	Manufacturing, Assembly and Integration Plan	Marco, Jan-Frederik	Alexander
	Project Gantt Chart	Bo	Jurriaan
<b>Conclusion and Recommendation</b>		Jurriaan, Oane	Bo